Development of Mid-Infrared Light Emitting Diodes to Replace Incandescent Airfield Lighting

Jonathan Paul Hayton
MPhys (Hons.)

This thesis is submitted in fulfilment of the requirements for the degree of Doctor of Philosophy

Department of Physics
Lancaster University
United Kingdom
October 2016

Centre for Global Eco-Innovation

This project was supported by the Centre for Global Eco-Innovation and is part financed by the European Regional Development Fund.

www.cgeinnovation.org

Development of Mid-Infrared Light Emitting Diodes to Replace Incandescent Airfield Lighting

Jonathan Paul Hayton
MPhys (Hons.)

October 2016

Abstract

This work studied the replacement of incandescent airfield lighting systems with light emitting diodes. The focus was on the replacement of the infrared component of the incandescent spectra. A series of LEDs with a variety of nanostructures in different material systems were produced and tested to determine their suitability in replacing incandescent airfield lighting systems.

Utilising quantum dashes in the active region, a surface emitting LED achieved an output power of 1.2 mW at 1.97 μm. This device had a wall-plug efficiency of 0.7%, an efficiency greater than that obtained in comparable commercially available surface emitting devices. The output power of this device was limited by the confinement of electrons within the quantum dashes at room temperature.

Another device characterised in this study was an LED with sub-monolayer InSb/GaSb quantum dots in the active region. The sub-monolayer InSb quantum dots were grown at Lancaster on GaSb substrates using molecular beam epitaxy

and fabricated into surface emitting LEDs. These were investigated using x-ray diffraction, transmission electron microscopy and electroluminescence. This is the first reported electroluminescence from such devices. Emission was measured at temperatures up to 250 K. Room temperature emission was from the quantum wells in which the quantum dots where grown, output power was 80 μW at a wavelength of 1.66 μm.

Further devices with InSb sub-monolayer insertions were fabricated into edge emitting diodes. These samples were grown on GaAs using interfacial misfit arrays, defect densities were reduced through the use of defect filtering layers. The threading dislocation density decreased by a factor of 6 from $2.5\times10^9/\mathrm{cm}^2$ to $4\times10^8/\mathrm{cm}^2$ between the bottom and top of the defect filtering layer. The edge emitting devices achieved lasing up to 200 K with a characteristic temperature of 150 K. These devices were limited by Shockley–Read–Hall recombination and weak confinement of carriers within the InSb regions. The inclusion of AlGaSb barriers improved room temperature operation with output power increasing from 2 μW to 42 μW. In addition, increased confinement also resulted in a decrease in peak wavelength from 2.01 μm to 1.81 μm.

GaInSb quantum well samples were produced on GaAs substrates utilising an interfacial misfit array. This included the first reported instances of ternary interfacial misfit array interfaces with threading dislocation densities of $<2\times10^9/\mathrm{cm}^2$ for an AlGaSb/GaAs interface and $5\times10^{10}/\mathrm{cm}^2$ for an InAlSb/GaAs interface. By utilising an AlGaSb interfacial misfit array it was possible to improve the confinement of carriers within the GaInSb quantum wells, resulting in a twenty fold increase in room temperature photoluminescence intensity.

Declaration of Authorship

I, Jonathan Paul Hayton, declare that this thesis titled, '*Development of Mid-Infrared Light Emitting Diodes to Replace Incandescent Airfield Lighting*' and the work presented in it are my own. I confirm that:

- This work was done wholly or mainly while in candidature for a research degree at Lancaster University.
- Where I have consulted the published work of others, this is always clearly attributed.
- I have acknowledged all main sources of help.
- No part of this has previously been or is being submitted to any other university or other academic institution.
- Where the thesis is based on work done by myself jointly with others, I have made clear exactly what was done by others and what I have contributed myself.

Signed:

Date:

Acknowledgements

Firstly I would like to thank my supervisor, Prof. Anthony Krier, for the support and guidance he has given me during my studies.

I would also like to thank my examiners Dr Andy Marshall and Prof Mohamed Henini.

I am also grateful to those within the department who assisted in the growth and characterisation of my samples, namely, Dr Michael Thompson, Dr Peter Carrington, Hiromi Fujita, Dr Adam Craig and Dr Kylie O'Shea.

Science is a collaborative endeavour and I would also like to thank those people from different institutions who have offered their time, knowledge and facilities to provide me with new insight into the work I have done. This included Dr Ken Kennedy and Saurabh Kumar at Sheffield University, Prof. Stephen Sweeney and Dr Igor Marko at the University of Surrey, and Dr Siddharth Joshi of the III-V Lab, France.

In the past four years I have been very lucky to occupy two great offices. My thanks to Kylie O'Shea, Claire Tinker-Mill, Alex Robson, Sam Harrison, Qi Lu, Aiyeshah Alhodaib, Chris Woodhead, Jonny Roberts, Alex Jones and Yasir Noori for making this possible.

I have also benefited during my time in the department from excellent support from the technical support staff. I would like to thank Stephen Holden, Shonah Ion, Stephen Holt, Ashley Wilson, John Statter, Graham Chapman, Phelton Stephenson, Robin Lewsey and Dr Kunal Lulla Ramrakhiyan.

I would also like to take this opportunity to thank Dr Russell Harvey for being a fantastic boss during my work as a technician. I truly enjoyed supporting first year labs and the challenges this entailed. I must also thank you for being so accommodating of the needs of my research.

My work was supported by the Centre for Global Eco-Innovation and I would like to thank all involved for their support during the project.

The support of my family has never wavered and for this I give them special thanks. It has been a comfort to know you've always had an open door. It is from you that I gained my questioning mind which has led me to where I am today.

In writing these acknowledgements you come to realise just how many people make a PhD possible, to these people I am indebted, but none more so, than to Steph. This journey has been one we have taken together and whilst it has certainly taken the path less travelled the scenery on the way has been worth it. I only hope that I can be there for you, as you have been for me these last few month giving me the occasional little push up the hill.

Publications

1. JP Hayton, ARJ Marshall, MD Thompson, and A Krier. Characterisation of $Ga_{1-x}In_xSb$ quantum wells ($x \sim 0.3$) grown on GaAs using AlGaSb interface misfit buffer. *AIMS Materials Science* 2(2): 86–96, 2015

2. Q Lu, Q Zhuang, JP Hayton, M Yin and A Krier. Gain and tuning characteristics of mid-infrared InSb quantum dot diode lasers. *Appl. Phys. Lett.* 105: 031115, 2014

3. JP Hayton, PJ Carrington, H Fujita, A Krier. Electroluminescent properties of sub-monolayer InSb quantum dots grown on GaSb by MBE. – paper in preparation.

Presentations

1. JP Hayton, ARJ Marshall, MJ Thompson, and A Krier. A Comparative Study of GaInSb Quantum Wells Grown on GaSb and Interfacial Misfit GaAs. **UK Semiconductors 2014**, Sheffield, UK. (Poster)

2. JP Hayton, ARJ Marshall, MJ Thompson, and A Krier. Thermal quenching of $Ga_{1-x}In_xSb$ quantum wells ($x \sim 0.3$) grown on GaAs using AlGaSb interface misfit buffer. **UK Semiconductors 2015**, Sheffield, UK. (Poster)

3. JP Hayton, ARJ Marshall, MJ Thompson, and A Krier. Characterisation of $Ga_{1-x}In_xSb$ quantum wells LEDs ($x \sim 0.3$) grown on GaAs using AlGaSb interface misfit buffer. **WOCSDICE 2015**, Smolenice, Slovakia. (Talk)

Contents

List of Figures

List of Tables

Chapter 1

Introduction

1.1 Motivation

Every day thousands of planes land in situations of limited visibility, be this either low light or inclement weather. This is achieved through the use of Enhanced Flight Visions Systems (EFVS)[1] which use an InSb based forward looking infrared (FLIR) camera to project an image of the environment as seen in the infrared (IR) into the cockpit. The source of IR light is the blackbody radiation inherent in the tungsten filament bulbs currently utilised in runway lighting. In using this light, EFVSs bypass the limitations of visible light in cloud/fog caused by scattering. This is achieved through the use of atmospheric transmission windows available in the mid-IR (2-4 μm) as shown in Figure 1.1. Unfortunately, these bulbs are very inefficient and legislation such as the *Energy Independence and Security Act of 2007*[2] is being instigated to phase them out of service in line with other energy efficiency drives.

The environmental impact of current runways systems can be calculated by looking at the power requirements of a single runway. A typical runway requires 100 MWh of electricity per annum, dependant upon length. Given the approximately 13,000 paved and lit runways on the planet[3] this results in an energy usage of 13 TWh. This comes with an associated CO_2 release of 7×10^5 tonnes, showing a clear need to replace these light systems with more environmentally friendly systems.

Replacements for the visible part of the spectrum have been sourced using 19 high power white LEDs delivering over 400,000 cd of light with energy usage 70% less than a comparable traditional halogen bulb[4]. Mean time to failure has also vastly improved from 100 hours for halogen lights to 10,000 for current generation white LEDs. An example of this light is given in Figure 1.2a. The use of LEDs as the light source has removed the infrared component seen in traditional blackbody lighting solutions. This means that current generation EFVS is no longer interoperable with the runway lighting, removing a key safety component in modern commercial aviation. Oxley Developments

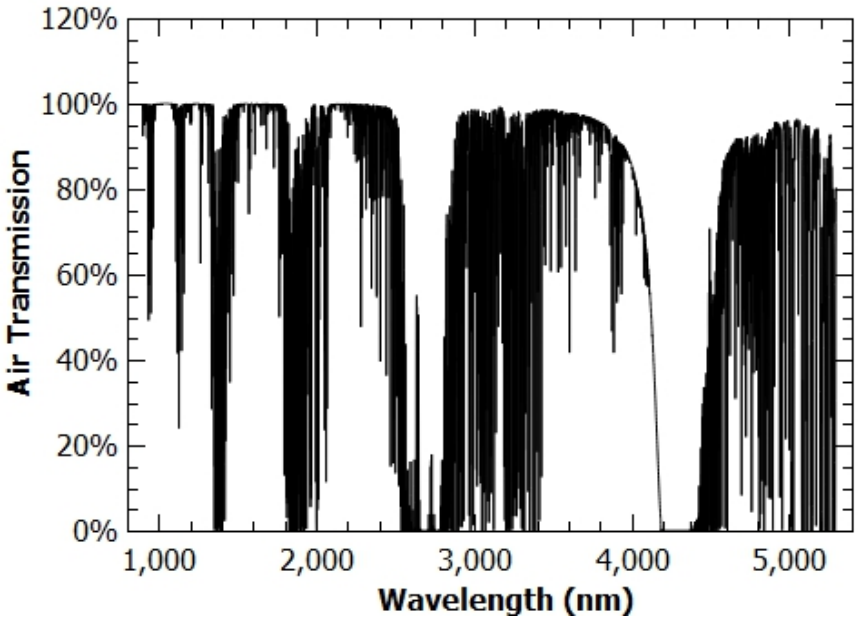

Figure 1.1: Optical transmission of air as a function of wavelength.

presented me with the task of making their high power runway lighting system compatible with legacy EFVSs[4]. To achieve this it was quickly decided to utilise the 2.2 μm atmospheric transmission window through the creation of light emitting diodes (LEDs), even though these have lower output powers than laser diodes, they were chosen due to the perceived dangers associated with lasers and plane safety.

Initial investigations indicated that to replace the emission from an incandescent source in the 2.2 μm atmospheric window would require an output of 2.7 W, a value far greater than that currently available as will be shown in Section 3.1. The focus of this project was the development of the means to achieve this level of output within the footprint of the current Approach Lighting System (ALS). If we assume a similar number of infrared LEDs in the final product as there are white LEDs, each device requires an output in the order of 100 mW. The focus was given to the replacement of the lighting aspect of the EFVS over the sensor component, not only due to the legislative impetus but also logistical reasons. It is easier to change the lighting systems on a runway

(a) (b)

Figure 1.2: (a) An example of an LED replacement for an Approach Lighting System lamp[4]. (b) An example of the view afforded by the use of Enhanced Flight Vision Systems[5].

when compared to the 30,000 aircraft of various types and specifications each requiring certification and testing.

The investigation into a solution is split into two sections. Chapter 5 investigates materials that can allow large area devices and possible future integration between the white LED and the infrared source. This was achieved by investigating metamorphic material growth through techniques such as interfacial misfit arrays. Chapter 6 will investigate LEDs with active regions involving different degrees of quantum confinement, from bulk materials to quantum dots. By necessity, to achieve 2.2 μm light emission these devices will involve different III-V material systems, but will aim to determine which, if any quantum system has properties beneficial to applications of high power 2 μm light sources. This will include devices grown at Lancaster University using MBE, including the first reported sub-monolayer InSb/GaSb Quantum Dot LEDs. Other samples will come from commercial sources and Prophet network partner institutions, as in the case of the quantum dash LEDs.

Chapter 2

Background Theory

2.1 Introduction

This chapter will cover the theoretical foundations that underline the work in later chapters. This will include the electronic structure of semiconductor materials, the operation of light emitting diodes and how efficiency can be measured.

2.2 Band Structure of Semiconductors

When atoms or molecules form a solid, their discrete energy levels mix to form energy bands. When this occurs, all lower energy bands are filled leaving only the outer most bands with electrons capable of being excited to higher levels, due to this all other bands are typically not considered.

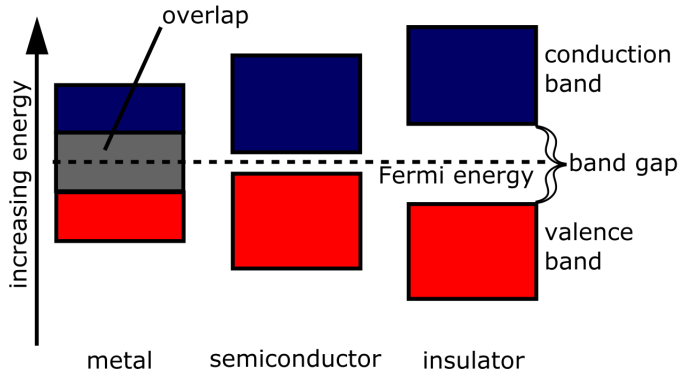

Figure 2.1: Comparison of band structures of metals, semiconductors and insulators[6].

The two bands which are considered are known as the valence band and conduction band. The valence band is the outer most fully occupied band, and the conduction band the next highest. In the case of metals these two bands overlap, but in insulators and semiconductors there is an energy gap between the top of the valence band and the bottom of the conduction band. At 0K all electrons occupy the valence band, as temperature increases, the thermal energy is sufficient to promote some electrons across the narrow band gap of the semiconductor as can be seen in Figure 2.1.

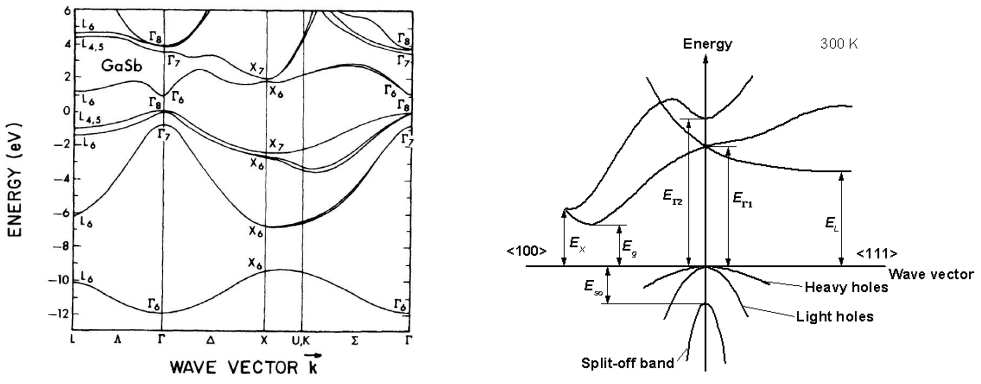

(a) (b)

Figure 2.2: (a) Band structure of gallium antimonide[7]. (b) Band structure of silicon[8].

In momentum space the band structure can be shown with a E-k diagram as seen in Figure 2.2a. In the case of GaSb there is a direct band gap meaning there is no momentum change between the conduction band minimum and valence band maximum, if this had not been the case then we would have an indirect band gap for example silicon(Figure 2.2b). Around k=0 the bands are roughly parabolic as can been seen in Figure 2.2a and can be described by the following relations [9];

$$E_c = E_g + \frac{\hbar^2 k^2}{2m_e} \tag{2.1}$$

$$E_{hh,lh} = -\frac{\hbar^2 k^2}{2m_{hh,lh}} \tag{2.2}$$

$$E_{SO} = -\Delta - \frac{\hbar^2 k^2}{2m_{SO}} \tag{2.3}$$

where E_g is the band gap, $m_e, m_{hh,lh}, m_{SO}$ are the effective masses of the electron, heavy hole, light hole and split–off hole respectively and Δ is the spin-orbit splitting. The spin–orbit splitting band (SO band) is energy shifted from the other valence bands due to Zeeman splitting caused by the interaction of the spin of the electrons with the magnetic field produced by their orbit.

2.3 Temperature Dependence of Band Structure

As temperature increases the lattice spacing of semiconductors increases. This increase in separation reduces the energy binding of the electrons, reducing the energy needed to excite electrons to the conduction band, thus reducing the band gap. This reduction can be described empirically using the Varshni equation[10];

$$E_g\left(T\right) = E_g\left(0\right) - \frac{\alpha T^2}{\beta + T} \tag{2.4}$$

where $E_g\left(0\right)$ is the band gap at 0 Kelvin and α and β are fitting parameters. This dependence is also valid for non-bulk transitions in quantum wells. Typically the Varshni fitting overestimates the transition energy at low temperatures, this derives from the effect of localised band minima. At low temperatures carriers have insufficient energy (kT) to escape localised band minima - for example due to inhomogeneous alloy mixing. This observation was made by Botha and Leitch when they noted that the deviation from Varshni's law was proportional to the full width half maximum of the photoluminescence of samples, another indicator of quantum well interface roughness[11]. Another approach to the temperature dependence of the band gap is based on the proportionality of the shift in band gap energy and average phonon energy first reported by Vina *et al.* the relation henceforth known as Vina's relation[12];

$$E_g\left(T\right) = a - b\left(1 + \frac{2}{\exp\left(\frac{\Theta}{T}\right) - 1}\right) \tag{2.5}$$

where $a - b = E_g\left(0\right)$ the band gap energy at 0 K, T is temperature and $\Theta = \frac{h\nu_{ph}}{k}$ where ν_{ph} is the average phonon frequency and h & k are Planck's and Boltzmann's constants respectively. An explanation of the physical origins of this relation are not communicated.

2.4 Band Alignment at Heterojunctions

Where two different materials interface a difference in electron affinity and or bandgap will cause a discontinuity in both or either of the valence and conduction bands. Electron affinity (χ) is the separation between the conduction band and vacuum level. This causes offsets ΔE_C and ΔE_V which can be determined using[13];

$$\Delta E_C = \chi_2 - \chi_1 \tag{2.6}$$

$$\Delta E_V = (\chi_1 + E_{g1}) - (\chi_2 + E_{g2}) \tag{2.7}$$

where E_g is the band gap of the material. These values are positive when there is an increase in energy for the corresponding particle (electron in conduction, hole in valence) between materials.

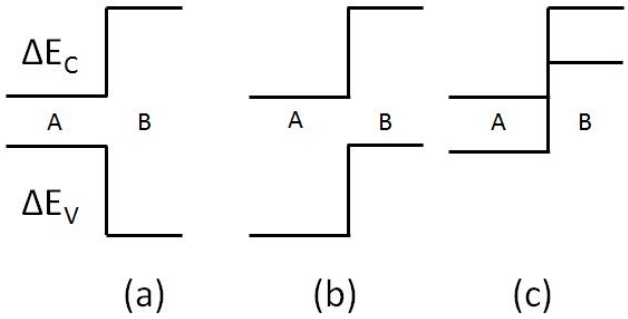

Figure 2.3: Heterojunction band alignments, (a) Type I band alignment, (b) Type II band alignment and (c) Type II 'broken gap' alignment.

Type–I Alignment

When both offsets are of the same sign this is known as type-I alignment. In the case where a narrow band material is sandwiched between two wider gap layers both the holes and electrons are confined. The InGaSb/(Al)GaSb interface discussed in this work

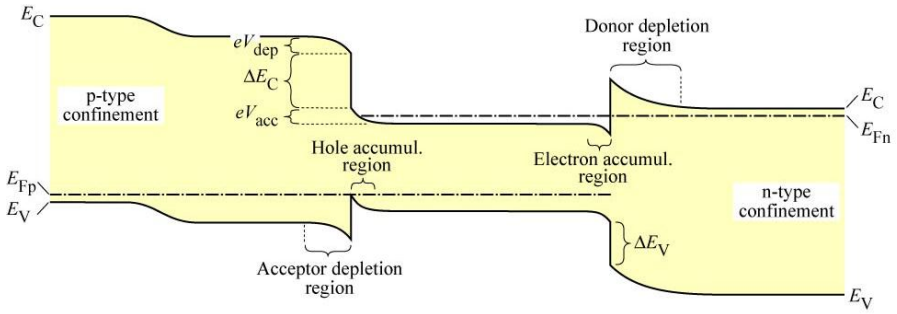

Figure 2.4: Band diagram of a forward biased double heterojunction [14](adapted from [15]).

is an example of type-I alignment. Other examples are InAs/GaAs and GaSb/AlSb.

Type–II Alignment

When ΔE_C and ΔE_V are of different signs then the two carriers are confined on different sides of the interface. Recombination occurs as the wavefunctions overlap beyond the interface. The carriers are no longer symmetric at the interface, one needs to gain energy and the other to lose it at the interface. An extreme example of this is the 'broken gap' alignment, where the valence band of one layer has a greater energy than the conduction band of the other layer.

Band Bending

At the interface of two regions an electric field is formed by the diffusion of carriers to the lower energy side of the interface. This field bends the bands as shown in Figure 2.4. Such features can cause strong localised confinement of carriers at low temperatures similar to a quantum well. Such interfaces can result in potentials that can block carrier transport, this can be reduced by replacing abrupt interfaces with graded ones.

2.5 Quantum Structures

When a material is sandwiched between 2 layers of another material the carriers become confined within that region. If the region is comparable in size to the de Broglie wavelength of an electron the energies these electrons can have become quantized.

A quantum well has one dimension in which the electron is confined, in the z axis, the direction of growth. The confined energy levels can be found by solving the Schrödinger equation

$$E\Psi = -\frac{\hbar^2}{2m}\frac{d^2\Psi}{dz^2} + V_0(z)\,\Psi \tag{2.8}$$

where E is the energy, m is the effective mass, Ψ is the wave function of the energy state in the z-direction and $V_0(z)$ is the potential barrier. Due to the finite nature of the potential in a quantum well it is necessary to consider the wavefunction both within the well and the barriers. If we consider the well to be of width w and centred on z=0 then

$$\frac{\hbar^2}{2m}\frac{d^2\Psi}{dz^2} + k_1^2\Psi(z) \text{ for } |z| < \frac{w}{2} \text{ with } k_1 = \sqrt{\frac{2mE}{\hbar^2}} \tag{2.9}$$

$$\frac{\hbar^2}{2m}\frac{d^2\Psi}{dz^2} + k_2^2\Psi(z) \text{ for } |z| < \frac{w}{2} \text{ with } k_2 = \sqrt{\frac{2m(V_0 - E)}{\hbar^2}} \tag{2.10}$$

where k_1 and k_2 are the wave functions of the well and barrier respectively. For the boundary conditions to be satisfied both the wave function and its derivative must be continuous at the interface. It can thus be shown

$$\left(k_1\frac{w}{2}\right)^2 + \frac{m_w}{m_b}\left(k_2\frac{w}{2}\right)^2 = \frac{2m_wV_0}{\hbar^2}\left(\frac{w}{2}\right)^2 \tag{2.11}$$

and

$$k_2\sqrt{\frac{m_b}{m_w}}\frac{w}{2} = \frac{m_b k_1}{m_w}\frac{w}{2}\tan\left(k_1\frac{w}{2}\right) \text{ for even solutions} \tag{2.12}$$

$$k_2\sqrt{\frac{m_b}{m_w}}\frac{w}{2} = -\frac{m_b k_1}{m_w}\frac{w}{2}\cot\left(k_1\frac{w}{2}\right) \text{ for odd solutions} \tag{2.13}$$

where m_b and m_w are the particle masses in the barrier and well respectively. The energy can be determined using equation 2.9 where k_1 is found from the intercept of 2.11 and either 2.12 or 2.13.

In the case of quantum wires and quantum dots additional degrees of confinement require consideration of the potentials in additional dimensions. This requires a solution to the Schrödinger equation in more than one dimension.

2.6 Density of States

Because electrons are bound by Pauli's exclusion theorem they cannot all occupy the lowest energy at the band edge and are distributed in a number of available states. The energies of these states can be determined by calculating the Density of States (DOS) The DOS describes the number of states per unit energy per unit volume such that the carrier density , N, within an energy interval, dE, is given by [16];

$$N(E) = g(E)\,dE \tag{2.14}$$

where $g(E)$ is the DOS with units of per unit volume per unit energy .

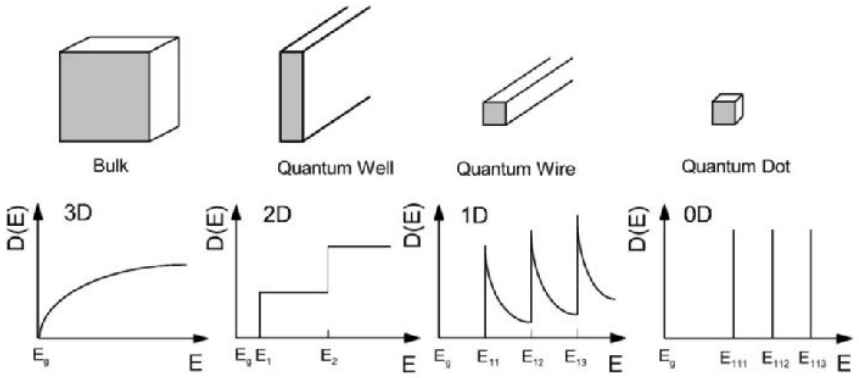

Figure 2.5: Density of States for bulk, quantum wells, quantum wires and quantum dots[17].

The derivations of the DOS for bulk, wells, wires and dots can be found in many textbooks [13]. The results are compiled below:

Dimension	DOS
3	$\frac{1}{2\pi^2}\left(\frac{2m^*}{\hbar^2}\right)^{\frac{3}{2}}(E-E_g)^{\frac{1}{3}}$
2	$\frac{m*}{\pi\hbar^2}\sum_i H(E-E_i)$
1	$\sqrt{\frac{2\pi m^*}{h^2}}\frac{1}{\sqrt{E-E_{min}}}$
0	$2\delta(E-E_{min})$

The probability of an electron being in a given energy level is given by the Fermi-Dirac distribution. The Pauli exclusion principal, which states that fermions – such as electrons – must each occupy an individual state and as such will fill up the available states in the energy band up to the maximum energy at zero Kelvin. In an intrinsic semiconductor this level, the Fermi level is in the middle of the band gap. As the temperature increases the electrons become thermally excited increasing in energy until it is possible to be promoted to the conduction band leaving holes in the valence band.

Thus by multiplying the DOS and Fermi-Dirac distribution it is possible to show the distribution of electrons in a semiconductor and thus the theoretical emission spectra (Figure 2.6). For example, in the bulk case electrons should statistically be most likely

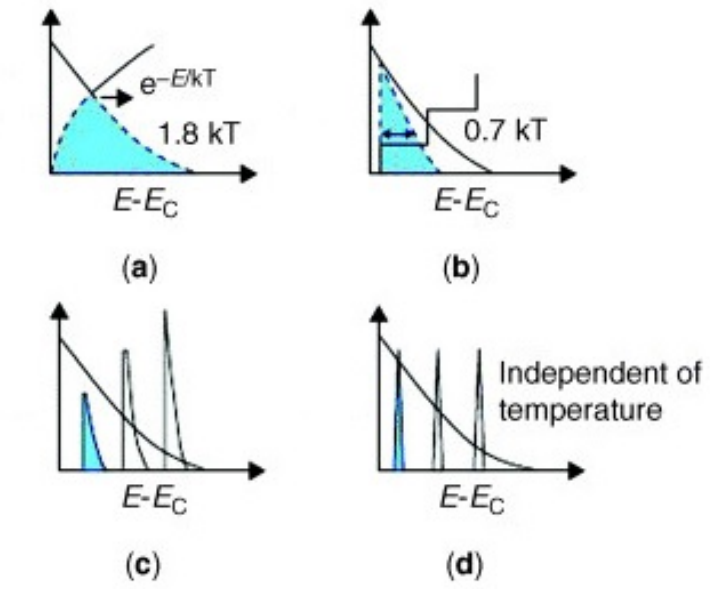

Figure 2.6: Theoretical emission spectra in; (a) bulk semiconductor and (b) quantum wells, (c) wires and (d) dots.[18]. y-axis indicates the number of carriers at a given energy in arbitrary units. For (a) and (b) the FWHM of the spectra is included in units of kT.

found at the band edge, but due to the density of states their are few available states at this energy with more found at higher energies. Because of this the most likely energy of electrons and thus the peak of the emission spectra is approximately 0.6kT above the band edge for a bulk semiconductor.

G. Rainò *et al.* proposed a fitting function for quantum wells based upon this theoretical distribution [19];

$$I_{EL}(E) = A\left[\text{erfc}\left(\frac{E_g - E}{\sigma\sqrt{2}}\right)\exp\left(-\frac{E - E_g}{k_B T}\right)\right] \tag{2.15}$$

where $I_{EL}(E)$ is the intensity of light at a given photon energy (E), erfc is the compli-

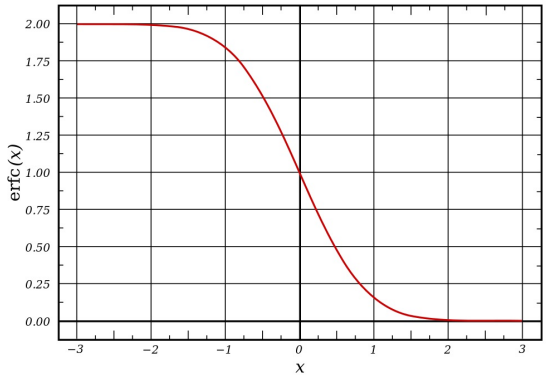

Figure 2.7: Plot of complimentary error function (erfc(x)).

mentary error function (Figure 2.7), this has values of;

$$\text{erfc}(-\infty) = 2$$

$$\text{erfc}(0) = 1$$

$$\text{erfc}(\infty) = 0$$

This function represents the step function seen in the 2D DOS, only giving values above the band edge($E_g < E$). σ is a fitting parameter to take into account inhomogeneous broadening, the smaller this value the closer to a flat band edge the DOS has. E_g is the energy minima of the DOS. The exponential function considers the thermal distribution of carriers above E_g where T is the lattice temperature and k_B is Boltzmann's constant.

Quantum structures are thus beneficial with LEDs as the number of available states in the ground state increases as we reduce the dimensionality of the system. It also causes the spacial confinement of the carriers to a specific locality. Both lead to a superior performance for the LED. The use of quantum structures also increases the degree to which the device can be engineered. Emission wavelength can be tuned by varying not only the composition of the device, but also the size of the quantum region and thus the confinement. The options for material also increase, as due to their small

size they are less constrained by strain limitations opening more material systems to exploitation.

2.7 Recombination

When a forward voltage is applied to a diode, excess carriers are introduced, electrons in the n-type side and holes in the p-type. These carriers diffuse to the depletion region at the interface of the p and n regions where they recombine. This can occur via several processes, in the case of LEDs the desired recombination is radiative, where the relaxing electron emits a photon equivalent to the amount of energy it has lost. This need not be a band to band transition, it can also occur to and from donor and acceptor states close to the band edge as seen in Figure 2.8.

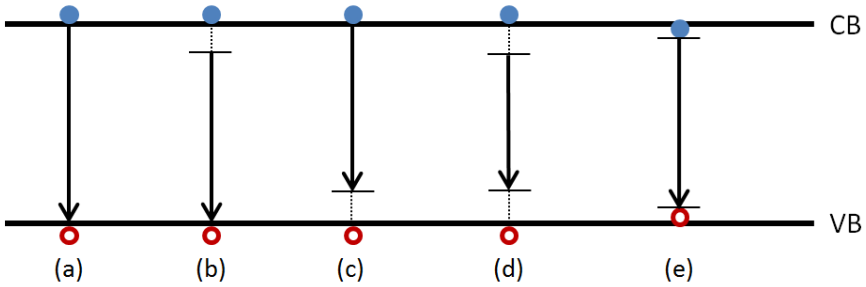

Figure 2.8: Various possible radiative transitions, solid lines indicate radiative processes and dashed lines non-radiative where: (a) is band-to-band transition, (b) donor to valence band, (c) conduction band to acceptor, (d) donor to acceptor and (e) excitonic recombination.

As well as radiative recombination there are undesirable recombinations which do not produce light such as Shockley-Read-Hall (SRH) and Auger recombinations. When the carriers are generated electrically at a rate of $I(n)$ then it can be assumed that;

$$I(n) = An + Bn^2 + Cn^3 + I_{leak} \tag{2.16}$$

where n is the excess carrier concentration, A, B and C are the rates of SRH, Radiative and Auger recombination respectively. I_{leak} is the leakage current, carriers that due to defects does not contribute to recombination but bypasses the junction. Auger recombination is a three carrier process in which an interband transition causes the excitation of an additional carrier. This becomes more prevalent as the band gap decreases due to a decrease in activation energy and an increase in Auger coefficient in narrow band materials.

2.7.1 Shockley–Read–Hall(SRH)

SRH occurs in the presence of a state deep in the band gap, caused by a native lattice defect or impurity atom, where carriers relax into this state and are thus "trapped". This relaxation can occur through the emission of multiple phonons or a photon, even when a photon is emitted it is considered non-radiative as the energy is much lower than the band gap and thus outside the desired emission.

The rate of SRH (A) is defined as;

$$A_{SRH} = \frac{1}{\tau_{SRH}} \tag{2.17}$$

where τ_{SRH} is the carrier lifetime. This lifetime is temperature dependent[20];

$$\tau_{SRH} = \tau_0 \left(1 + \cosh \frac{E_{tr} - E_{Fi}}{kT}\right) \tag{2.18}$$

where τ_0 is the lifetime at zero Kelvin, $(E_{tr} - E_{Fi})$ is the difference in energy of traps from the Fermi energy, k is Boltzmann's constant and T is temperature.

2.7.2 Radiative Recombination

Radiative recombination occurs when an electron hole pair recombine across the band gap producing a photon with energy equal to the transition. Typically these transitions

are at or above the band gap energy though it is possible to get some sub-band gap energy emission due to shallow donor/acceptor states or to excitonic binding of the electron hole pair.

The energy of the emitted photon depends upon the process involved but for band to band transitions (Figure 2.8(a)) the average photon energy, $h\nu$ is given by;

$$h\nu = E_g\left(T\right) + \frac{1}{2}kT \tag{2.19}$$

where $E_g(T)$ is the band gap energy as a function of temperature, T is temperature and k is the Boltzmann constant.

In the presence of shallow donor or acceptor states, at low temperatures carriers can be trapped in these sites and recombine via them (Figure 2.8(b) and (c)) this results in transitions defined by;

$$h\nu = E_g\left(T\right) + \frac{1}{2}kT - E_i \tag{2.20}$$

where E_i is the binding energy of the acceptor or donor state. These states are a result of defects or impurities in the material. These effects are only seen at low temperatures because as temperature increases carriers have sufficient energy to escape to either the conduction or valence band suppressing transitions involving donors and acceptors.

If recombination occurs via both an acceptor and a donor state then an additional term is required;

$$h\nu = E_g\left(T\right) - \left(E_D + E_A\right) + \frac{e^2}{4\pi\epsilon_0\epsilon_r r} \tag{2.21}$$

where e is the electron charge, E_A and E_D are the acceptor and donor binding energies respectively, ϵ_0 & ϵ_r permeability of free space and relative permeability of the

semiconductor and r is the spatial separation of the two carriers. The final term in the equation is due to the coulomb interaction between the two carriers (d).

Coulomb interaction is also present in the formation of excitons - bound electron hole pairs which lowers the energy of the transition(e) given by;

$$h\nu = E_g\left(T\right) - E_{Xf} \tag{2.22}$$

where E_{Xf} is the free exciton binding energy. Excitons in semiconductors are of the Wannier-Mott type, due to the screened Coulomb interaction and small effective masses the radius of these excitons is large at 10 nm with a binding energy of the order 10 meV E_{Xf} can be calculated using

$$E_{Xf} = 13.6\frac{\mu}{n\epsilon_0\epsilon_r}\text{eV} \tag{2.23}$$

where μ is the reduced mass

$$\mu = \frac{m_e m_h}{(m_e + m_h)} \tag{2.24}$$

and ϵ_0 and ϵ_r are the permittivity of free space and relative permittivity of the semiconductor[21].

2.7.3 Auger Recombination

Auger recombination is a process by which the energy released by a recombination across the band gap is used to excite another carrier instead of the generation of a photon. There are several different modes of Auger recombination, dependant upon which carriers are excited. The naming convention for Auger recombination takes the form of a four letter acronym; the first two letters indicate the movement of the relaxing carrier and the second two the movement of the excited carrier. C represents electrons, H heavy holes and L light holes. The key ones in III-V semiconductors are CHCC (energy of recombination excites an electron up the conduction band) and CHSH (recombination excites an electron from the SO band to the heavy hole band) which are shown in Figure

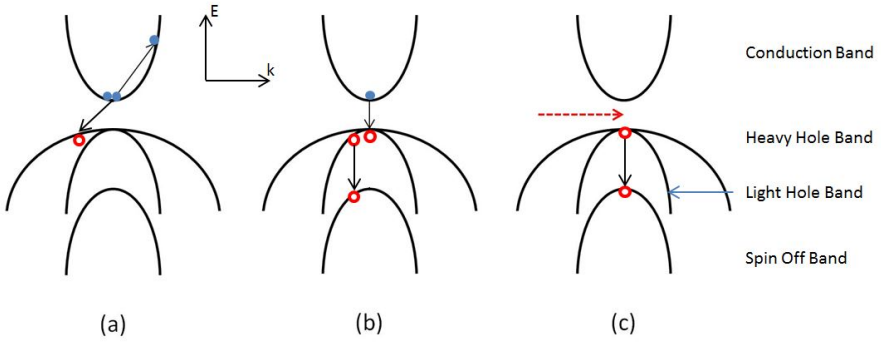

Figure 2.9: Auger recombination methods: (a) CHCC, energy of recombination excites an electron up the conduction band. (b) CHSH, energy of recombination excites an electron from the SO band to the heavy hole band. (c) Intervalence Band Absorption, a process similar to Auger recombination, the initial energy is provided by an absorbed photon.

2.9.

The rate of Auger recombination (C) is determined by,

$$C = \sum_i C_i e^{\left(-\frac{E_{ai}}{kT}\right)} \tag{2.25}$$

where C_i is the rate for each Auger process at zero Kelvin with E_{ai} being the activation energy associated with that process as outlined below.

In CHCC the recombination provides the energy for another electron to be excited higher up the conduction band. The activation energy for this process is[22];

$$E_a^{CHCC} = \left(\frac{m_c}{m_c + m_h}\right) E_g \tag{2.26}$$

where m_c is the electron effective mass, m_h is the heavy hole effective mass and E_g is the transition energy. It can be seen that the activation energy decreases with increasing wavelength (as $E_g \propto \frac{1}{\lambda}$) which corresponds to an increase in CHCC recombination in longer wavelength devices.

In CHSH the recombination excites a carrier from the SO band into the heavy hole band with an activation energy of;

$$E_a^{CHSH} = \left(\frac{m_s}{2m_h + m_c - m_s}\right)(E_g - \Delta_{so}) \tag{2.27}$$

where m_s is the effective mass of SO band holes and Δ_{so} is the energy gap between the heavy hole and SO bands. In practical terms this means that if $\Delta_{so} > E_g$ then the CHSH process is effectively suppressed but when $\Delta_{so} = E_g$ resonance is achieved and the CHSH rate is greatly increased.

2.7.4 Intervalence Band Absorption

Inter valence band absorption is a key loss mechanism in narrow band gap materials. An emitted photon is reabsorbed promoting an electron from the SO band to the heavy hole band. Similar to Auger processes the activation energy of the process can be defined as;

$$E_a^{IVBA} = m_s \frac{(\hbar\omega)}{(m_h - m_s)} \tag{2.28}$$

where ω is the frequency of the absorbed photon.

2.7.5 Surface Recombination

The surface of a semiconductor is a substantial source of non-radiative recombinations. By their very nature these surfaces are an extreme perturbation to the periodicity of the lattice, which modifies the band diagram at the surface allowing additional states in the forbidden gap. Chemically the surface also differs from the main bulk of the semiconductor, where not all valence orbitals can achieve a chemical bond. This results in partially filled electron orbitals, known as 'dangling bonds' which are electrical states that can be located within the forbidden gap and act as recombination centres. Depending on the charge state of these bonds they can also act as donor-like or acceptor-like

states. As recombination occurs in this region it is depleted, and as a result, additional carriers from the surrounding higher carrier density regions flow into the depleted region. This means that the surface recombination is limited by the rate at which the carriers arrive at the surface. This parameter is known as the surface recombination velocity, given units of cm/s. If there is no recombination at the surface, carriers will not move to the surface so the surface recombination velocity is zero. If surface recombination could happen infinitely fast recombination would be limited by the maximum velocity the minority carriers could achieve typically of the order 10^7cm/s in semiconductors.

To reduce surface recombination the surface can be treated in a process known as passivation. This is done by introducing to the surface an additional material which does not form part of the semiconductor but which bonds to the dangling bonds. In GaSb two possible passivation methods are treatment using sulphur containing chemicals or deposition of hydrogenated amorphous silicon[23, 24]. The deposition of hydrogenated silicon has the added benefit of diffusing hydrogen up to 3μm into the semiconductor, reducing bulk defects as well.

2.8 Light Emitting Diodes

At the abrupt interface of p-type and n-type material, with donor concentration N_D and acceptor concentration N_A, we can consider all the dopants ionised such that the free electron concentration is given by $n = N_D$ and the free hole concentration is given by $p = N_A$. At the unbiased p-n junction, free electrons supplied by the donor atoms diffuse over to the p-type region where they recombine with a hole, a corresponding process occurs with holes diffusing into the n-type region. With the free carriers near the junction depleted the ionised donors and acceptors produce spatially separated electrical charges. The separated charges result in an electric potential known as the diffusion

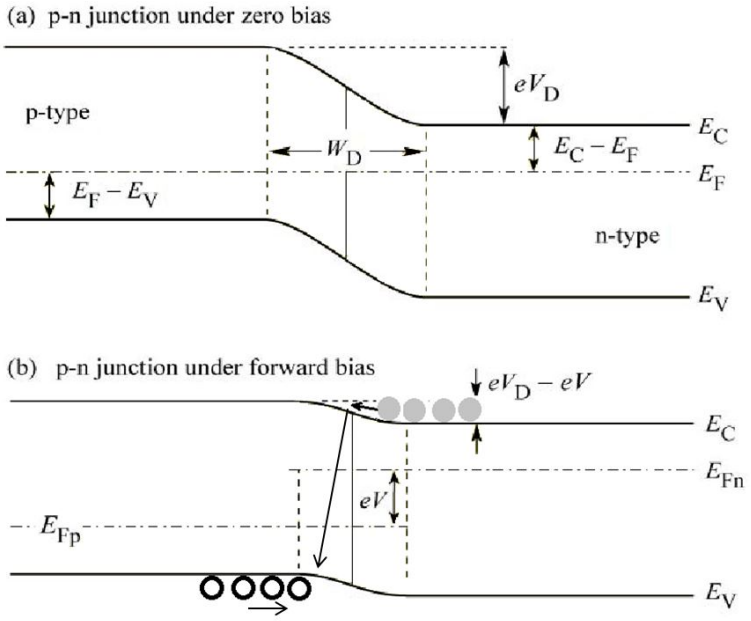

Figure 2.10: (a) An unbiased p-n junction showing the diffusion voltage (V_D) and depletion region width (W_D). (b) The same p-n junction under a forward bias (V) electrons are light grey and holes are hollow circles[14].

voltage (V_D) which stops further diffusion and has a value which is given by[13];

$$V_D = \frac{kT}{e} ln \frac{N_A N_D}{n_i^2} \tag{2.29}$$

where N_A and N_D are the acceptor and donor concentrations, respectively, k is the Boltzmann constant, T is the temperature, e is the charge of an electron and n_i is intrinsic carrier concentration. These properties are illustrated in Figure 2.10. Between the two regions there are no longer free carriers, this region is known as the depletion region. The width of this region (W_D) is given by[14];

$$W_D = \sqrt{\frac{2\epsilon}{e} (V_D - V) \left(\frac{1}{N_A} + \frac{1}{N_D} \right)} \tag{2.30}$$

where ϵ is the permittivity of the semiconductor and V is the bias voltage. This can be seen in Figure 2.10.

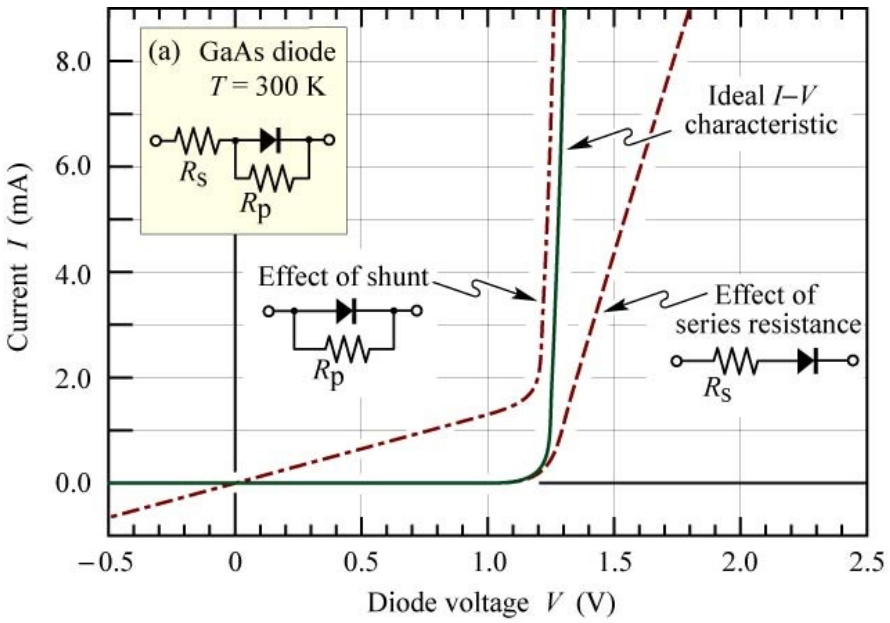

Figure 2.11: The effect of series and parallel (shunt) resistances in the current voltage relation of an LED[14].

Under forward bias the depletion region is injected with electrons and holes, electrons in the n-type and holes in the p-type. They diffuse through to the depletion region before eventually recombining once spatially close enough and producing a photon. As the bias voltage is increased the current flow increases. The diode equation (2.31) was first developed by Shockley and is thus known as the Shockley equation[25]:

$$I = I_s \left(e^{e(V-V_D)/kT} - 1 \right) \tag{2.31}$$

where I_s is the reverse bias saturation current.

In real diodes there are several deviations from an ideal diode equation, these are shown in equation 2.32. An ideality factor n_{ideal} is required. In a perfect diode all current would be due to diffusion, this would give an ideality factor of 1, the presence of recombination and generation of carriers results in a value of 2. A typical diode has values of $n_{ideal} = 1.1 - 1.7$ being a combination of diffusion and carrier generation

and recombination. The ideal diode equation also doesn't take into account any unwanted resistances, these can either be series or parallel resistances. Series resistances are caused by excessive contact resistance or the neutral regions of the device. Parallel resistances occur when a current can bypass the p-n junction either through defects such as threading dislocations or surface imperfections. The effects of these resistances on the IV characteristics of an LED are shown in Figure 2.11, including these gives us a relation;

$$I - \frac{(V - IR_s)}{R_p} = I_s \left(e^{e(V-IR_s)/n_{ideal}kT} \right) \tag{2.32}$$

2.8.1 Efficiency

Not all of the power supplied to an LED produces useful light. Not all carriers recombine to produce photons and not all photons escape the semiconductor before being reabsorbed. The prevalence of these two processes is indicated by the values of efficiency used when discussing LEDs, internal and external. The internal quantum efficiency of an LED is defined as the number of photons produced divided by the total injected carriers.

$$\eta_{\text{internal}} = \frac{\text{photons emmitted in active region}}{\text{carriers injected into active region}} \tag{2.33}$$

Not all light that is produced within the LED is emitted, due to the difference in refractive indices between the semiconductor and air. Only a small fraction of produced light is usable, this is known as the extraction efficiency.

$$\eta_{\text{extraction}} = \frac{\text{photons emmitted into free space}}{\text{photons emitted in active region}} \tag{2.34}$$

Extraction efficiency is limited by two refractive index dependant processes, the critical angle and the internal reflection of light. The critical angle is when the emitted light reaches the surface at such an angle (ϕ_c) that it is diffracted back into the semiconductor

($\Phi = 90°$). Using Snell's law for materials of different refractive indices this gives,

$$\overline{n}_s \sin\phi = \overline{n}_{air} \sin\Phi \tag{2.35}$$

$$\sin\phi_c = \frac{\overline{n}_{air}}{\overline{n}_s} \sin 90° = \frac{\overline{n}_{air}}{\overline{n}_s} \tag{2.36}$$

thus;

$$\phi_c = \arcsin \frac{\overline{n}_{air}}{\overline{n}_s} \tag{2.37}$$

where $\overline{n}_s$ is the refractive index of the semiconductor.

The light emitted within the critical angle is also subject to reflection as defined by the Fresnel equation,

$$R = \left| \frac{n_{air} - n_s}{n_{air} + n_s} \right|^2 \tag{2.38}$$

where R is the reflection coefficient.

By combining equations 2.37 & 2.38 we get the extraction efficiency and by combining the internal quantum efficiency and the extraction efficiency we get the external quantum efficiency,

$$\eta_{\text{external}} = \eta_{\text{internal}} \eta_{\text{extraction}} = \frac{\text{photons emmitted into free space}}{\text{carriers injected into active region}} \tag{2.39}$$

Wall plug efficiency (η_{wall}) has been taken as a figure of merit in this work. It is calculated as the output power of the LED divided by the supplied power (adjusted for duty cycle);

$$\eta_{wall} = \frac{P_{out}}{IVD_c} \tag{2.40}$$

where I is the supplied current, V the voltage and D_c duty cycle. This was chosen because, in interest of energy efficiency, it is the total power supplied that is important. This measure allows the effective comparison of cascading devices and other devices

which utilise carrier recycling.

2.9 Strain

When a semiconductor film is deposited on a substrate to which it is not lattice matched the deposited layer is deformed to conform with the substrate. When the lattice constant of the film (a_{film}) is greater than the substrate lattice constant (a_0) then there is compressive strain which reduces the lattice constant perpendicular to the growth direction and increases it in the growth direction. If $a_{film} < a_0$ then the opposite occurs and it is known as tensile strain.

2.9.1 Dislocations

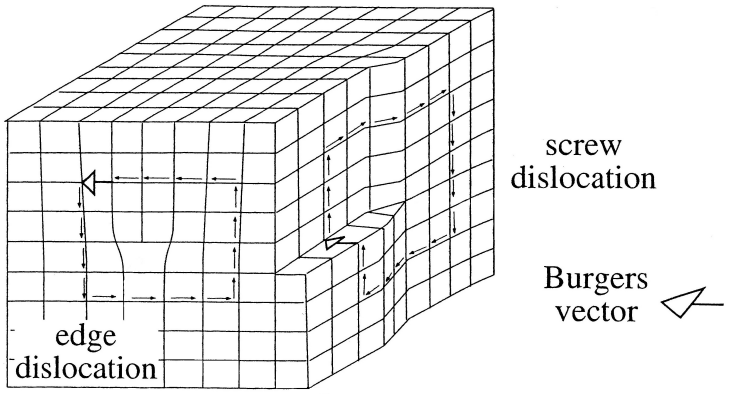

Figure 2.12: Example of the Burgers vector of edge and screw dislocations[26].

Dislocations are abrupt changes in the regular ordering of atoms along a dislocation line. Dislocations are mostly due to the misalignment or vacancy of atoms. These can be caused by impurities and strain deforming the lattice structure. Two such types of dislocation are edge dislocations ($\vec{b}\perp$) and screw dislocations ($\vec{b}\|$). These dislocations are defined by their Burgers vector $\vec{b}$ which indicates the slip distance of the lattice in terms of magnitude and direction (Figure 2.12). An edge dislocation is perpendicular to

the Burger vector and a screw dislocation is parallel to it. In real crystals however most dislocations are of a mixed edge/screw nature.

2.9.2 Critical Thickness

As the epitaxial layer increases in thickness the strain energy density increases until it is in coincidence with the interfacial energy allowing the generation of dislocations at the interface. There have been several attempts at calculating the critical thickness (h_c) at which this occurs.

Firstly Frank and van der Merwe stipulated in 1962 [27] that critical thickness could be calculated using;

$$h_c \cong \frac{1}{8\pi^2}\left(\frac{1-\nu}{1+\nu}\right)\frac{a_0}{f} \tag{2.41}$$

where a_0 is the lattice constant of the substrate, f is the lattice mismatch and $\nu = C_{12}/(C_{11}+C_{12})$ is Poisson's ratio, where C_{11} and C_{12} are the elastic constants of the epitaxial layer.

This was further developed by Matthews and Blakeslee [28] who took into account the slippage of the lattice when a defect is formed, the Burgess Vector (b) resulting in;

$$h_c \cong \left(\frac{b}{f}\right)\left[\frac{1}{4\pi(1+\nu)}\right]\left[ln\left(\frac{h_c}{b}\right)+1\right] \tag{2.42}$$

People and Bean [29] considered the case where the dislocations were not produced at the interface but isolated within the epitaxial layer. To this end they considered screw dislocations due to their low formation energy compared to other dislocations resulting in;

$$h_c \cong \left(\frac{1-\nu}{1+\nu}\right)\left(\frac{b^2}{16\pi\sqrt{2}a(x)f^2}\right)\left[ln\left(\frac{h_c}{b}\right)\right] \tag{2.43}$$

where $a(x)$ is the lattice constant of the epitaxial layer.

2.9.3 Strain Induced Band Shift

The effects of compressive strain as seen in GaInSb/(Al)GaSb quantum wells and InAs/InGaAs quantum dashes can be seen in Figure 2.13. In a quantum well compressive strain would occur in the growth direction and thus across the quantum well. In this case the heavy hole band is lifted in energy, separating it from the light hole band.

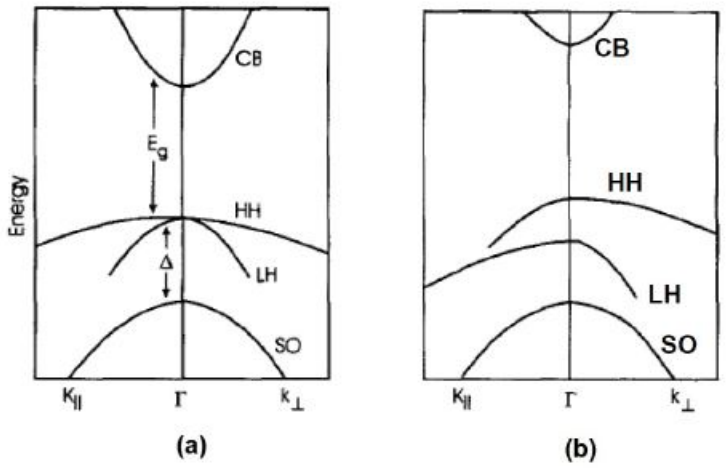

Figure 2.13: Effect of strain on the band structure of a material (a) Unstrained band structure (b) Under bi-axial compressive strain[30].

Krijn [31] calculated the change in band offsets, starting with strain inherent lattice mistamched growth - biaxial strain $\epsilon_{||}$ parallel to the interface and uniaxial strain $\epsilon_\perp$ perpendicular to it:

$$\epsilon_{||,\perp} = \frac{a_{||,\perp}}{a} - 1 \tag{2.44}$$

where

$$a_{||} = a_0 \tag{2.45}$$

and

$$a_\perp = a\left[1 - 2\frac{C_{12}}{C_{11}}\left(\frac{a_{||}}{a} - 1\right)\right] \tag{2.46}$$

where a_0 is the lattice constant of the substrate, a is the equilibrium lattice constant of the epitaxial layer and C_{11} and C_{12} are the elastic constants of the epitaxial layer.

The shift in the conduction band is taken as

$$\Delta E_c = a_c(2\epsilon_{\parallel} + \epsilon_{\perp}) \tag{2.47}$$

where a_c is the conduction band hydrostatic deformation potential. For the valence band the energies are shifted not only by the hydrostatic component,

$$\Delta E_v^{hy} = a_v(2\epsilon_{\parallel} + \epsilon_{\perp}) \tag{2.48}$$

where a_v is the valence band hydrostatic deformation potential, but also a shear contribution which splits the valence band energies by;

$$\Delta E_{hh}^{sh} = -\frac{1}{2}\delta E^{sh} \tag{2.49}$$

$$\Delta E_{lh}^{sh} = -\frac{1}{2}\Delta_0 + \frac{1}{4}\delta E^{sh} + \frac{1}{2}\left[\Delta_0^2 + \Delta_0\delta E^{sh} + \frac{9}{4}\left(\delta E^{sh}\right)^2\right]^{1/2} \tag{2.50}$$

$$\Delta E_{so}^{sh} = -\frac{1}{2}\Delta_0 + \frac{1}{4}\delta E^{sh} - \frac{1}{2}\left[\Delta_0^2 + \Delta_0\delta E^{sh} + \frac{9}{4}\left(\delta E^{sh}\right)^2\right]^{1/2} \tag{2.51}$$

where

$$\delta E^{sh} = 2b(\epsilon_{\perp} - \epsilon_{\parallel}) \tag{2.52}$$

is the shift due to strain, b is the tetragonal shear deformation potential and Δ_0 is the spin-orbit splitting in the absence of strain. The total shift in the valence band can thus be shown to be :

$$\Delta E_{v(hh,lh,so)} = \Delta E_v^{hy} + \Delta E_{hh,lh,so}^{sh} \tag{2.53}$$

The strain induced shift in the SO band energy can be used to suppress the CHSH process by increasing the activation energy and thus reducing the rate. Compressive

strain also reduces the effective mass in the valence band, and this modifies the dispersion relation for the valence band reducing the rate of both Auger recombination and intervalence band absorption[32].

2.10 High Lattice Mismatch Growth

Despite the increased probability of dislocations, it is possible to grow structures on substrates with a high degree of lattice mismatch. One way to achieve this has been to gradually change the lattice constant of the deposited layer in a series of graded steps between the original lattice constant and the desired final one[33, 34]. This is known as a metamorphic buffer layer, growth of this layer can be time consuming and its thickness, which is typically several microns can be undesirable.

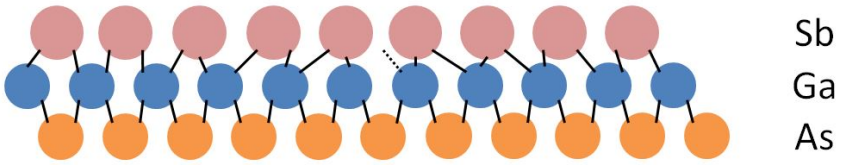

Figure 2.14: Atomic arrangement at IMF interface, with dangling bond indicated by dashed line.

Another method pioneered by D Huffaker *et al.*[35] at University of New Mexico, known as Interfacial Misfit (IMF), involves growing an abrupt interface between the substrate and a compressively strained epilayer. This growth technique has been shown to relieve 98.5% of strain at the interface of GaAs/GaSb. Defect densities of $< 10^5/\text{cm}^2$ have been achieved on 5 μm GaSb layers. This allows for high quality GaSb based devices on GaAs.

An IMF is achieved by first growing a buffer of GaAs. The growth is then paused without an As flux which results in a Ga terminated surface. An Sb flux is then intro-

duced and growth of GaSb follows. Due to the difference is lattice constant between GaSb and GaAs every 13 GaSb latticesites there is a dangling bond as 13 GaSb units have the same separation as 14 GaAs units as demonstrated in Figure 2.14. Investigation of these interfaces using High Resolution Transmission Electron Microscopy (HR-TEM) indicate that the Burger's vector lies along the interface, indicating that the defects are in fact 90°with respect to the growth direction.

Chapter 3

Literature Review

3.1 Introduction

This chapter examines the various material systems that can be utilised to achieve emission in the 2 μm region. This includes bulk heterostructures; often grown by Liquid Phase Epitaxy (LPE) and quantum well, quantum dot and quantum dash samples grown my Molecular Beam Epitaxy (MBE) and Metalorganic Vapour Phase Epitaxy (MOVPE). Also included is a discussion of the use of metamorphic epitaxy as a means of increasing the degrees of freedom in device design.

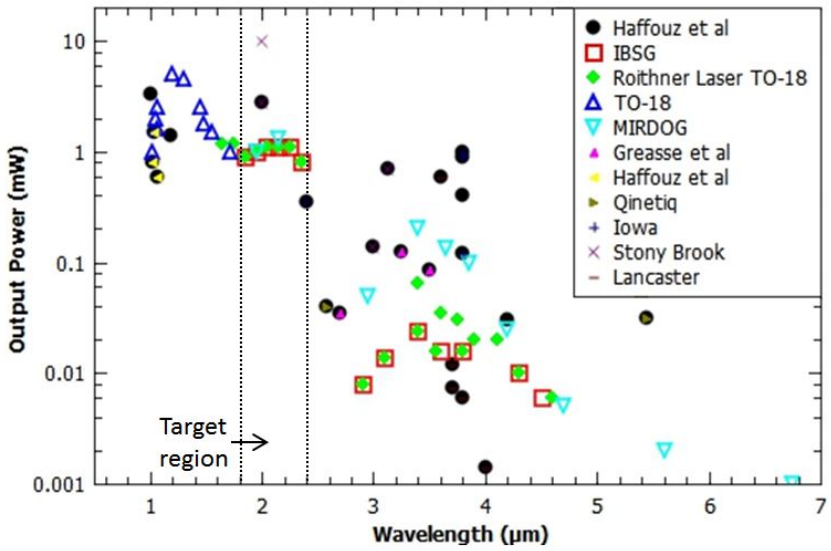

Figure 3.1: A comparison of LED devices with their absolute output power as reported in the literature, open points are quasi-CW(50% duty cycle 1 kHz[qCW]) and filled points are CW[36, 37, 38, 39, 40, 41, 42, 43, 44].

It is typically found that there is a decrease in output power as wavelength is extended (Figure 3.2), this is due, in part, to increased Auger recombination rates which increase by 3 orders of magnitude between GaAs (870 nm) and InSb (7.2 μm) due to reducing effective masses of carriers[45]. This results in the decreased efficiency of the LED. Even if efficiency remained constant at longer wavelengths, the reduced energy per photon would decrease the output power for devices with equal drive currents. Light extraction is also

more challenging at longer wavelengths, epoxy encapsulation to gradate the refractive index and reduce reflection (as outlined in Equations 2.37 & 2.38) no longer works as the epoxy is not transparent to Mid-IR and more exotic glasses are needed.

A direct comparison of infrared LEDs can prove difficult as literature reported values have no commonly agreed parameters. For example there are large deviations in emission area, drive current, operating temperature, duty cycle and integrated area. This is because the varied uses of MIR-LEDs prioritise different figures of merit dependent on the intended application. Some applications, such as gas sensing require narrow linewidth. Night vision compatible lighting needs high efficiency and output power. Where space is a factor or out-coupling to optical fibres is important, such as telecommunications, high brightness is a priority. Test conditions are selected to maximise favoured figures of merit. However, in some cases the operating parameters may not be suitable for real-world application. Reports of relatively high power may in large part be due to larger area devices. Similarly, relatively high efficiencies may be reported at lower than practical currents, before non radiative processes such as Auger recombination become major factors.

With an aim to more accurately compare output power of devices, light intensity was normalised against test conditions (Figure 3.2). Light intensity is integrated over a hemisphere and scaled to a constant emitting area and drive current. The dashed red line indicates the theoretical limit of an LED with 100% external efficiency. This theoretical maxima cannot be achieved due to extraction efficiency and non-radiative processes such as Auger recombination. Devices beyond the trend line are cascade devices in which carriers are recycled, boosting the apparent efficiency. However, this is not the actual case as the wall plug efficiency remains unchanged compared to single stage devices; this is due to the increased drive voltage required to operate cascade devices.

The comparison of devices is not typically an issue with visible LEDs as they have much higher luminosity, higher efficiency and standardised photometric definitions which

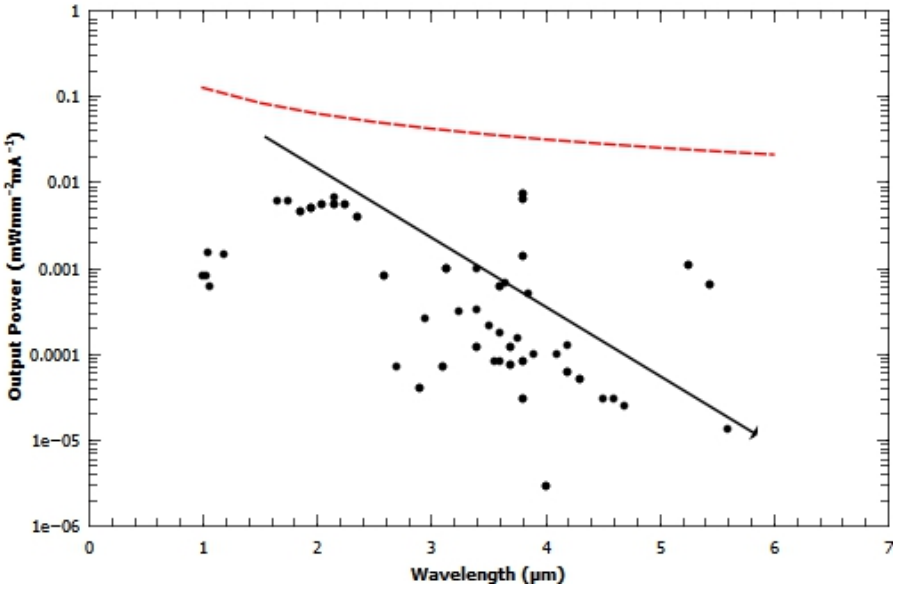

Figure 3.2: A comparison of LED devices from Figure 3.1, normalised to current and emitting area and integrated over 2π steradians. The dashed red line indicates the theoretical limit of the 100% conversion and extraction of LEDs. A trend line in included to guide the eye.

can easily be converted to radiometric values[46]. Infrared LEDs also use radiometric measurements but lack comparable photometric definitions.

3.2 Bulk Alloy LEDs

Using Liquid Phase Epitaxy (LPE), a collaboration between the Ioffe Institute and the Quantum Nanotechnology group at Lancaster University, conducted an in depth and wide ranging study into LEDs based on GaSb alloys in the spectral range of 1.6-4 μm [47, 48, 49, 50, 51, 52]. The currently commercially available devices of this type, produced by IBSG[36], Roithner[38] and MIRDOG[37] are included in Figure 3.1.

A.A. Popov *et al.*[51] presented an example of an LED device operating at 2.2 μm. This device was based on an InGaAsSb alloy. The composition was chosen to ensure it remained lattice matched to the GaSb whilst also selecting an appropriate band gap.

Heterojunctions in the system result in type I confinement of both carriers. Testing indicated that band symmetry around the active region (barrier layers on both sides of the active region) is important in achieving the maximum output power whilst also reducing the width of emission spectrum. Optimum active region design in these double heterojunctions LEDs has a thickness of a 2-3 μm. This thickness is comparable to the carrier diffusion length. As indium content increases in GaInSb, the carrier lifetime decreases reducing the required active region thickness.

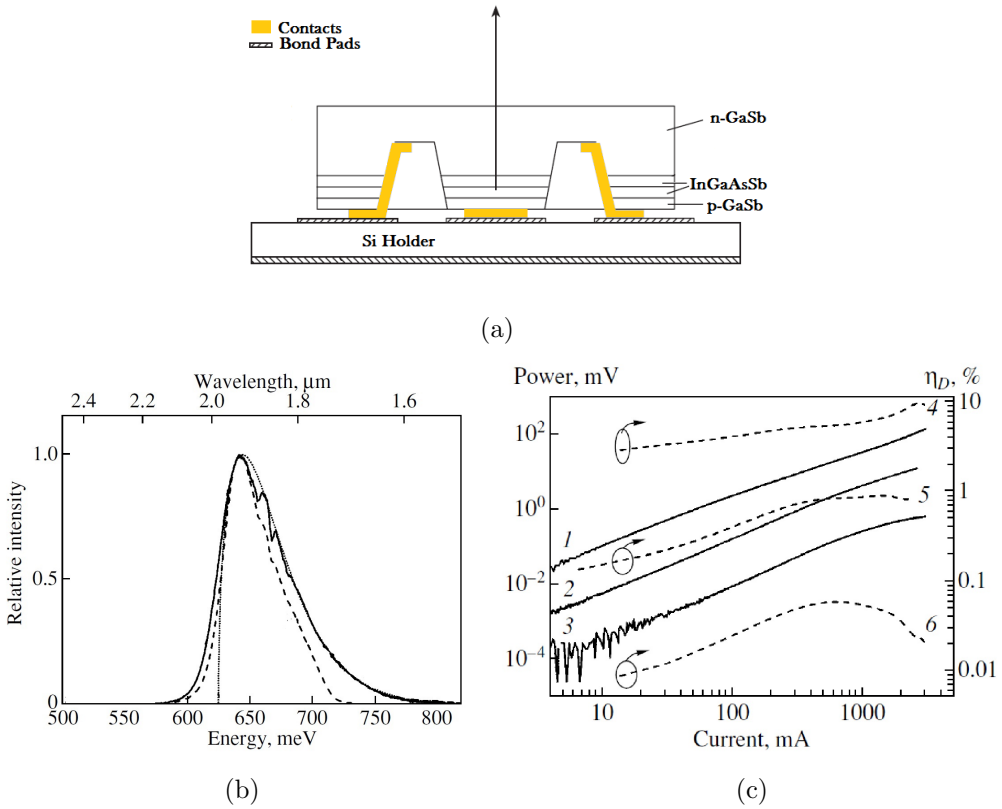

Figure 3.3: (a) Schematic of a 'flip-chip' LED as used by the Ioffe Institute. The arrow indicates the direction of light emission.
(b) Spectra of a flip-chip LED (dashed line) compared with a top bottom contacted LED of the same material (solid line) with the calculated spectra (dotted line) for reference.
(c) Output power (1-3) and external quantum efficiency (4-6) as a function of pump current at 77 K (1,4), 297 K(2,5) and 453 K (3,6)[53].

To reduce the reabsorbtion by the p-type region, a 'flip-chip' design was investigated by Zotova *et al.*[53]. The schematic of one such device is shown in Figure 3.3a.

By flipping the chip, the heat generating active region is closer to the heat removing casing, reducing the effect of Joule heating with increased current. Additionally, the light is extracted through the wider gap n-type region, decreasing reabsorption. This coupled with patterning of the surface with conical pyramids resulted in external quantum efficiencies of 6% and output powers of 2 mW at 1.94 μm [54]. Increased output from this device was limited by the CHCC Auger process.

Due to the limitations of LPE, it is not possible to produce GaInAsSb with In content from 25-70%. This is due to what is known as the miscibility gap: from 25-70% indium the alloys of GaInAsSb do not form a homogeneous solution, precluding the controlled grown of homogeneous semiconductors. Subsequently LPE grown heterostructures made from alloys of GaInAsSb are limited to wavelengths of 1.6-2.4 μm and 3.4-4.4 μm.[55, 56] It is also possible to implement macroscopic structural improvements to the device that improved light output; these include the use of parabolic reflectors which collimated the light into an angle of $\sim$12°. Encapsulation with an epoxy compound, further improved extraction efficiency by reducing internal reflection and increasing the light emission cone by reducing the refractive index mismatch at the interface. Such encapsulates are of limited use at wavelengths greater than 2 μm however, as the availability of optically transparent epoxies at or beyond this region is limited and the improved extraction efficiency realised by this technique will be offset by increased absorption. It is possible to use glasses such as zinc sulphide but these are particularly difficult to achieve[57].

The development of pentanary or quinternary alloys has allowed for the production of improved LED designs[58, 59, 60, 61, 62]. The addition of a further element to the alloy gives further degrees of freedom when selecting a specific bandgap. For example, for a given bandgap or lattice constant, it become possible to independently vary factors such as the band alignment (electron affinity), refractive index and spin-orbit valence band

splitting[63]. This enables the independent control of the confinement, both optically and of the carriers, along with suppression of intervalence band absorption and Auger recombination[64].

3.3 GaIn(As)Sb/(Al)GaSb Multi Quantum Wells

Whilst possible to grow quantum scale structures with LPE[65], MBE is more suited to the growth of nanometre scale epilayers. The use of quantum wells has many benefits over bulk materials; as the carriers are confined spatially by the potential of the barrier material, they are physically close to one another, increasing the likelihood of recombination. The controlled introduction of strain can also be used to engineer the band alignment and suppress undesired Auger recombination by shifting the relative positions of the bands (as outlined in Section 2.9.3) and decreasing the hole effective mass [32].

Examples of GaInSb/GaSb quantum well LEDs can be found in the work of A.N. Baranov *et al.*[66], achieving electroluminescent emission at wavelengths up to 2.17 μm at room temperature from a single quantum well. In this work $Al_{0.5}Ga_{0.5}Sb$ barriers were used to improve the confinement of the carriers. As both the barriers and the wells are lattice mismatched the number of wells is limited before critical thickness is reached. This is calculated using the methods outlined in Section 2.9.2.

At a high indium content, the critical thickness is reduced such that any reduction in band gap from additional indium incorporation is offset by the increased energy of the confined states due to the smaller quantum well size. To illustrate this nextnano® was used to simulate a series of quantum wells with indium compositions from 15% - 45%. Well widths were chosen up to the critical thickness, calculated using the People & Bean method[29]. Those that showed carrier confinement less than kT are excluded. This can be seen in Figure 3.5. At high indium concentrations (45% and higher) the wells need to be wider than the critical thickness to maintain confinement of the carriers. It

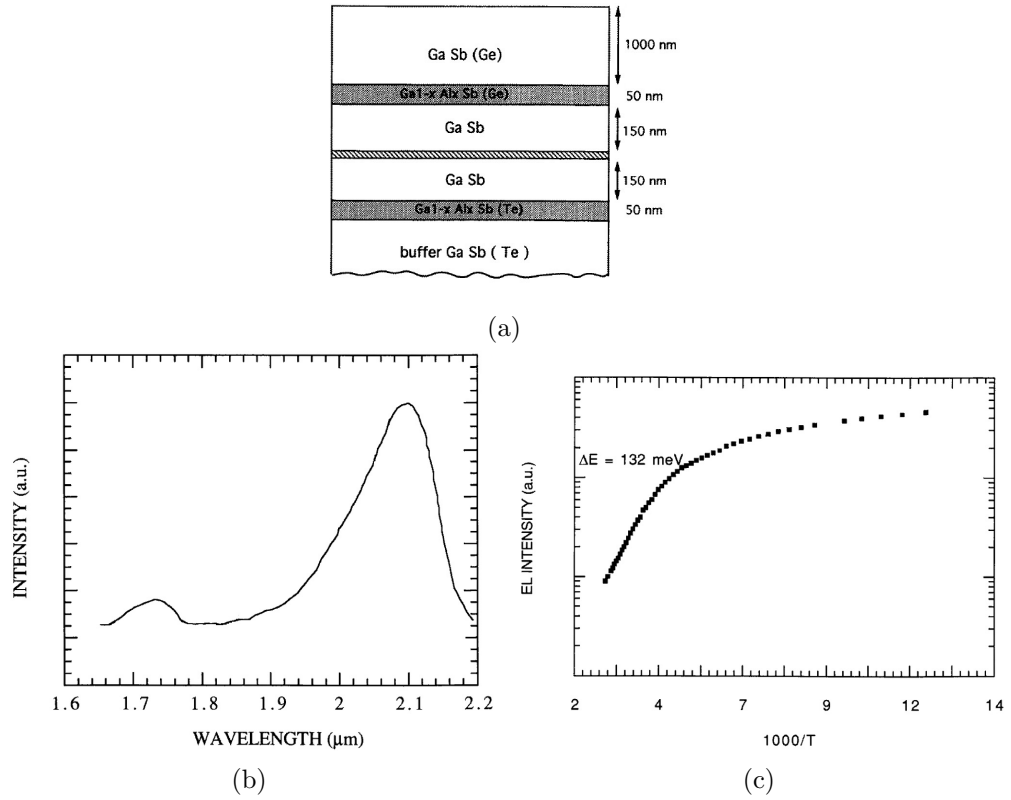

Figure 3.4: (a) Schematic diagram of LED reported by AN Baranov *et al.*[66]. The quantum well consists of 6 nm of $Ga_{0.65}In_{0.35}Sb$. (b) Room temperature emission spectrum of LED) with a drive current of 50 mA qCW. (c) Activation energy of LED showing quenching is due to thermionic emission of the carriers from the QW ground state.

should be noted that the People & Bean estimate of the critical thickness is regarded as generous and there is no evidence of GaInSb quantum well devices with more than 35% indium. This is in contrast with the Matthews & Blakeslee[28] estimate which calculates a critical thickness well below the value at which quantum wells have been shown to grow without relaxing. An investigation into the critical thickness of $Ga_{(1-x)}In_xSb$ ($x < 0.2$) grown on GaSb specifically was conducted by T.A. Nilsen *et al.*[67]. This work found critical thicknesses approximately 2.5 times greater than those predicted by Matthews & Blakeslee, but well below those predicted by People & Bean. Using the thickness limit suggested by Nilsen *et al.*, a 35% indium quantum well would be limited to around

2.25 μm emission.

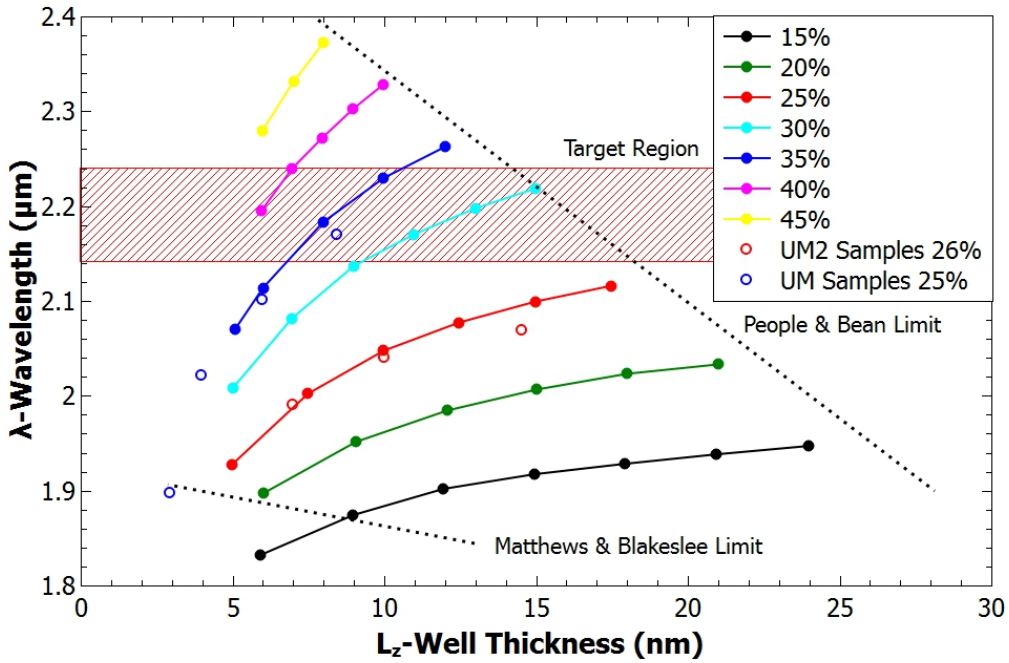

Figure 3.5: Simulated emission wavelengths of $Ga_{(1-x)}In_xSb$ quantum wells of varying thickness. Data is plotted for well thickness between where carriers are confined up until the critical thickness as calculated using the method prescribed by People & Bean[29]. Data from the work of Baranov *et al.* [66] is also included as open points.

To extend beyond 2.25 μm, it is necessary to increase the indium content further. Arsenic is incorporated to compensate for the increased strain and allow quantum wells below the critical thickness to have confined states. Typically this is around 2% arsenic and helps to reduce the lattice mismatch between the barriers and wells[68]. The addition of arsenic also strongly reduces the hole confinement within the quantum wells [44]. This is problematic as it increases the rate of thermal quenching due to loss of carrier confinement, which is needed for room temperature operation.

S. Suchalkin *et al.*[69] considered two different approaches to compensate for the reduced confinement. First was the use of $Al_{0.5}Ga_{0.5}Sb$ barriers to increase the overall confinement. It was realised that reducing the Al content of the barriers from 50% to

35% further improved the confinement. Despite a lesser total barrier offset, the increased electron affinity of the reduced Al barriers improved the valence band offset. Secondly, the use of quinternary AlGaInAsSb gave the additional degree of band gap freedom to adjust strain and valence band offset independently. The quinternary material produced an emission of 3.3 μm, superior to the AlGaSb barriers. Although the authors do not elaborate on the cause of this, it is possible it is due to the difficulty of producing high quality high aluminium content materials.

The introduction of mixed group-V alloys in MBE presents a challenge. During MBE growth it is possible for the group-V flux to vary, as can the substrate temperature. This is not a concern in mixed group-III materials, as there is an excess of group-V it does not influence the composition or thickness of the alloy. In mixed group-V alloys the two group-V species compete to incorporate; the rates at which they do so are dependant upon multiple factors including the relative fluxes and the substrate temperature. This can result in graded compositions as the substrate temperature varies with deposition thickness. To eliminate the complexity and calibration required to achieve the desired group-V ratio, a growth technique known as Digital Alloying or Modulated MBE was developed[70, 71, 72, 73]. This involves the rapid shuttering of the different binary compositions that constitute the desired alloy. This in effect produces a short period - typically less than 10 ML - superlattice which has a composition intermediate to the two component layers. This provides for greater control of the composition of the epilayers and also allows for the controlled gradating between compositions, which is useful in reducing discontinuities in the band profile.

GaSb is not the only substrate on which 2 μm light emission can be achieved[75, 76]. M.C. Amann *et al.*[77, 74] have produced several devices on InP substrates. These devices utilise the type-II band alignment seen in $GaAs_{0.51}Sb_{0.49}/Ga_{0.25}In_{0.75}As$ to produce a superlattice. The devices were grown using MOVPE and processed as micro-cavity LEDs, the emission can be seen in Figure 3.6a along side the emission power (Figure

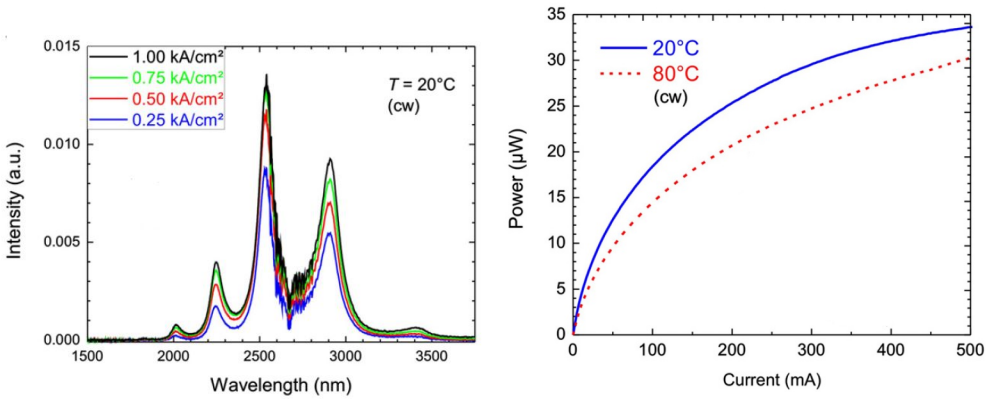

(a) (b)

Figure 3.6: (a) Spectra of type-II GaInAs/GaAsSb LED with emission of 2.6 μm grown on an InP substrate. (b) Room and high temperature current power curves for type-II GaInAs/GaAsSb LED[74].

3.6b). The distortions on the spectra at 2.7 μm are due to water absorption.

The use of a type-II superlattice proved advantageous for high current density operation as there was no indication of type-I transitions in either layer in the superlattice even at current densities of 1 kA/cm^2. Additionally the use of type-II transmission was shown to suppress Auger recombination as evidenced by the CW drive operation up to a temperature of 80 °C. This is a higher temperature than seen in other CW devices[74].

3.4 Quantum Well Cascade LEDs

To further increase the output power of quantum well devices S. Jung *et al.* applied the principles of cascading multiple active regions within a single device with 12 nm $In_{0.2}Ga_{0.8}Sb$ quantum wells [39]. All layers in the device were lattice matched to GaSb, excluding the quantum wells which were compressively strained to increase the valence band offset. The InGaSb wells were contained within $Al_{0.3}Ga_{0.7}As_{0.024}Sb_{0.976}$ spacers, which together, comprise the active regions. Carriers were confined to these regions by $Al_{0.85}Ga_{0.15}As_{0.068}Sb_{0.932}$ barriers. These devices also utilised a 'flip chip' design. The

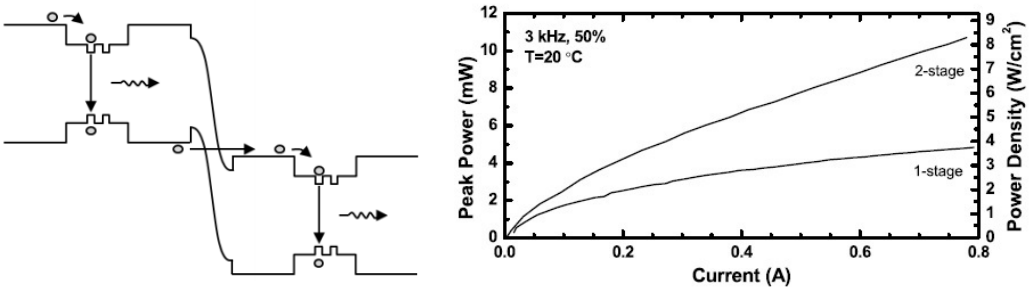

(a) (b)

Figure 3.7: (a) Band diagram of a two stage quantum well cascade laser as reported by Jung *et al.* [39]. (b) Power output of the single stage device and two stage cascade device showing the more than doubled output power of the 2-stage device.

substrate was lapped to reduce the thickness and the devices were mounted on copper blocks for thermal anchoring.

Devices with one and two active regions (design shown in Figure 3.7a) were tested over a range of injection currents. A power output of 5 mW was achieved from the single stage device. The two stage device achieved more than double that of the single stage device, 11 mW, at the same current (Figure 3.7b). At 4 mW, the wall plug efficiency (total power emitting divided by electrical power supplied) of each device was calculated as 0.36% and 0.51% for the single and two stage devices, respectively. The improved efficiency of the two stage device was attributed to the reduced carrier density in each quantum well resulting in a lower Auger recombination rate. J.P. Prineas *et al.* at University of Iowa have shown similar results further supporting cascade devices as a strong contender for producing high power output[78].

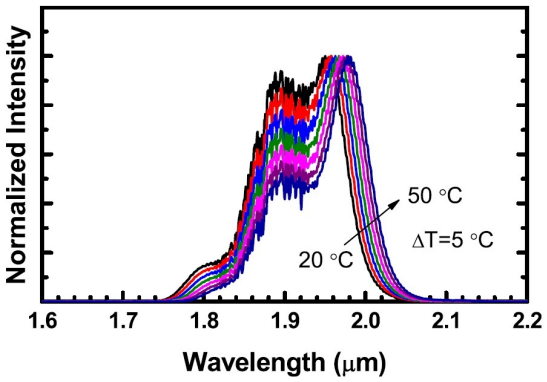

Figure 3.8: Spectrum of 2 stage cascade LED with a drive current of 50 mA with 5% duty cycle. The feature at 1.9 μm is due to a gallium mismatch between the 2 active regions[39].

3.5 InSb/GaSb Quantum Dots

InAs/GaAs quantum dots (QDs) have been comprehensively researched due to their ease of growth and useful emission for optical communication systems. The use of dots in active regions possess desirable properties, such as high temperature stability. However, it is not possible to extend the wavelength of InAs/GaAs QDs to 2 μm. To achieve longer wavelength emission, it is necessary to utilise a narrower gap material such as InSb. The properties of InSb dots are less well explored for two reasons. Firstly, the optimum growth temperatures of InSb and GaSb are greatly different making optimised growth difficult. Secondly, indium has a high mobility on antimony terminated surfaces. This results in the rapid formation of threading dislocations to relax the strain, reducing optical quality and increasing defect related non-radiative processes [79]. MBE growth of InSb/GaSb QDs by the standard Stranski-Krastanow (SK) method is seen to begin at 1.7 ML of InSb coverage[80, 81]. This growth method resulted in a wide distribution of heights, up to 15 nm (Figure 3.9(a)) with densities of 4×10^{9} cm^{-2} and diameters ranging from 40-80 nm. Given the large dimensions of these dots, the probability that they will contain a defect is increased. Defect containing dots are undesirable as they confine

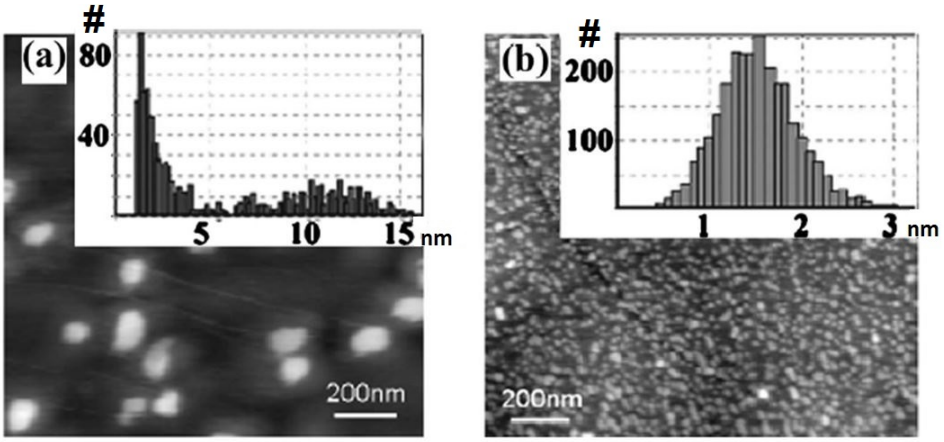

Figure 3.9: AFM images of (a) 2.6ML InSb QDs grown by SK mode and (b) two stage deposition and annealing. Insets show histograms of the dot heights[79].

carriers to a region with increased non-radiative recombination. Defects are prevalent in SK mode InSb/GaSb dot formation as this has been shown to involve total relaxation concurrent with the transition between 2D-3D growth [82].

Ya. A. Parkhomeenko *et al.* at the Ioffe Physical-Technical Institute have also achieved the growth of InSb quantum dots on GaSb using LPE[83]. These dots were grown on a surface of GaSb and not capped but this provides further insight into the growth of InSb dots. The growth temperature of InSb dots is independent of the growth technique and instead determined by the lattice mismatch between the materials. The InSb/GaSb dots formed by LPE are significantly flatter than those seen in the InSb/InAs when also produced using LPE. The InSb/GaSb dots have a height to diameter ratio almost a third of that of InSb/InAs[84]. The dependence of the InSb dot formation on the epilayer they are deposited on and the variance in shape between InAs and GaSb surfaces, opens the possibility of control of the morphology of the quantum dots by varying the composition of the surfaces. Such morphology control has previously been shown in the InSb/InAs(Sb,P) system[85].

MOVPE growth of InSb/GaSb quantum dots by E. Alphandéry *et al.* indicates SK

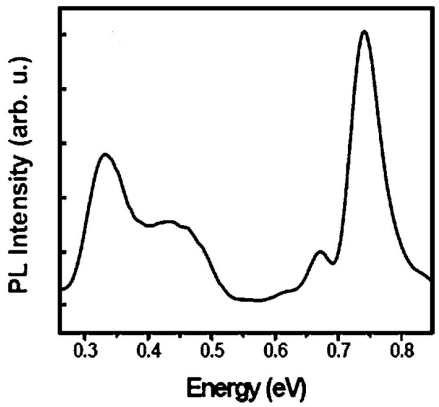

Figure 3.10: 90 K PL emission spectra of InSb/GaSb QDs. Peaks at 360 meV and 500 meV are due to the ground and first excited states of the QDs. The higher energy peak is due to recombination in the GaSb[79].

mode formation of dots at 2-5 ML of InSb[86]. Thicker InSb deposition results in further extension of wavelength but a rapid decrease in photoluminescence intensity, this is attributed to the introduction of dislocations. Dot dimensions from the optimal growth conditions in this work were heights of 4 nm and aspect ratios of 0.08 as confirmed by Magneto-PL. AFM images show dot with heights ranging from 0.6 nm to 11 nm with dots becoming flattened at 7 nm indicating they have become relaxed.

As SK mode growth depends upon strain for dot formation, the combination of substrate and dot material is limited to materials with sufficient lattice mismatch. There is also a minimum dot size below which only a wetting layer is formed. To overcome these limitations and achieve high density growth of uniform dots, non-standard growth methods are required.

One such novel method is the MBE growth of InSb below the condensation temperature of antimony. This produces a polycrystalline layer a few monolayers thick, which is then annealed, resulting in a much smaller dot, (13±3) nm wide with a height of 1-3 nm but with far greater uniformity than those seen in SK mode MBE growth (Figure 3.9(b)). Capped with further GaSb, these samples achieved PL emission at 3.5 μm. A four fold decrease in intensity between 4 K and 300 K indicates good thermal stability.

Another method of growing QDs is the so called submonolayer QD (SML QD). This involves depositing less material than is required to produce a single monolayer which results in the formation of islands of the dot material which can then be encapsulated [87]. SML QDs are desirable as they allow ultra-high densities of dots to be produced[88]. Because strain is not required to produce the dots this method can be used to achieve defect free QDs. High density defect free QDs are desirable because reduced defects reduce SRH recombination and higher densities of dots decreases the carrier density in each dot, reducing the Auger rate increasing luminous efficiency. SML QDs have also been shown to produce narrower emission compared to SK mode growth indicated improved homogeneity in composition and size[89]. There is however, some disagreement as to the nature of submonolayer QDs with some groups considering them localised indium rich QD-like regions within disordered InGaAs quantum wells[90]. Nevertheless, they still offer an effective system of utilising the benefits of QDs, especially in systems where SK mode growth is not possible.

Currently there are no published accounts of devices utilising InSb/GaSb QDs, with studies focusing on the growth, mechanical characterisation and PL analysis as shown in Figure 3.10. In Chapter 5 LEDs using SML InSb/GaSb QD active regions will be developed and their properties explored.

3.6 Quantum Dashes

When InAs quantum dots are grown on $In_{0.53}Ga_{0.47}As$ (lattice matched to InP), they become elongated, maintaining a dot like cross section in the $(1\bar{1}0)$ plane, but extending in the order of 100's of nanometres. This kind of structure has been labelled a Quantum Dash (QDash). Typical dimensions are 20 nm wide, 5 nm high and 300 nm long.

Initial work on InAs dots focused on growth on GaAs substrates, here the lattice mismatch of 7.2% limits the number of monolayers of InAs that can be deposited before

relaxation occurs limiting the size of the dots and restricting them to shorter wavelength applications [91, 92]. By embedding the quantum dots in $In_{0.4}Ga_{0.6}As$ quantum wells J. Tatebayash *et al.*[93] reduced the band gap energy due to a relaxation of the compressive strain and reduced effects of quantum confinement. Moving to InP as a substrate allowed for an increased indium content in the InGaAs layer, $In_{0.53}Ga_{0.47}As$ is lattice matched to InP. By increasing the indium content to 53%, extended emission wavelength was achieved. The lattice mismatch is reduced by a factor of more than 2 to 3.2%, this reduced strain allows for thicker dots to form before relaxing, extending the wavelength. With strain of $\sim 3\%$ the elongation of the dots to dashes is noted[94].

QDashes are relatively new systems and as such the mechanism of growth is currently not well understood, one theory suggested by R.H. Wang *et al.*[95] notes that the growth only occurs on InGaAs(lattice matched to InP). This is in contrast to dot formation seen in InAs grown on lattice matched AlInAs as reported by S. Fafard *et al.*[96]. Fafard also noted similar dot formation resulting from direct growth on InP. Dot formation on AlInAs was also reported by J. Brault *et al.*[97], who attributed this to the reduced diffusion length on AlInAs when compared to GaInAs, this was supported by surface roughness measurements. The dependence of InAs morphology on surface composition, along with AFM observations of dashes preferentially elongating in the $[1\bar{1}0]$ direction. From these observations Wang suggests the theory that the dashes are formed due to the step edges of InAs orientated on a (001) surface. Step edges along $[1\bar{1}0]$ are cation terminated and thus less reactive than the step edges along [110] which being anion terminated are more reactive with indium, increasing the growth rate along this axis. InAs dashes have also been shown to form when grown on high index InP(311)A substrates [99, 100, 101]. Q. Gong *et al.* attributed dash formation in this instance to strain induced growth instability. These samples were designed for the fibre communication at 1.55 μm and whilst InP(311)A substrate does provide another method of growing dashes, the difficulties presented in the processing make this a less favourable approach.

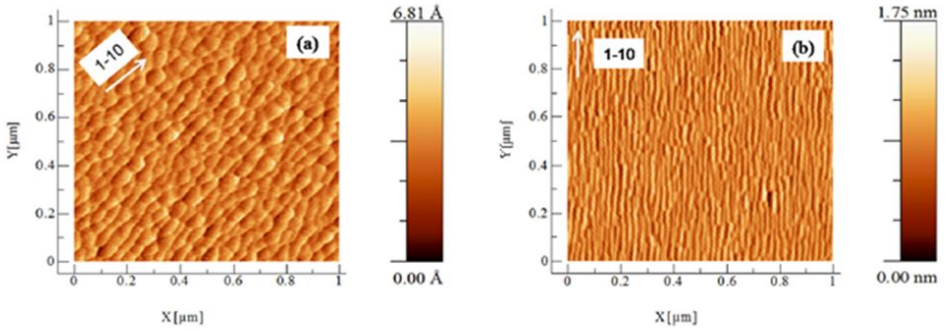

Figure 3.11: AFM scans of InAs QDashes (a) compared with InAs(Sb) QDashes (b) grown under identical growth parameters[98].

Quantum dashes grown on InP(100) have the benefit of accessing the mature processing techniques already developed for telecommunications applications.

Dash growth is favourable as it allows for improved coverage compared to dots. Multiple layers of dashes have been shown to result in inhomogeneous dimensions resulting in broadening of the emission spectrum[102].

Emission wavelength is determined by the confinement in the direction of growth and the composition of the barrier. To extend this wavelength it is necessary to deposit more InAs though this is limited by the ending of dash growth and the proceeding 2D growth, though modelling by K. Papatryfonos indicated 2.5 μm is achievable[103].

Another solution to extended emission wavelength is the addition of Sb into the dashes[98]. This extended the PL emission of the wells out from 2 μm to 2.15 μm, with limited reduction in intensity or FWHM of emission(Figure 3.12b). Antimony incorporation can be achieved in two ways. Firstly, by subjecting the InAs dashes to Sb flux once formed. Whilst this did extend the emission wavelength, it also greatly reduced the emission intensity. Alternatively, it can be achieved by direct growth of InAsSb, this resulted in better intensity and further extension of wavelength. Structurally it also resulted in a more uniform, flatter dashes with greater length as can be seen in

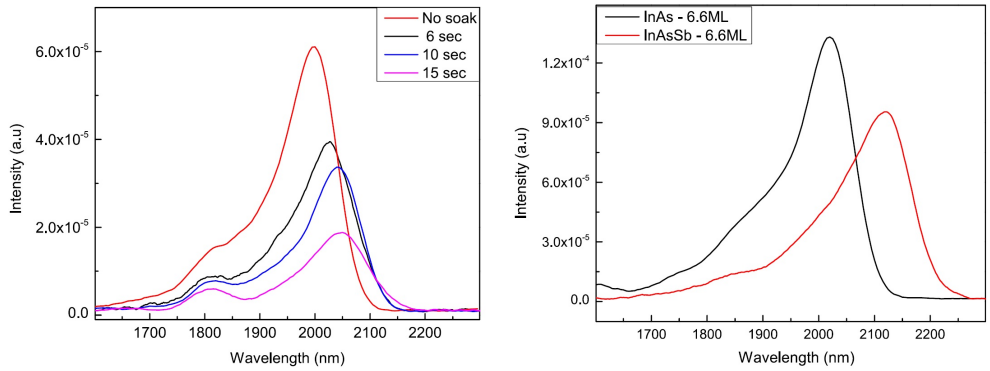

(a) (b)

Figure 3.12: (a) PL Spectra of InAsSb QDashes produced by soaking InAs dashes in antimony flux prior to capping. (b) InAsSb QDashes produced by InAsSb deposition[98].

Figure 3.11, a result also seen by K. Keawaguchi *et al.*[104]. This morphology change is attributed to the surfactant properties associated with antimony[100, 101]. The ground state energy suggests that antimony incorporation was between 2 and 4%. The antimony incorporation was controlled by decreasing the growth temperature, this increases the time antimony remains on the surface thus increasing the incorporation and extending the wavelength. By reducing the growth temperature emission wavelength was extended as far as 2.25 μm as shown in Figure 3.12. The introduction of antimony is a preferred method of extending the wavelength, the increased InAs deposition required to produce the same red shift as the introduction of 2% antimony produces an order of magnitude less intense PL emission.

Similar experiments by the LENS-UMR FOTON group at INSA de Rennes also showed the validity of extending the wavelength of InAs nanostructures with antimony, where direct deposition of InAsSb is superior to a antimony soak prior to capping[105]. Theoretical calculations indicate that whilst remaining a type-I transition the use of $InAs_{(1-x)}Sb_x$ should provide emission at wavelengths up to 3.5 μm, though IVBA (Section 2.7.4) will become resonant, requiring the introduction of phosphor to the barriers [106].

As part of the EU funded PROPHET network[107], K. Papatryfonos profiled the DOS of quantum dashes and determined them to be one dimensional in nature[108]. With the aim of apply quantum dash derived devices to gas sensing applications, ridge lasers operating at 2.07 μm with a pulsed output power of 11 mW were developed[109].

In Chapter 6, light emitting diodes will be produced from quantum dash material provided by the Laboratory in Photonics and Nanostructures, CNRS, France.

3.7 Metamorphic Epitaxy

The first LEDs were homoepitaxial materials doped to form pn junctions but emission was limited by the intrinsic band gap of the material. Heteroepitaxial devices followed, these were layers of alloyed materials with lattice constants within a narrow range of the lattice constant of the substrate used. This allowed for the emission wavelength, confinement offsets, carrier mobility and other characteristics to be tailored to requirements within the confines of approximate lattice matching.

The next logical step is the growth of highly lattice mismatched materials beyond their critical thickness. Doing so causes them to relax, when this is done intentionally to grow on the resultant relaxed material, it is known as metamorphic epitaxy[110].

Once no longer constrained by the limits of lattice matched growth of epilayers with the substrate the degrees of freedom in device design vastly increases opening new solutions to technological challenges. This can be beneficial in many systems, for example the growth of GaSb on GaAs substrates. Such a system allows the more mature contact development of GaAs to be used. It also becomes possible to design devices requiring semi-insulating substrates, useful in several device designs. However, as to date it has not been possible to produce semi-insulating GaSb. GaAs substrates also offer superior heat sinking ability, improving the efficiency of the device under higher loads. Larger substrates are available for GaAs which along with the reduced cost of the substrate

improves the commercialisation prospects of devices.

The disadvantage of metamorphic growth is that the lattice mismatch is accommodated via misfit dislocations. Early studies noted that these misfits were likely to generate threading dislocations, which are problematic as they do not terminate within the crystal unless they loop[111]. Thus they can only be removed by reaching the surface, because they typically travel in the growth direction they are unlikely to terminate in the material and therefore the effect is cumulative. Once produced unless deliberately engineered out they will effect all subsequent layers. The threading dislocation density (TDD) is a key figure of merit in metamorphic epitaxy as threading dislocations act as non-radiative centres reducing the devices efficiency and mean time to failure[110].

There have been three methods adopted to reduce the TDD; abrupt interfaces, buffer layers and structured interfaces. In the GaAs/GaSb system the most successful process has been that of an atomically abrupt interface where the XRD rocking curve FWHM of the deposited GaSb is 22" compared to that of the GaAs substrate at 15" indicating high quality material[112]. It was noted early on in the study of this system that at the interface the misfit was relieved by a periodic array of 90° dislocations [113, 114]. These dislocations form during the island growth stage of deposition, when the islands start to coalesce these periodic dislocations will meet at the interface. When coalescence occurs, if the dislocations are shifted by a half period then 60° dislocations can form. These are less desirable as twice as many are required to relieve the equivalent amount of strain as 90° dislocations[115]. They can also cause the bending of the GaSb layer, or the GaSb epitaxial layer can become tilted off the growth axis as shown in Figure 3.13b.

D.L. Huffaker *et al.*[35, 116, 117, 118, 119] have reported that by optimising the growth conditions it is possible to ensure that the interface dislocations are entirely of the 90° species (Figure 3.13a). Resulting in dislocation densities of $<10^5\,\mathrm{cm}^{-2}$ within 100 nm of the interface, only 100 times greater than those seen in GaSb substrates [120]. There is disagreement on which method of growth of the GaAs/GaSb interface is superior.

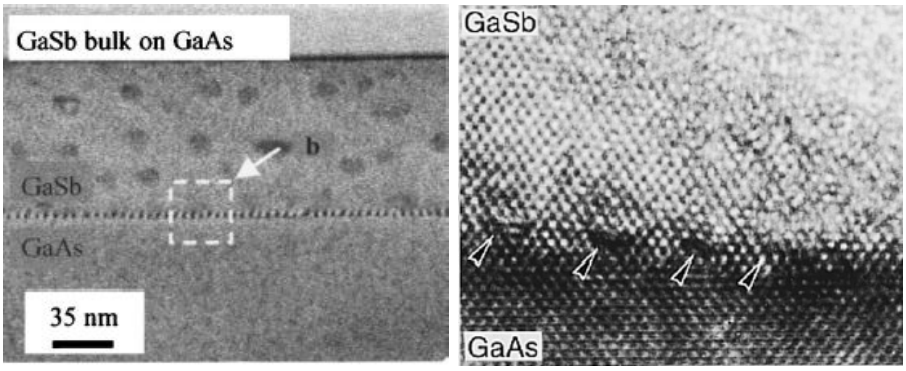

(a) (b)

Figure 3.13: (a) TEM image of optimised IMF interface showing periodic misfits[35]. (b) TEM image showing the results of 60° dislocations, note the tilt of the GaSb layer relative to the GaAs[115].

Richardson *et al.* suggests that following a period of GaAs growth the arsenic valve should be closed allowing the arsenic on the surface to disorb. Once the RHEED indicates that the surface is no longer arsenic rich, gallium and antimony should be deposited simultaneously at a Sb:Ga ratio of 1.75 and a growth rate of 1 μm/h[112, 121]. Huffaker *et al.* use a similar system, growing the GaSb slower and at a higher temperature (560 ℃ compared to the 505 ℃ of Richardson). The key difference though is a use of an antimony 'soak' (subjecting the gallium rich surface to an antimony flux) by Huffaker[117]. This occurs after the surface becomes gallium rich, proceeded by the growth of GaSb, it is not evident from the literature which is most effective.

Electrically, the dangling bonds of the Ga at the interface produces a large discontinuity of 0.7 V though this can be overcome by introducing a n-type δ-doping in the region within the interface[119]. This supplies an excess of carriers in this region to counteract the dangling bonds. Reverse breakdown currents are also higher than in comparable devices grown on GaSb suggesting the greater presence of threading dislocations indicating that the interface is never entirely defect free.

Chapter 4

Experimental Details

4.1 Introduction

This chapter will outline the techniques used to produce and characterise LEDs and the semiconductor materials they are produced from. Specifically their growth using molecular beam epitaxy and the processes involved in cleanroom processing into LEDs. Characterisation tools will include x-ray diffraction, photoluminescence and electroluminescence.

4.2 Molecular Beam Epitaxy (MBE)

The use of molecular beam epitaxy produces high quality single crystal semiconductor materials from a range of solid and gas sources. This mode of growth is slow compared to the other growth techniques such as liquid phase epitaxy. With growth rates which are typically a few Å per second, this allows for precise control of layer thickness and abrupt interfaces, both necessary attributes when growing quantum structures such as wells and dots. High quality crystal structures ideally need to be impurity free. To reduce impurities and reduce scattering within the growth chamber it is kept at ultra high vacuum of the order 10^{-10} mbar.

MBE Machine

The MBE system used in the growth of samples for this research is a VG-V80H MBE system composed of two chambers, one for growth and another for preparation of the substrates. The latter includes load locks for loading and storage of wafers and a heater for outgassing, to remove hydrocarbon and water vapour deposits.

The growth chamber is pumped using a combination of a cyropump cooled to 10 K, ion pump and a titanium sublimation pump. The pressure is measured using a tungsten filament ion gauge. Further pumping is supplied by cryopanels inside the chamber, these also provide thermal shielding between effusion cells(see Fig 4.1).

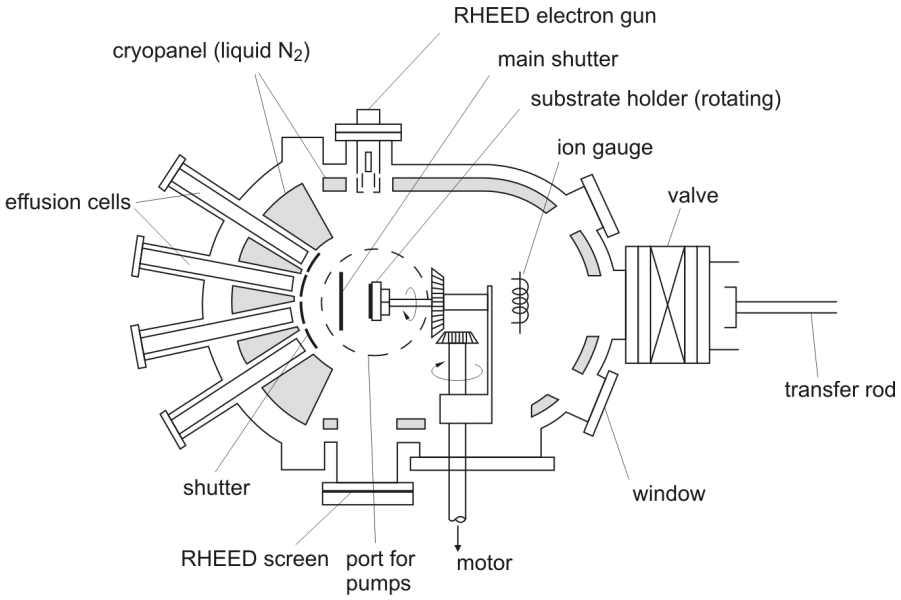

Figure 4.1: Schematic of MBE machine growth chamber, showing the location of the substrate holder, effusion cells and RHEED gun and screen[122].

Molybdenum holders are used to mount substrates in the growth chamber on the substrate manipulator. The samples are grown on 2 inch wafers and quarters of 2 inch wafers. The manipulator rotates the substrate during growth to reduce non-uniformity in the sample surface. There is also a heating element built into the manipulator behind the substrate which can be used to heat the substrate, this is calibrated using known transition points for the substrate material, such as the oxide desorption point. The oxide desorption process is the point at which the surface oxide on the substrate is fully removed. At this point the reflection high energy electron diffraction (RHEED) pattern changes (see below), because this transition occurs at a fixed known temperature it can be used to determine the real substrate temperature[123].

The sources available on the machine are aluminium, gallium, indium, antimony and arsenic. For doping, beryllium (p-type) and GaTe (n-type) are used. The group III elements and dopants use thermal effusion K-cells; aluminium and gallium use so called 'hot-lip' cells while the indium has 2 independently controlled filaments, the dopants use

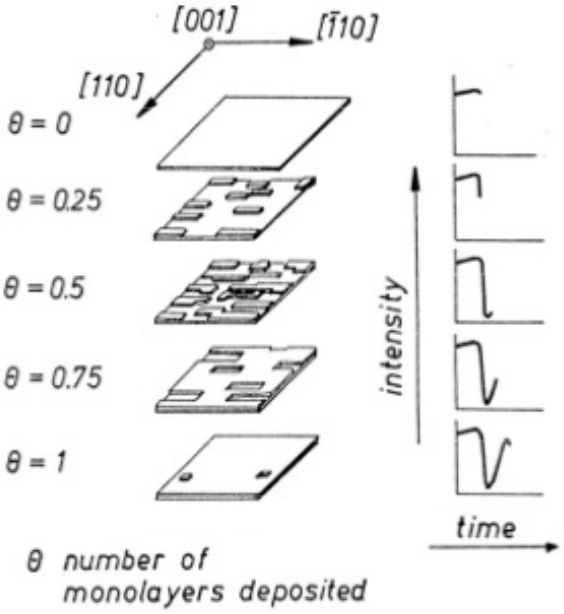

Figure 4.2: RHEED oscillations produced Frank-van der Merwe mode growth (layer-by-layer) used to determine growth rate [124].

single filament cells. The group V elements use cracker cells, the solid source material - for example arsenic - is heated in a crucible to form a flux beam, this is channelled into an independently heated cracking zone which allows either As_4 or As_2 beams dependent on the cracker temperature.

Growth rate is calibrated using the RHEED gun. This fires electrons at a glancing angle onto the substrate which are reflected onto a fluorescent screen. Operational parameters are a filament current of 1.4A with a beam voltage of 14kV.

The resultant electron beam is diffracted with the pattern dependent on the surface morphology and orientation. Surface smoothness results in a streaky image whilst 3D features result in a spotty image. This can be used to observe the growth mechanism of structures and provide indication of successful 2D or 3D growth as it occurs.

The intensity of a single spot on the RHEED pattern varies in intensity during the deposition of a monolayer, it is brightest when a smooth surface exists, as more material

is deposited the surface becomes less smooth as shown if Figure 4.2. This rough surface reduces the intensity of the reflected electron beam. Further deposition begins to smooth out the surface again, until a full monolayer of material is deposited and the intensity maximises again. This oscillation in intensity can be used to determine the growth rate of different materials at different cell temperatures.

4.3 Structural Characterisation

4.3.1 High Resolution X-Ray Diffraction

High Resolution X-Ray Diffraction (HRXRD) is a non-destructive method of determining the lattice constant of a crystal, because of this it can be used to determine the composition of epitaxial layers of semiconductors. From the scan it is possible to determine the thickness, strain and composition of a material as well is its homogeneity. HRXRD is based upon Bragg's Law for the scattering of X-rays by a crystal,

$$n\lambda = a_0 \sin(\theta) \tag{4.1}$$

where n is an integer, λ is the wavelength of the incident X-rays, a_0 is the lattice constant and θ is the angle between the lattice planes and the incident X-rays. From this equation it is possible to determine at which angles (θ) constructive interference occurs when a lattice spacing (a_0) and X-ray wavelength (λ) are known. A BEDE QC200 machine was used in this work with fitting utilising RADS Mercury software (Jordan Valley).

The X-ray source is a filament that produces electrons which are accelerated by a 35 kV potential towards a copper target, this produces X-rays with a wavelength of 1.54 Å from the K_α transition. The X-rays then pass a collimator before being conditioned on a reference crystal angled such that the reflected beam satisfies the Bragg condition. This produces a beam of highly monochromatic X-rays. A schematic of the system is shown in Figure 4.3. The sample is placed on a table that can rock through ω and the scan is

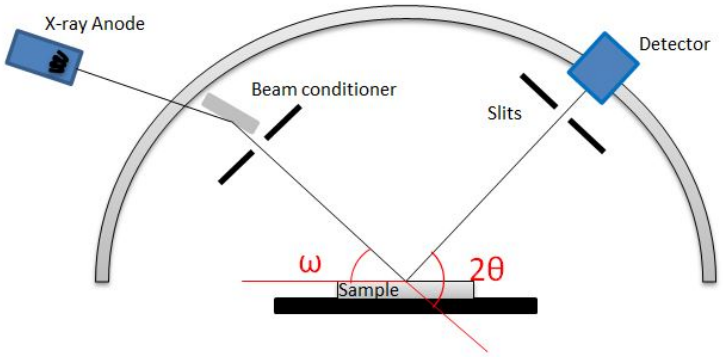

Figure 4.3: Schematic of the BEDE x-ray diffraction machine showing ω - the angle between the X-ray source and the sample and 2θ - the angle between the incident beam and detector angle.

taken by a detector which moves through 2θ. Most often these scans are taken about the (004) Bragg reflection as this provides insight into the lattice constant in the growth direction.

High intensity peaks with very small Full Width Half Maxima (FWHM) are indicative of high crystal quality as seen in homo-epitaxial growth (Figure 4.4). The position of peaks relative to the substrate can be used to determine their composition ((a) in the figure). Thickness can be determined by fitting of the data using simulation software. When the sample contains multi quantum wells (MQWs) the separation of the satellite peaks (b) indicates the period of the well and barrier combined[125]:

$$t_w + t_b = \frac{(n_1 - n_2)\,\lambda}{2\,(\sin\omega_1 - \sin\omega_2)} \tag{4.2}$$

where t_w and t_b are the thickness of the well and barrier respectively, n_1 and n_2 are the peak numbers with respective angles of ω_1 and ω_2 ((b) in Figure 4.4).

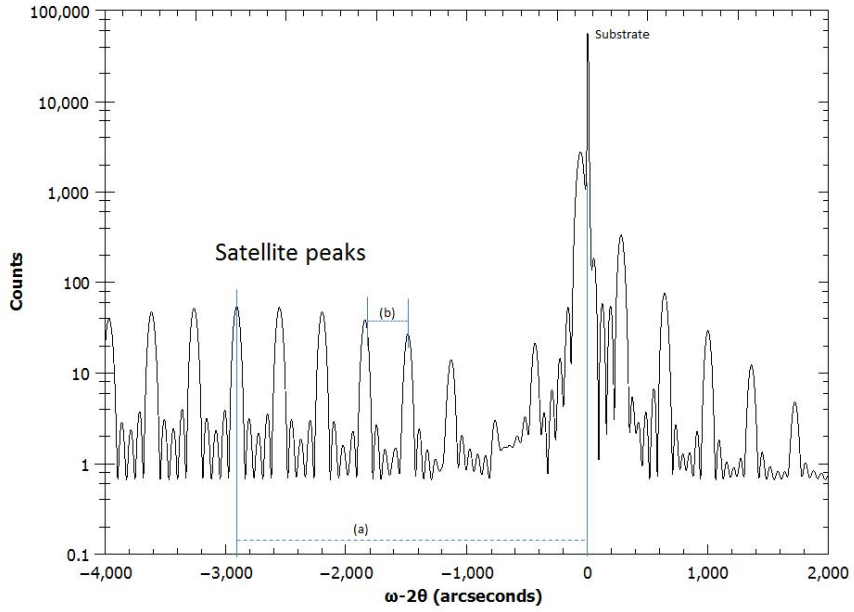

Figure 4.4: Example rocking curve of five 6 nm $In_{0.3}Ga_{0.7}Sb$ quantum wells grown on GaSb with 30 nm GaSb barriers. Well composition is determined by the spacing denoted as (a) and periodicity of the Quantum wells as denoted by (b).

4.4 Device Fabrication

The majority of the samples presented in this work were processed in the class 1000 and 100 cleanrooms at the Quantum Technology Centre of Lancaster University Physics Department. Additional processing was undertaken at the EPSRC National III-V Centre in Sheffield, namely that of the Quantum Dash LEDs. The following section will outline the method used to fabricate the LEDs tested in this study, using the GaInSb quantum well LEDs as an example. Proceeding sections will provide details for additional samples where they deviate from this method. For example in the change of etching solution needed for different materials.

4.4.1 GaInSb Quantum Well LEDs

To prepare the Quantum well samples for processing they are cleaned by boiling in n-butyl acetate for 2 minutes then rinsing in acetone and isopropyl alcohol (IPA) before being dried using compressed nitrogen gas. This removes any organics and water vapour present. The back contact is first applied using a Moorfield Minilab thermal evaporator

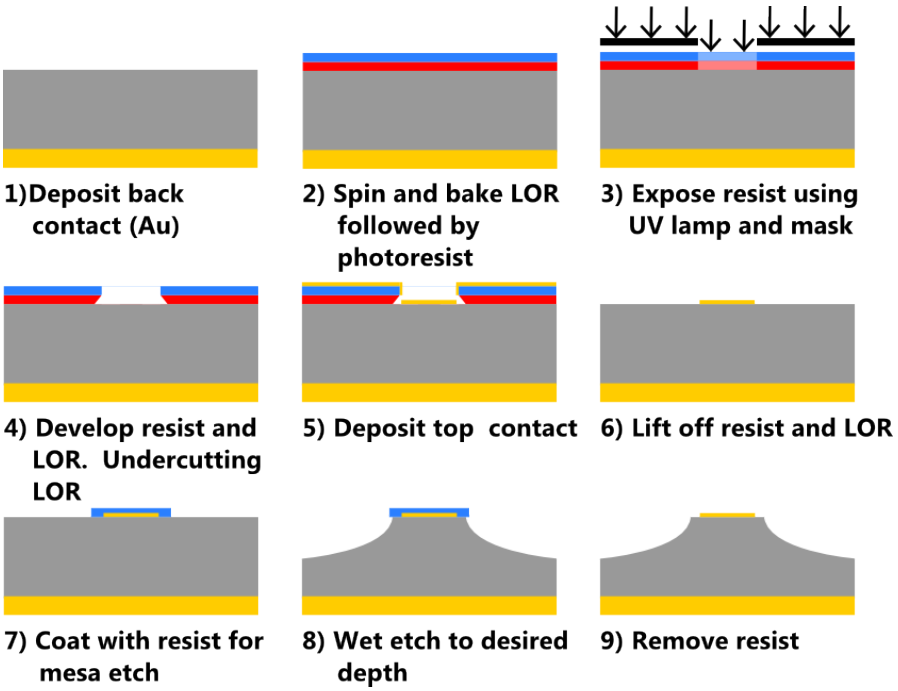

Figure 4.5: Step by step LED fabrication. The semiconductor is grey, the red and blue are LOR and photoresist respectively with the lighter shades denoting exposed sections. The orange represents the gold contacts.

for the deposition of metal films. Samples are fixed to an aluminium mounting plate using Kapton tape. This plate is then inserted into its holder at the top of the evaporator such that the sample surface is facing the crucibles. The metals to be evaporated are cleaned using acetone and IPA then baked at 200 ℃ to remove any organics and water vapour. They are then placed into a ceramic coated tungsten or pure tungsten crucible. The system is then pumped down to 10^{-6} mbar to prevent oxidation and increase the mean free path of the metal atoms beyond the dimensions of the system. For GaSb,

Ti-Au contacts are used. The titanium crucible is heated until a pressure drop is noted in the chamber, this indicates that the titanium has evaporated and begin condensing on the surfaces of the chamber. A shutter is then moved to expose the sample to the metal. Deposition thickness is measured with a quartz crystal thickness monitor (typically for Ti this rate was 2 Å/s). The process is then repeated for the Au. The crucible is heated to a known drive current beyond which point it is known the metal is evaporating. At this point the shutter is opened until the desired thickness is achieved. The sample is then allowed to cool before being brought back to atmospheric pressure and removed from the evaporator, as seen in Figure 4.5(1).

To produce the top contacts for the LEDs the sample is mounted on to the vacuum chuck of the spinner (SÜSS Microtech Labspin) and fully covered in Microchem LOR-3B ensuring the entire sample is coated using an eye dropper. The sample is then spun at a rate which gives the LOR a thickness greater than the thickness of the metal to be deposited, typically this was 4000 rpm for 30 s which provided a thickness of 300 nm of LOR. To harden the resist the sample is baked at 170 °C for 3 minutes. A further coat of Microposit S1805 photoresist is applied to the sample and spun at 4000 rpm for 30 s to achieve a even layer 500nm thick. The photoresist is then baked at 110 °C for 2 minutes to harden using a hotplate (Figure 4.5(2)).

The chosen contact or mesa pattern is applied using a SÜSS Microtech MJB4 mask aligner with a 365 nm UV lamp with power supply control achieving constant light intensity. For surface emitting LEDs the mask pattern has circular mesas of different diameters (see Figure 4.6a) is used. For edge emitting LEDS (ELEDs) the mask has strips with widths of 25 μm and 50 μm capped with a gold strip 25 μm wide, these are shown in Figure 4.6b. Once the mask is aligned with the substrate the resist is exposed to UV light for 2.5 s (3) and then developed using Microposit MF-CD-26 developer for 30 s (4). The sample is then rinsed in deionised water and blown dry using nitrogen gas. The sample is then viewed under a microscope to ensure all photoresist is removed from

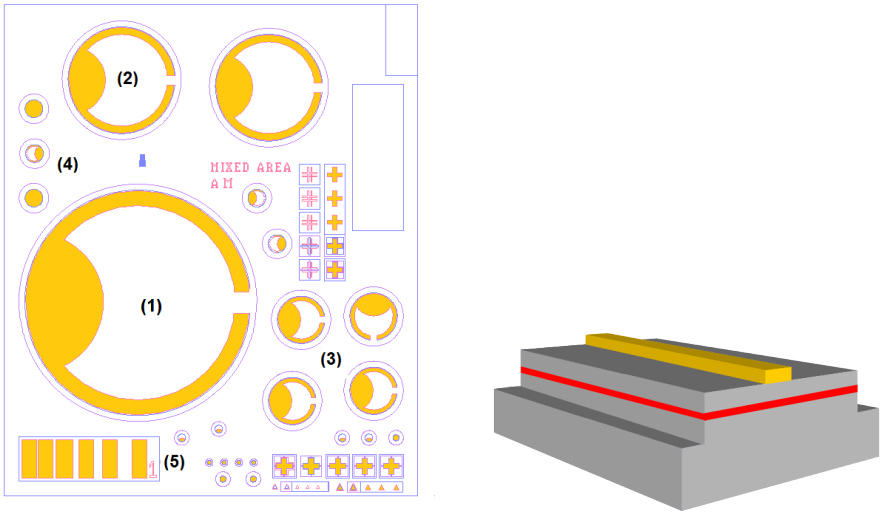

(a) (b)

Figure 4.6: (a) Schematic of device test set of surface emitting LEDs. The mesa diameters are (1) 800 μm, (2) 400 μm, (3) 200 μm and (4) 100 μm. Note the developer check marks above the largest mesa and the transmission line model pads at the bottom (5). (b) A graphic representation of an ELED, gold represents the top stripe contact and red the active region.

the desired areas and the edges are well defined. This is helped by the use of developer check features included in the mask (see Figure 4.6a between (1) and (2)). The LOR is removed at a faster rate by the developer creating an undercut, this provides a break in the metal coating facilitating the lift off process. Metals are then deposited using the thermal evaporator as described previously (5). Once deposition is complete the sample is placed into a beaker of MicroChem PG Remover for approximately 1 hour until all excess metal has lifted off. Then sample is then rinsed in IPA and dried (6).

The next stage is to etch the mesas producing individual devices. Prior to etching the samples are coated in a layer of S1805 photoresist and patterned and developed as outlined above(7). Mesas are etched using a mixture of hydrochloric acid, hydrogen peroxide and deionised water at a ratio of 1:1:5 (8)[126]. Initially the etch rate is approximately 1 μm/min and the etch depth is measured using a KLA Tencor Alpha-Step IQ surface profiler. After etching the samples are rinsed in deionised water to stop further

etching. The remaining photoresist was removed using acetone and cleaned with IPA(9).

For testing the sample wafer is scribed into individual chips using a Karl SÜSS RA-120M scriber and these chips are mounted onto TO-39 headers using solder. A TPT HB05 wire bonder is used to bond the top contact to the header pin. The header is placed in the chuck and heated to 100 ℃. Suitable values for the force, time and ultrasonic power are selected, a ball bond is produced on the contact pad on the device and a second bond connected to the header pin.

4.4.2 InP Quantum Dash LEDs

Using the mesa mask shown in Figure 4.6a and methods outlined previously, SPR350 photoresist was exposed and developed. The sample was etched to a depth of 2.5 μm using a mixture of 47% hydrobromic acid, 100% acetic acid and potassium dichromate solution at a ratio of 1:1:1. The potassium dichromate solution (KCr_2O_7) was produced by dissolving 14.7 g of crystalline KCr_2O_7 in 100 ml of H_2O. The top contact was laid down using a plasma sputterer and consisted of 50 nm of titanium, 120 nm of platinum and 200 nm of gold; this was annealed at 420 ℃ for one minute using a rapid thermal annealer. The back contact was produced by thermal evaporation on 20 nm of indium-germanium at a ratio of 1:1 by weight and then 200 nm of gold; this was rapid thermal annealed at 360 ℃ for 30 seconds.

4.4.3 InSb SML Quantum Dot LEDs

The InSb SML quantum dot samples were processed into edge-emitting LEDs (ELED). This consisted of ridges 25 μm wide and 600 nm high. The ridge length was approximately 1500 μm. The top p-type contact consisted of 20 nm of titanium and 200 nm of gold, which extended 150 μm to each size of the ridge. The bottom n-type contact was achieved with 20 nm of 1:1 indium-germanium by weight and 200 nm of gold, which was rapid thermal annealed at 400 ℃. Both contacts were deposited using thermal evapora-

tion.

One sample was processed into surface emitting LEDs using the mask shown in Figure 4.6a. The mesas were etched to a depth of 3 μm using a solution of phosphoric acid (H_3PO_4), citric acid, hydrogen peroxide and water at a 1:10:5:40 ratio. This etch resulted in a high quality mirror finish, superior to that seen with the HCl etch, there was however some trenching. Given the top-bottom nature of the contacts used and the thickness of the AlGaSb layer that the etch stopped in, this trenching was considered inconsequential. It should however be taken into account if top-top contacts are used in future.

4.5 Optical Characterisation

4.5.1 Photoluminescence

Photoluminescence (PL) is a non-destructive method to probe the energy structure of a semiconductor. A laser provides a source of photo-excited carriers in the sample which decay to the band edge before recombining. If the recombination is radiative the resultant photons can be collected and the spectra analysed to determine the energy transitions and band structure of the material. A schematic of the system is shown in Figure 4.7.

In this work laser excitation was provided by a 514 nm argon ion laser (Spectra Physics Stabilite 2017) with an output power which can be varied between 0.1 W and 1.4 W. Given the optical set-up used in the system this results in a irradience of 10 W/cm^2 at the sample surface at 1 W laser power. The laser is chopped at $\sim$220 Hz to remove interference from the mains etc. The light from the sample is collected and focussed into a monochromator using CaF_2 lenses.

The monochromator (Bentham M300) has a 300 lines/mm grating this provides a spectral resolution of 10 nm/mm slit-width (Slits can be adjusted to 0.05 mm accuracy).

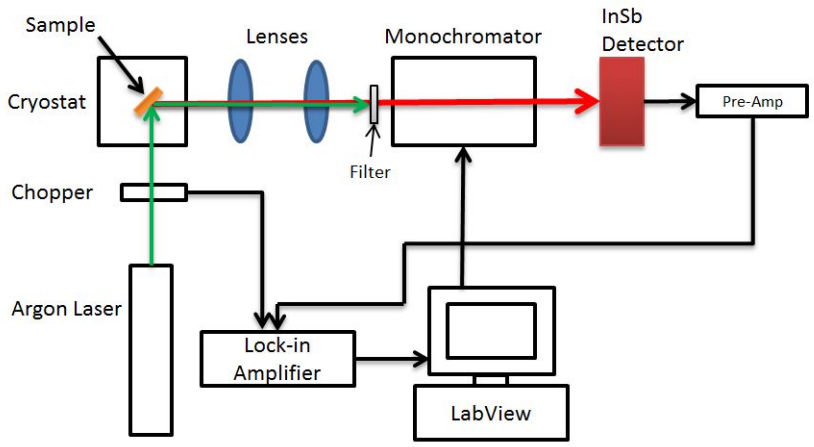

Figure 4.7: Schematic of photoluminesence system, the red line indicates the emission from the sample, green the laser beam line.

To remove higher orders diffraction modes created by reflected laser light being included in the spectra, a Si filter is inserted at the entrance aperture in this work the cut off wavelength of the filter was 1.04 μm (Bentham OS1250). A liquid nitrogen cooled InSb detector (Judson Technologies) is placed at the aperture of the monochromator on an xyz stage.

The signal from the detector first goes through a pre-amplifier before being picked up by the lock-in amplifier (Standford Research Systems SR810) which references the chopper frequency. The signal produced by the lock-in amplifier is then transferred to a PC utilising Labview from National Instruments, This program also controls the stepper motor in the monochromator.

The cryostat (Oxford Instruments) uses continuous flow liquid helium which allows it to operate from 4 K to 300 K. The sample is mounted on a copper plate using silver Electrodag to provide a thermal connection, this copper plate is then screwed to a cold finger which is placed into the sample chamber of the cryostat. The chamber is then evacuated and filled with helium gas to provide a heat exchange. A temperature controller is used to control a heater in the helium gas flow, the stability of the tem-

perature at the sample is monitored using a silicon diode mounted next to the sample, the voltage of which is measured using a Keithly 2400 source meter calibrated at known temperatures. Spectra were taken with laser powers starting at 1.4 W and reducing in intensity until the signal was lost. The range of temperatures for this work were 4 K to 300 K or until signal was lost. To compare absolute intensity between samples a second calibration sample is included on the reverse of the cold finger and used to calibrate the system with each use.

4.5.2 Electroluminescence

To characterise LEDs and lasers a similar set up to photoluminesence can be used. A schematic of the system used in the work is shown in Figure 4.8. The electron-hole pairs are no longer produced by photoabsorption but direct injection across the junction using a pulse generator (Agilent B114A) at 1-5 kHz and a duty cycle of 0.1-50%. The pulse generator also produces a reference signal which is sent to the lock-in amplifier (Bentham PSD 496). Current to the device is measured with a induction loop connected to an oscilloscope. The device is mounted on a TO header which in turn is fitted to a copper cold head.

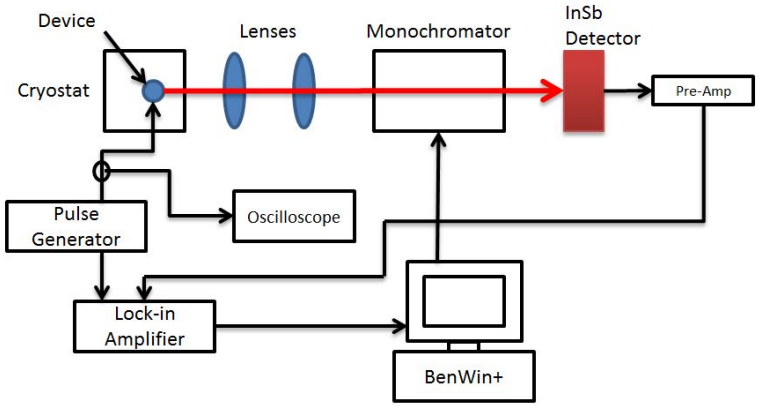

Figure 4.8: Schematic of electroluminesence system, the red line indicates the emission from the device.

The light produced is collected and focused using CaF_2 lenses into a monochromator (Bentham TM300) with a 300 lines/mm grating before the intensity is measured by a liquid nitrogen cooled InSb detector (EG & G Optoelectronics) This is relayed via a preamp to the lock-in amplifier, the processed signal is sent to a PC using BenWin+ software (Bentham) this software also controls the monochromator grating and slit width.

The cyrostat (Oxford Instruments OptistatDry) uses closed cycle refrigeration to achieve a temperature range of 4 K to 300 K. The device is clamped to a copper holder designed to present either the edge or top surface to the window depending to if the device is surface or edge emitting. Temperature is monitored using a four wire rhodium-iron resistance temperature sensor which is connected to a temperature controller (Mercury-iTC) which can control a heater to adjust the temperature.

4.6 Electronic Characterisation Techniques

4.6.1 Current-Voltage (I–V) Characteristics

A Keithly 2400LV SourceMeter controlled by a Labview program was used to measure the current-voltage (I-V) characteristics of the devices. The voltage is stepped in 20 mV increments and the corresponding current measured. There is a built in current limiter to protect the device from damage the value of this was chosen with the dimensions of the device taken into consideration. These scans were taken between 77 K and 300 K.

This technique can be used to determine if leakage current is caused by surface states or defects within the semiconductor. By measuring the shunt resistance as a function of mesa diameter if $R \propto \frac{1}{d}$ then surface recombination is dominant, if $R \propto \frac{1}{d^2}$ then defect states within the diode such as threading dislocations dominate.

4.6.2 Transmission Line Method (TLM)

The transmission line method (TLM) is a measurement used to determine the contact resistance (R_c) of the device as well as the sheet resistance (R_{sh}) of a semiconductor layer. To determine these values an additional feature is added to the device mask. It includes a series of 75μm wide contact pads spaced 5, 10, 20, 30 and 50 μm apart (d_n)(as shown in Figure 4.6a). The semiconductor around the contact pads is isolated from the rest of the sample by etching. The resistance across each pair of pads is then measured using the Keithly 2400 SourceMeter. The resistance of the probe to contact (R_{cct}) is taken into account by taking a measurement with both probes on the same pad. It is also assumed that the metal contact has a much lower resistance than the semiconductor. The total measured resistance can thus be expressed as [127].

$$R_{TL} = (2R_c + R_{cct}) + \frac{R_{sh}}{W}d \tag{4.3}$$

where W and d are the width of the pad and pad separation, respectively. Thus by plotting the total resistance against $\frac{d}{W}$ one can determine the contact resistance from the y intercept and the sheet resistance from the gradient.

Chapter 5

Growth and Characterisation of GaInSb/(Al)GaSb Multiple Quantum Wells

5.1 Introduction

GaSb/InGaSb quantum wells are an established material system for the emission of light in the 2 μm region. Due to the lack of semi-insulating (SI) GaSb substrates and the relatively high cost of substrates there have been limited applications in broad area LEDs. Since the work of Huffaker one possible solution is the incorporation of an Interfacial Misfit Array (IMF)[35]. This has allowed low defect density growth of GaSb on GaAs substrates, opening traditionally GaSb based systems to large area array designs such as detectors and making multiple element LEDs more cost effective[128, 129, 130, 131]. This chapter examines the structural and optical properties of GaInSb/GaSb samples, evaluates their suitability as 2 μm LEDs and discusses what effect of the addition of an IMF has.

5.2 Quantum Well Design and MBE Growth

Theoretical modelling was undertaken to determine the desired composition of well to achieve 2 μm emission. A MATLAB®based finite well Schrödinger solver was used to find the energies of the carriers within the wells and subsequently the emission wavelength. The effective masses, band gaps and alignments were calculated using a Excel spreadsheet containing the equations outlined in Section 2.4. The equations incorporated strain and band bowing parameters taken from the comprehensive work of I. Vurgaftman *et al.* [132] and material data from the Ioffe Institute [45].

Modelling suggested that quantum wells with an indium content of 35% would emit light in the target region around 2 μm without reaching the strain limit and with suitable carrier confinement. To validate this a series of samples were grown on n-GaAs(100) substrates, this was facilitated by the introduction of an IMF. The IMF was achieved by firstly removing the oxide layer from the substrate. 100 nm of GaAs was then grown at 1 Monolayer per second (ML/s) with a substrate temperature of 575 ℃. Gallium flux was

then interrupted and the sample was left in a excess of arsenic for 1 minute. The arsenic flux was then switched off for 15 s allowing arsenic atoms to desorb, leaving the growth terminated on gallium atoms. This process was confirmed through observation of the RHEED pattern as it shifted from an As-rich (2×4) to a Ga-rich (4×2). This pause without flux, allowed for an abrupt gallium terminated interface to be achieved without As-Sb intermixing. The antimony valve was then opened for 4 minutes as the substrate was cooled to 515 ℃. Once the substrate temperature had stabilised the gallium shutter was opened and the growth continued with 400 nm of GaSb to create a buffer layer. The quantum wells were grown onto this, with a composition of $Ga_{0.65}In_{0.35}Sb$ and well widths as outlined in Table 5.1.

The quantum wells were grown at a rate of 1 ML/s. The composition was confirmed by the deposition of a bulk layer on a separate test wafer which was analysed by XRD. A 50 nm barrier of GaSb was grown between each quantum well. So that the GaSb cell temperature remained constant throughout the growth, the barriers were deposited at a rate of 0.65 ML/s. The quantum wells were then capped with 10 nm of GaSb.

X-ray diffraction (HRXRD) scans were taken of each sample to confirm the structures grew to the intended design and to give an indication of the structural quality. Two examples are shown in Figure 5.1. All samples except QA339 showed pendellösung fringes. Though they are less well defined than those simulated, this is consistent with XRD of other reported IMF samples[130].

Sample	Well Thickness (nm)
QA276	6
QA277	4.8
QA280	3.6
QA333	4
QA338	8
QA339	12

Table 5.1: Well dimensions of $Ga_{0.65}In_{0.35}Sb$ quantum well samples grown using IMF interfaces.

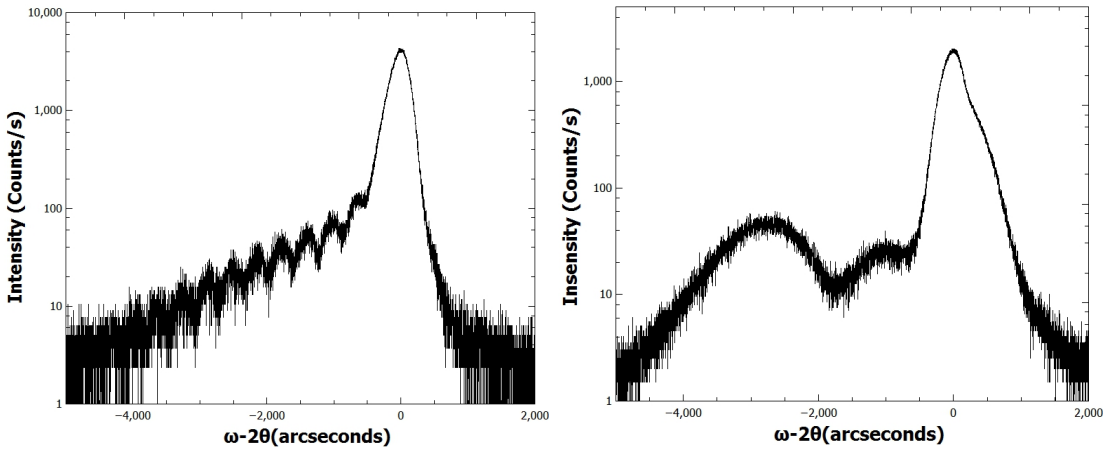

(a) (b)

Figure 5.1: (a) XRD of QA280 consisting of 5×3.6 nm $Ga_{0.65}In_{0.35}Sb$ QWs of pendellösung fringes consistent with a periodicity of 51 nm (b) XRD of QA339 consisting of 5×12 nm $Ga_{0.65}In_{0.35}Sb$ QWs evidence of relaxation with several additional features seen. The $\omega - 2\theta$ axis of both samples has been zeroed to GaSb.

The periodicity of each samples' quantum wells was calculated from the fringes using the equation[125];

$$t = \frac{(i-j)\,\lambda}{2\,(\sin\omega_i - \omega_j)} \tag{5.1}$$

where t is the thickness of a combined well and barrier layer, $(i-j)$ is the number of fringe peaks between peaks i and j and $\sin\omega$ is the angle of peaks. λ is the wavelength of the x-rays (0.1154 nm).

The resultant periods were consistently 2-3 nm smaller than the designed structures. The offset does not scale with well width, so is attributed to a thinner barrier of around 47 nm thick. It is not believed that this will compromise the results as it is still greater than the carrier wavefunctions penetration into the barriers. XRD simulations of QA339 (Figure 5.1b) indicate that the sample has relaxed as there are no clear fringes. Transmission electron microscopy (TEM) could have been used to determine if this is the case, but the weak photoluminescence of the sample led to it not being considered viable and further analysis excessive. The $\omega - 2\theta$ axis on each graph was zeroed to allow ease of

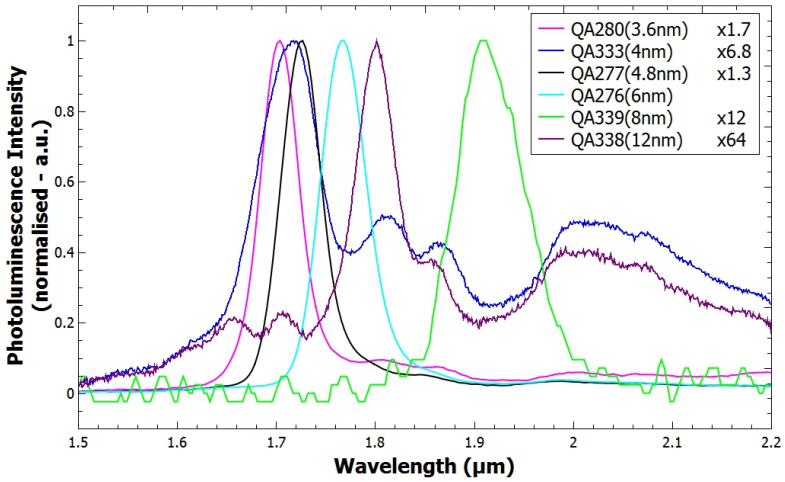

Figure 5.2: 4 K photoluminscence of $Ga_{0.65}In_{0.35}Sb$ QW samples grown on IMF, showing a clear red-shift with increasing well thickness. Additional peaks are due to contamination in the system and not inherent to the QWs.

comparison with future GaSb substrates samples. The full width half maxima (FWHM) of the GaSb peak can be used to indicate the crystalline quality of the samples. Larger FWHM indicate poorer quality. As the well width increased the FWHM also increased. Photoluminescence measurements were conducted with laser power densities of up to 10 W/cm^2 on the sample. At temperatures from 4 K until they quenched. The 4 K spectra have been normalised in Figure 5.2. Relative quality can be gained through FWHM of the spectra and the intensity of the signal. Additional peaks in Figure 5.2 for QA280, QA333 and QA338 have been attributed the contamination in the cryostat as they remained constant over several different samples, including the ones consisting of other material systems.

The 4 K photoluminescence emission peak wavelengths are shown in Figure 5.3a and are consistent with the MATLAB® simulations for all samples except QA339. This further suggests that it is beyond the critical thickness and no longer has abrupt wells. Comparing the quenching temperature of the samples in Figure 5.3b shows it increasing for well widths up to 6 nm at which point a decrease in quenching temperature is

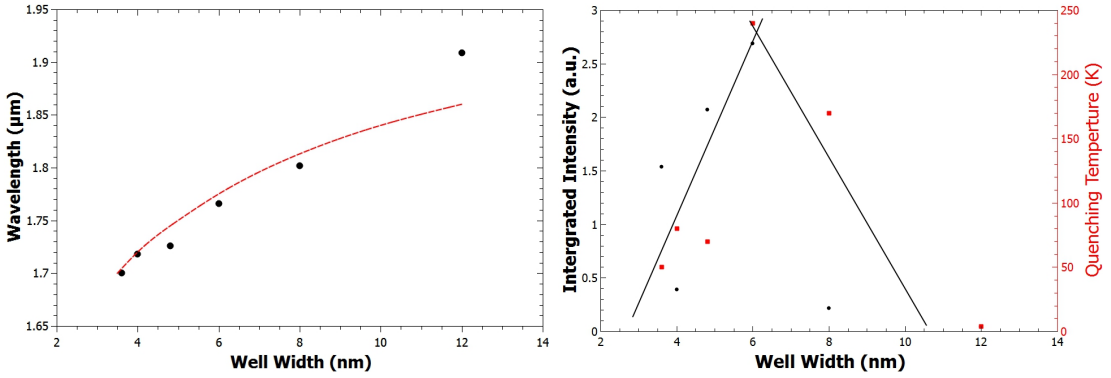

(a) (b)

Figure 5.3: (a) A comparison of the 4 K photoluminescence emission peak wavelength with the modelled values. The dashed line indicates the nextnano® simulated peak emission of $Ga_{0.65}In_{0.35}Sb$ wells at 4 K. (b) Figures of merit for the PL spectra of $Ga_{0.65}In_{0.35}Sb$ QW samples with integrated intensity of emission in black and temperature of PL quenching in red.

observed. Below 6 nm the reduced quenching temperature is attributed to decreasing confinement, the energy levels are higher in the wells due to the effect of the barrier potential. Above 6 nm the increased defects reduce the radiative efficiency and subsequently the quenching temperature. The superiority of the 6 nm sample is also replicated in the integrated intensity. The full width half maxima (FWHM, ΔE) of the 4 K PL scan can be used to further compare the inhomogeneity using the equation[133].

$$\Delta E = \frac{\hbar^2}{m_e^*} \frac{\Delta L_Z}{L_Z^3} \tag{5.2}$$

where m_e^* is the effective mass of the electron in the well, ΔL_Z is the quantum well interface roughness and L_Z is the quantum well width.

The interface roughness increases with well width (Table 5.2), indicating that the strain is affecting the interfaces. Further properties of the 6 nm sample QA276, including the activation energy and recombination processes were also examined. These will be discussed in the next section.

Sample	Well Thickness (nm)	ΔL_Z (ML)
QA276	6	1
QA277	4.8	1
QA280	3.6	0.5
QA333	4	3
QA338	8	7
QA339	12	30

Table 5.2: Composition of $Ga_{0.65}In_{0.35}Sb$ QW samples grown on IMF and ΔL_Z calculated from the broadening of the 4 K photoluminescence spectra

5.3 InGaSb Quantum Wells Grown on GaSb and GaAs with Different Barrier Materials

Once the 6 nm $Ga_{0.65}In_{0.35}Sb$ quantum wells in QA276 were identified as the well composition best suited to give an emission at the target wavelength, the structure was grown on GaSb and the composition of the barriers were varied to determine the optimal design. From the activation energy of the thermal quenching of the InGaSb/GaSb samples along with reviews of similar structures in the literature, carrier confinement was identified as a limiting factor in room temperature operation[66, 134]. To improve efficiency it is common to include AlGaSb blocking layers to confine the carriers to the active region[135, 136]. Due to lattice mismatch, these barriers have had to be thin, typically a few nm's. This means they are used to confine the entire active region, not individual quantum wells. Placed such that electrons cannot continue beyond the active region, they increase the recombination rate. Carriers can still recombine between the quantum wells as the barriers here remain the lower bandgap GaSb and thermal excitement of carriers to these layers is still possible.

To improve carrier confinement, barriers composed of AlGaSb were used in a third sample. This sample was grown with a novel ternary AlGaSb IMF to reduce the lattice mismatch. The AlGaSb IMF followed the same growth technique as the standard GaSb IMF, but with the opening of both the gallium and aluminium shutters, with cell

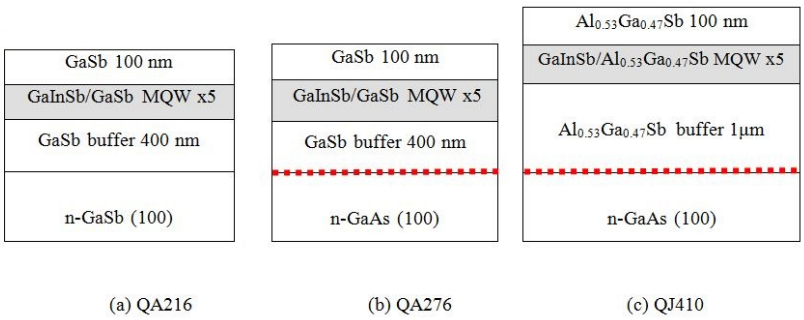

Figure 5.4: A schematic diagram showing the different structures studied in this section. (a) QA216: InGaSb/GaSb MQW grown homoepitaxially on GaSb substrate; (b) QA276: The same MQW structure as in (a) but grown on GaAs using the GaSb IMF buffer layer; (c) QJ410: a ternary $Al_{0.53}Ga_{0.47}Sb$ layer is used instead of GaSb for the IMF and also in the MQW barriers for additional confinement. (The IMF is represented with a red dashed line).

temperatures allowing for the growth of $Al_{0.53}Ga_{0.47}Sb$ at a rate of 0.46 ML/s with a substrate temperature of 515 ℃. A 1 μm buffer of AlGaSb was grown followed by five InGaSb quantum wells nominally the same as those previously described.

Another source of reduced optical efficiency was the choice of an IMF to make use of more cost effective and easily processed GaAs substrates. To benchmark the samples and quantify the effect of using IMF, a sample of five 6 nm $In_{0.35}Ga_{0.65}Sb$/GaSb quantum wells were grown on n-type GaSb. After the native oxide layer had been desorbed, the substrate was set to a temperature of 510 ℃. A 200 nm buffer layer of GaSb was deposited, followed by the quantum wells interspaced with 50 nm GaSb barriers and capped with 50 nm of GaSb. Growth rates were 0.65 ML/s for the GaSb and 1 ML/s for the InGaSb. A schematic of the three structures is included in Figure 5.4.

5.3.1 X-ray Diffraction

Initial analysis of the crystalline quality was completed using X-ray analysis; $\omega - 2\theta$ scans were taken of all samples. As expected, the homo-epitaxial GaSb sample (QA216) had the best FWHM at 27 arcseconds, indicating high crystalline quality. The pen-

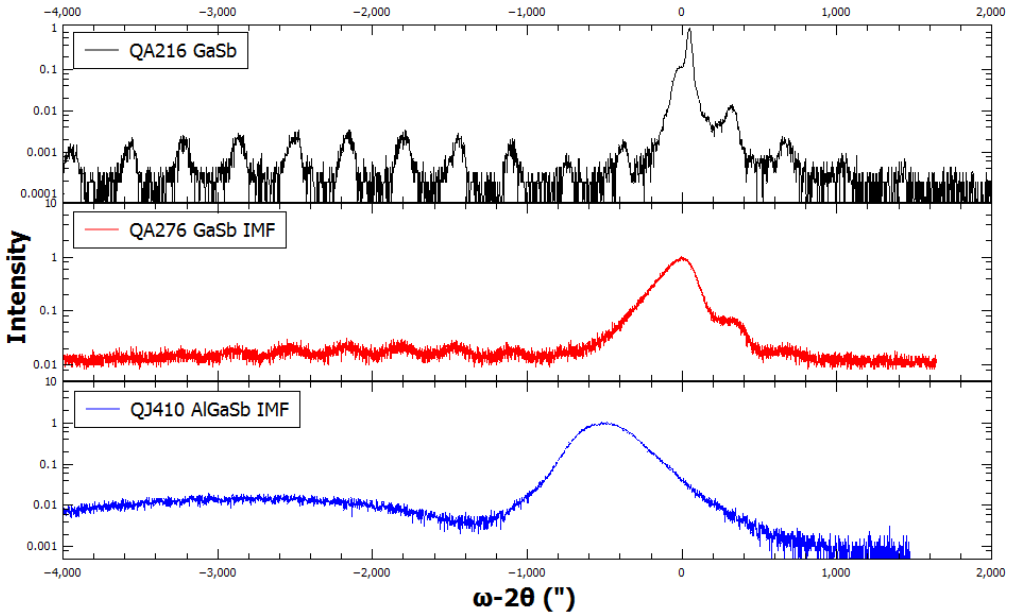

Figure 5.5: XRD of InGaSb QW samples with $\omega - 2\theta$ axis zeroed on lattice constant of GaSb. The lack of defined pendellösung fringes in the IMF samples is indicative of poor crystal quality as is the broadness of the buffer layer peak.

dellösung fringes were also clearly defined with a FWHM of 78 arcseconds and a well defined periodicity (Figure 5.5). The GaSb IMF sample (QA276) displayed a much broader hetero-epitaxial substrate peak with a FWHM of ∼220 arcseconds and pendellösung fringes with FWHM of ∼200 arcseconds. In the AlGaSb sample (QJ410) the pendellösung fringes have been lost in a shoulder peak similar to that of a bulk material with poor homogeneity. An alternative reason for this could be that the sample had non periodic wells. Fittings of the GaSb samples indicate that the quantum wells were (6±1) nm wide with indium concentrations of 34% and 35% for the GaSb substrate and IMF respectively. The difference between which was attributed to a change in growth rates between the samples. The AlGaSb peak in Figure 5.5 indicates a composition of $Al_{0.53}Ga_{0.47}Sb$ for the buffer layer and barriers, the broadness of the buffer peak indicates a poor crystalline quality with a FWHM of 470 arcseconds. The well composition was taken as $Ga_{0.72}In_{0.28}Sb$ from the position of the centre of the peak.

5.3.2 Transmission Electron Microscopy

To help elucidate the composition of QJ410, TEM images were taken by Richard Beanland at the University of Warwick, to examine the AlGaSb/GaAs interface and quantum well interfaces.

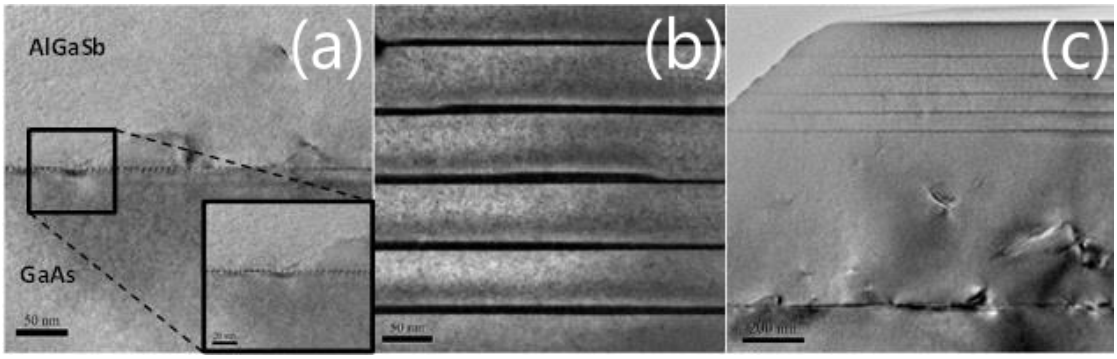

Figure 5.6: TEM image on AlGaSb-GaAs interface (a), with inset clearly showing ternary IMF. (b) shows abrupt thickness changes in the QWs varying from 7 nm to 12 nm. An overview of the sample (c) shows a overall high quality buffer layer with relatively few threading dislocations.

As shown in Figure 5.6(a) the possibility of a ternary IMF has been verified with a periodicity of 4 nm which represents 13 AlGaSb lattice spacings to 14 for GaAs. The growth of the IMF likey follow the same mechanism as the GaAs/GaSb IMF with the growth of GaAs still being Ga terminated. An antimony atom bonds to the Ga surface, the difference in lattice constant leaving a dangling bond every 14 gallium atoms and then the AlGaSb continuing growth on from this point. The quantum wells in this sample had an interface roughness of ± 3 nm, which is consistent with the broadness of the x-ray diffraction and 4 K photoluminescence spectra. Comparing this result with the values measured for the native and IMF GaSb samples of ± 1 nm, it can be inferred that the introduction of aluminium to the barriers has reduced the abruptness of the interface. The reduced interface abruptness could be caused by the difference in optimal growth temperatures of AlGaSb and GaInSb. The defect density after the misfit array was determined to be 2×10^9 cm^{-2}.

5.3.3 Photoluminesence

Photoluminesence measurements were taken for all three samples at temperatures from 4 K to 300 K with a laser power of 1 W/cm^2 to 10 W/cm^2 at the sample surface. A comparison of the 4 K PL is shown in Figure 5.7; the Gaussian line shape is indicative of excitonic transitions. The spectra of the two GaSb samples are in good agreement given the similar well design, the shift to lower peak wavelength being due to the reduced indium content in the IMF sample.

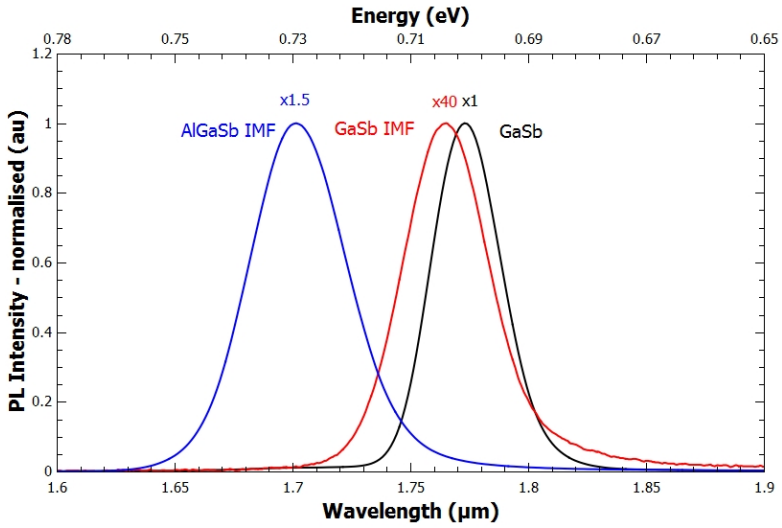

Figure 5.7: The normalised photoluminesence at 10 K from each of the MQW samples. The FWHM are measured as 15.4, 16.7 and 20.5 meV for GaSb, GaSb IMF and AlGaSb respectively.

Due to the increase defect density, the luminous intensity of the IMF sample is greatly reduced. The higher energies seen in the AlGaSb are a combination of the reduced indium content and the increased potential in both the conduction and valence band offsets, increasing the energies of the e_1 and hh_1 bands relative to the band edge. Also of note, is the increased lower energy tail in the IMF samples. This is attributed to the increased defect sites providing more acceptor and donor states via which recombination can occur.

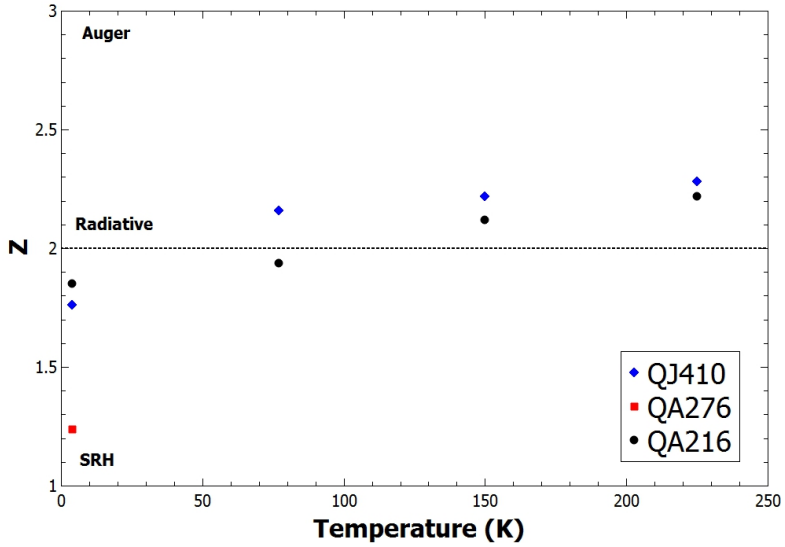

Figure 5.8: The temperature dependence of the Z value for each of the MQW samples; GaSb substrate – black points, GaSb IMF – red squares and AlGaSb – blue diamonds.

Using the FWHM of the 4 K scans and Equation 5.2, the well interface abruptness was calculated for all three samples. The GaSb and GaSb IMF samples both have abrupt interfaces calculated at 1 ML, whereas the AlGaSb has a broken interface of up to 10 MLs which is in agreement with the TEM images and XRD scans.

The samples were then warmed to 300 K with laser excitation power (L) varied at 10 K, 75 K, 150 K and 225 K to determine the dominant recombination process in each by comparing the photoluminescence intensity (I) with varied excitation power such that;

$$L \propto I^{\frac{Z}{2}} \tag{5.3}$$

where the exponent Z = 1 corresponds to Shockley-Read-Hall (SRH), Z = 2 corresponds to radiative recombination and Z = 3 corresponds to Auger recombination.

The results of this are shown in Figure 5.8. It is observed that recombination is dominantly radiative, except in the GaSb IMF sample where SRH is more significant. This is attributed to the expected higher defect densities in this sample, implying that

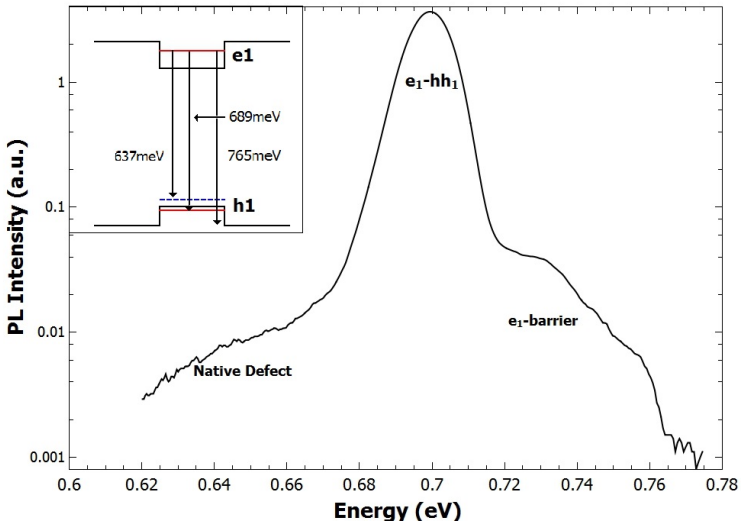

Figure 5.9: 4 K PL of homoepitaxial InGaSb/GaSb MQWs (QA216); Inset the schematic of the quantum wells

the AlGaSb IMF is of a higher quality. Further Z number analysis on QA276 was prohibited by the weakness of the PL signal over a range of excitation energies. Due to the limitations of this method of analysis the differences in Z parameter in the GaSb and AlGaSb IMF are considered negligible due to the assumptions used.

As shown in Figure 5.9, there is good agreement between the photoluminescence spectra and the finite well Schrödinger solver. The e_1–barrier/lh_1 transition also visible in the native GaSb sample, but not in the GaSb IMF sample. Given that the number of carriers and the density of states should be approximately equal band filling into the barrier should be expected in both samples. This is further evidence of a large number of carrier being lost to defect related non-radiative centres.

The temperature dependence of the integrated PL emission intensity is shown in Figure 5.10. The initial higher intensity of the GaSb is attributed to the superior crystalline quality. The recombination is predominantly radiative and the thermal quenching is as a result of limited carrier (electron) confinement in the quantum wells. The GaSb IMF has the lowest 4 K PL intensity which is as expected from the increased dislocation

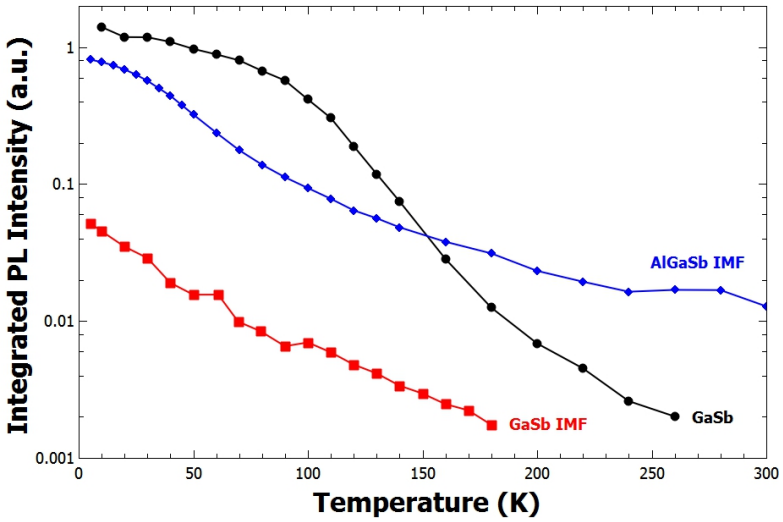

Figure 5.10: The temperature dependence of the integrated PL intensity for each of the MQW samples; GaSb substrate – black circles, GaSb IMF – red squares and AlGaSb – blue diamonds.

density originating from the heteroepitaxial growth mediated by the IMF interface. By comparison the 4 K PL of the AlGaSb IMF is an order of magnitude brighter and it maintains this improved signal over the entire temperature range. The increased confinement found in the AlGaSb sample helped to maintain photoluminescence emission up to room temperature, whereas the InGaSb/GaSb samples quenched at ~250 K. This is also supported by the nominally equal recombination processes seen in the AlGaSb IMF and the GaSb sample, but reduced emission seen in the GaSb sample with its smaller barriers. Both IMF samples are also more susceptible to non-radiative recombination due to the presence of increased threading dislocation densities and structural defects when compared to the homoepitaxial sample.

To determine the dominant quenching process in each sample, the integrated intensity of photoluminescence emission was plotted against $\frac{1}{kT}$ where k is Boltzman constant and T is temperature. The activation energy can be determined using the Arrhenius fitting function as shown in Figure 5.12[137];

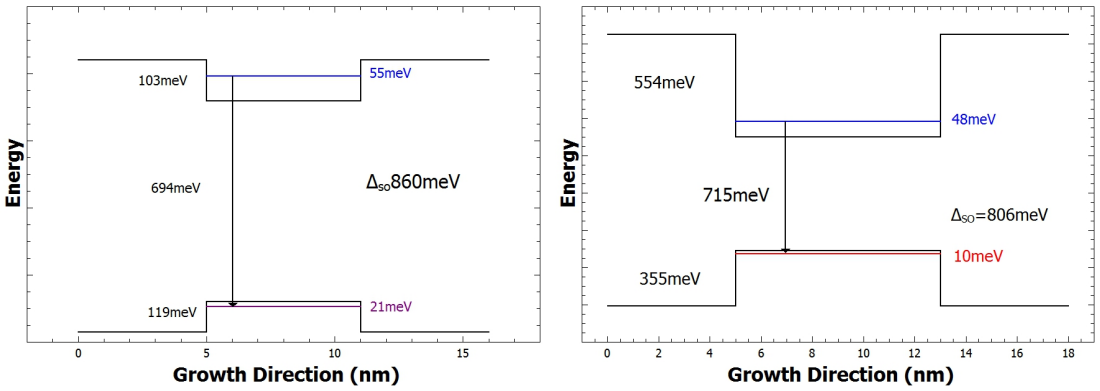

(a) (b)

Figure 5.11: (a) Band diagram for QA216 and QA276 showing valence and conduction bands along with the confined states. Δ_{SO} is also included. (b) Band diagram for QJ410 showing valence and conduction bands along with the confined states. Δ_{SO} is also included.

$$I = \frac{I_0}{1 + A\exp^{-E_a/k_BT} + B\exp^{-E_b/k_BT}} \tag{5.4}$$

where I is the intensity I_0 is the intensity at 0K and E_a and E_b are the activation energies. This gave an activation energy for QA216 of 60 meV, QA276 of 34 meV and QJ410 of 18 meV. In all 3 samples there is a second activation energy of around 4 meV. In QA216 this process is 1500 times weaker than the 60 meV process. In QA276 and QJ410 it is only 46 and 35 times weaker respectively, this would suggest this is a defect related process.

Using nextnano® the band diagrams of the quantum wells were simulated and can be seen in Figure 5.11. From this it was possible to assign the thermal quenching of QA216 to thermal excitation of electrons out of the well as confinement in the conduction band was 48 meV. As the Z value of QA216 was seen to increase with temperature it is also possible that an Auger process was responsible for quenching. With a Δ_{SO} of 860 meV for QA216, the CHSH process and inter valence band absorption (IVBA) can be discounted as $\Delta_{SO} > E_g$, so these processes are suppressed. Using the equations outlined in Section

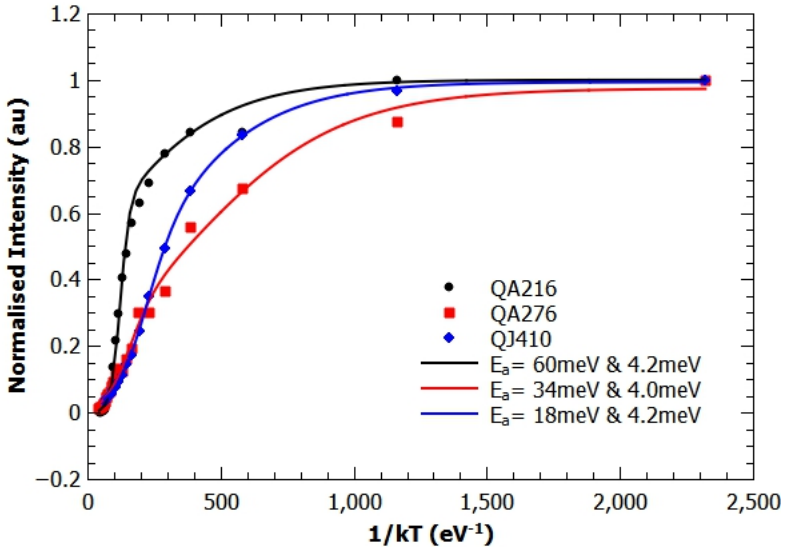

Figure 5.12: Arrhenius plot for QA216, QA276 and QJ410 plotting the normalised PL integrated intensity.

2.7.3, the activation energy of the CHCC process was found to be 49 meV. Literature of similar samples have identified thermal carrier leakage as responsible, this along with the reduced quenching in QJ410 suggests this is the case in QA216. The 18 meV activation energy for QJ410 is attributed to the CHHL process which has a calculated energy of 16 meV. Due to the large confinement of the carriers in QJ410 it isn't possible for it to be thermal excitation out of the wells as this would not be shown at 300 K. In QA276 the 34 meV activation energy is also the CHHL process but in this case the light hole state is not confined so the process is a type-II transition to the light hole state in the GaSb barrier. Given the likely high density of defect in this sample the activation energy could also be the ionisation of a defect state, which would be consistent with the low Z value.

5.4 Improved AlGaSb IMF

The superior 300 K performance of QJ410 merited further optimisation of the GaInSb/AlGaSb MQW IMF. The growth of QJ410 (T_S=515 ℃) was repeated with all conditions identical except for the substrate temperature which was 495 ℃(QJ437), as seen in Figure 5.13a this resulted in an increase in the FWHM of 70% and still no evidence of pendellösung fringes.

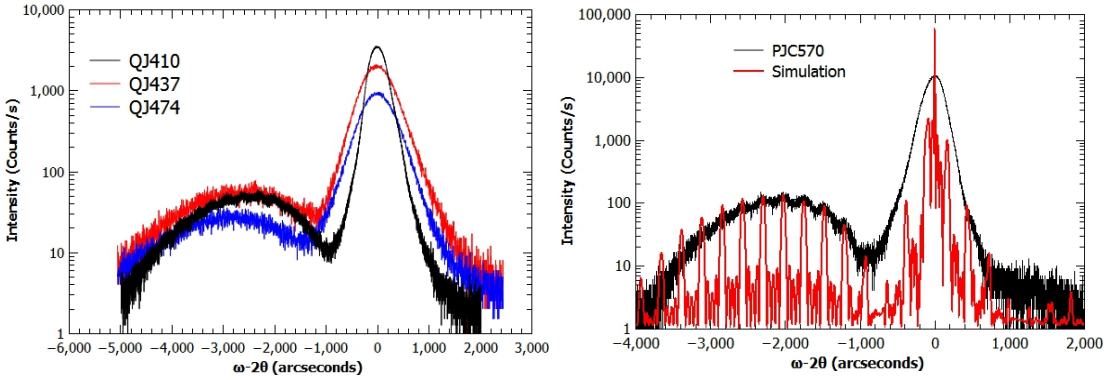

(a) (b)

Figure 5.13: (a) X-ray diffraction pattern of QJ410, QJ437 and QJ474 AlGaSb IMFs with GaInSb MQWs grown at substrate temperatures of 515 ℃, 495 ℃ and 515 ℃ respectively. The quantum wells in QJ410 and QJ437 were grown at the same temperature as the buffer layer, in QJ474 they were grown at 500 ℃. There is no evidence of the pendellösung fringes in any sample. (b) X-ray diffraction pattern of PJC570, grown with a substrate temperature of 510 ℃ and the wells at 470 ℃, at each interface of the quantum wells growth was paused under a antimony flux for 5 s. Included is the simulated diffraction pattern.

The next sample aimed to grow the buffer layer and quantum wells at temperatures closer to the ideal for each. The buffer of QJ474 was grown at T_S=515 ℃ as in QJ410, but before the quantum wells and barriers were deposited, the substrate temperature was reduced to 500 ℃. The FWHM was increased by a further 11%; the cause of this is believed to be due to the very low growth temperature of the AlGaSb barriers.

A fourth sample, PJC570, was grown with a substrate temperature of 510 ℃. The

buffer layer in this sample had a slightly lower aluminium content at 44%. The quantum wells and barriers were grown at 470 °C. The composition, was confirmed by x-ray diffraction was five 10 nm $Ga_{0.77}In_{0.23}Sb$ quantum wells with 57 nm barriers of $Ga_{0.56}Al_{0.44}Sb$. At each interface the growth was paused and the sample remained under antimony flux for 5 s before growth continued. Figure 5.13b shows the resultant x-ray diffraction pattern. A reduction of 40% is seen in the FWHM of the AlGaSb peak, and the pendellösung fringes have become visible indicating the superior crystalline quality. It is believed the pause in growth gives the layers time to stabilise before they are capped by the next layer, utilising the antimony flux as a surfactant.

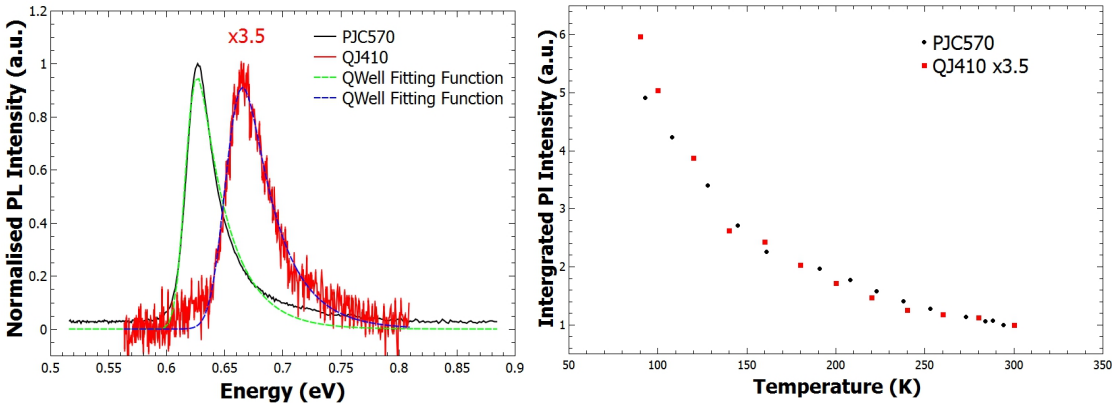

(a) (b)

Figure 5.14: (a) 300 K photoluminescence spectra of QJ410 and PJC570 along with the fitting function (Equation 2.15). (b) Comparison of the integrated PL intensity of QJC570 and QJ410 normalised at 300 K.

Figure 5.14a shows the 300 K photoluminescence spectra of QJ410 and PJC570. PJC570 has superior high temperature luminescence with an intensity 3.5 times greater thhat QJ410. The FWHM of PJC570 is 32 meV, not much greater than that expected from thermal broadening (26 meV) whereas the FWHM of QJ410 is 45 meV. Both spectra are fitted with the function outlined in Equation 2.15

$$I_{PL}(h\nu) = A\left[\text{erfc}\left(\frac{E_g - h\nu}{\sigma\sqrt{2}}\right)\exp\left(-\frac{h\nu - E_g}{k_B T}\right)\right]$$

where erfc is the complimentary error function, σ is a fitting parameter to take into account inhomogeneous broadening, E_g is the bandgap, T is the lattice temperature and k_B is Boltzmann's constant. The band gap energies of QJ410 and PJC570 at 300 K were 657 meV and 619 meV respectively. This function provides a much better fitting of the data at high temperatures where carriers have higher thermal energy. σ was 11.1 meV for QJ410 and 7.1 meV for PJC570, an improvement of 37%, a similar level of improvement to that seen in the x-ray FWHM. The larger the value of σ, the greater the broadening; the cause of the broadening is poor structural quality, alloy localisation or interface roughness. Given the TEM images of QJ410 indicating rough interfaces, it is believed that the pause in growth at the quantum well interfaces has improved the abruptness. The antimony flux provides a surfactant effect which stabilised the individual layers before they are capped by the following layer. The improved interface abruptness indicated in the 300 K photoluminescence is consistent with the x-ray where improved interface abruptness in PJC570 was indicated by more clearly defined fringes. Whilst there was a 5 ℃ difference in well growth temperature between QJ410 and PJC570 (515 ℃ to 510 ℃) the effect of greater temperature differences in previous sample was less than seen between QJ410 and PJC570. Figure 5.14b shows the integrated intensities of QJ410 and the improved sample grown with epilayer interface pauses (PJC570). The intensity of the photoluminescence quenches at a greater rate in the QJ410 and the intensity remains inferior to PJC570 even down to 80 K. The activation energies associated with the quenching of the photoluminescence signal are 36 meV and 15 meV. The 36 meV process is attributed to the CHHL process. As for the 15 meV process, given the quantum well potential, the possibility of loss of carrier confinement is discounted. The CHSH and IVBA processes as they are forbidden due to $\Delta_{SO} > E_g$ (Δ_{SO}=790 meV). The activation energy of CHCC was calculated as 56 meV this also can be discounted. The remaining possibilities are ionization of shallow Si or Ge donors (10 & 9 meV). This would imply that PJC570 is an improved iteration of QJ410 and that whilst the defect processes are

still the cause of quenching this rate has reduced. Intensity measurements at a range of temperatures down to 4 K would be required to provide a value of I_0, which would allow a more accurately determined the activation energy.

5.5 Growth of InGaSb Quantum Well LEDs

A sample (QJ403) was grown using the same quantum well dimensions and composition as QA216 as the active region of a p-i-n junction. A quarter wafer of n-GaSb was used as the substrate. After the native oxide desorbed, 700 nm of n-GaSb (n=6×10^{18}cm^{-3}) followed by 300 nm of intrinsic GaSb were deposited. Three 6 nm $Ga_{0.65}In_{0.35}Sb$ wells with 50 nm GaSb barriers where capped with 200 nm of GaSb. To improve the efficiency of the device, an electron blocking layer consisting of 20 nm of p-$Ga_{0.70}Al_{0.3}Sb$ (p=8×10^{17}cm^{-3}) was included to confine the electrons to the active region. This was followed by a 600 nm p-GaSb layer (p=2×10^{18}cm^{-3}). The entire sample was grown with a substrate temperature of 510 ℃. X-ray diffraction indicated that the quantum wells were in fact 7.2 nm wide with a composition of 34% indium.

To test the properties of a sample with an IMF (QJ414), a doped variant of QJ410 was chosen due to the superior photoluminscence exhibited when compared to the GaSb IMF samples. A n-GaAs quarter wafer was heated under arsenic flux until the native oxide layer was removed, the substrate was cooled to 575 ℃ and 100 nm of n-GaAs (n=6×10^{18}cm^{-3}) was grown. After the growth of an IMF as outlined for QJ410 the substrate was further cooled to 515 ℃ and 500 nm of n-$Ga_{0.56}Al_{0.44}Sb$ (n=6×10^{18}cm^{-3}) and 100 nm of intrinsic AlGaSb were grown, followed by five 6 nm $Ga_{0.65}In_{0.35}Sb$ quantum wells with $Ga_{0.56}Al_{0.44}Sb$ barriers. A further 100 nm of AlGaSb was deposited, followed by 400 nm of p-AlGaSb (p=6×10^{18}cm^{-3}). A 50 nm p-GaSb (p=1×10^{19}cm^{-3}) cap was added to protect the AlGaSb from oxidation and to improve the contact bonding. The samples were etched into 800 μm diameter mesas as outlined in Section 4.4. The contacts

formed on GaSb consisted of 20 nm of titanium and 200 nm of gold. For the n-GaAs a 20 nm layer of Au/Ge at a ratio of 88:12 by weight was followed by 200 nm of gold and annealed at 400 ℃. The n-type contact on each device was deposited of the back of the substrate meaning the devices used top-bottom contacts. This results in the current having to cross the IMF interface in QJ414.

5.5.1 Electrical Properties

Figure 5.15 shows the current voltage relations of these two devices once mounted on to a TO-46 header. The series resistance for QJ403 is 1.5 Ω and 6.7 Ω for QJ414. The increased resistance is consistent with the presence of the IMF layer[138]. Parallel resistances were 1.67 kΩ and 675 Ω for QJ403 and QJ414 respectively.

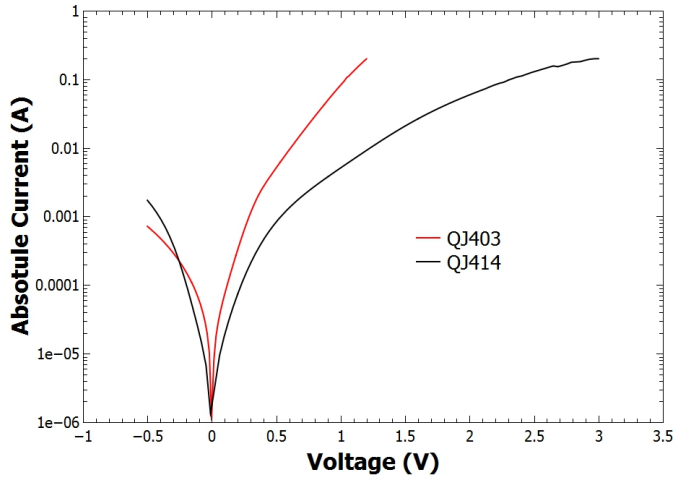

Figure 5.15: Probe station I-V curves for a $Ga_{0.65}In_{0.35}Sb$ MQW LED grown on GaSb(QJ403) and using an AlGaSb IMF(QJ414).

The lower resistance of QJ414 indicates a greater number of carriers bypassing the active region and not recombining. This can be attributed to increased defects. Ideality factors of 10 for QJ414 and 7 for QJ403 further indicate a large number of carriers bypassing the active region.

5.5.2 Electroluminesence

QJ414 did not emit any light, even when cooled to 4 K. The presence of a large potential at the GaAs/AlGaSb interface is believed to be the cause of this, blocking the electrons for reaching the active region. This can be seen in Figure 5.16 where the electron density is highest at the AlGaSb/GaAs interface. This is caused by charge transfer between the two layers because of the different potentials. To a lesser degree the same is effect blocks the diffusion of holes at the GaSb/AlGaSb interface. This means the carriers are spatially separated.

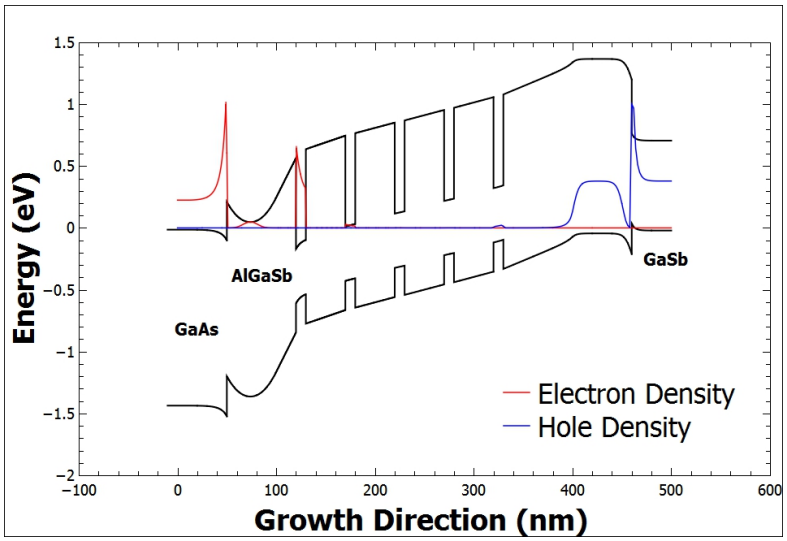

Figure 5.16: Band diagram of QJ414 showing the simulated electron and hole densities. The majority of electrons are trapped by the potential at the GaAs/AlGaSb interface. The holes will be confined by the GaSb/AlGaSb interface.

The 4 K spectra of QJ403 is shown in Figure 5.17a. A deconvolution of the spectra shows a peak consistent with the e_1-hh_1 transition as modelled in nextnano®. The fitting was achieved using equation 2.15, with a bandgap of 682 meV, σ of 4.7 meV and carrier temperature of 62 K. Using equation 5.2, the FWHM of the e_1-hh_1 transition indicates a quantum well surface roughness of approximately two monolayers. Z analysis of the power varied spectra at 4 K indicated a value of 1.3 at low injection currents, indicating a

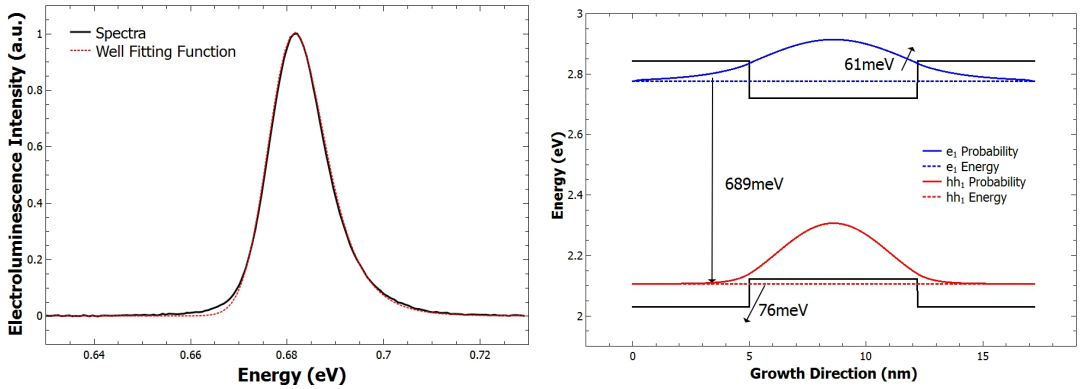

(a) (b)

Figure 5.17: (a) 4 K electroluminescence spectra of QJ403 at 200 mA 1% duty cycle 1kHz. Fit using equation 2.15 for the e_1-hh_1. (b) nextnano® simulation of QJ403 at 4 K with transition energies and confinement energies.

dominance of SRH which switches to a value of 2.5 at 240 mA injection current, indicating a shift to Auger dominance. The Z value of less than 2 at low currents suggests that crystal quality and defects are present in the device.

The 300 K electroluminescene is shown in Figure 5.18a. The fitting with equation 2.15, provides good agreement with the measured spectrum for the lowest energy transition. This peak is attributed to the e_1-hh_1 transition. The fitting parameters give a lattice temperature of (300±10) K which is consistent with the measured temperature of the device. The broadening parameter σ was 3.4 meV at 300 K compared to a value of 4.7 meV at 4 K. The broadening can be caused by poor structural quality, alloy localisation or interface roughness. In this instance, given the FHWM measurements using equation 5.2 it is likely that an interface roughness of 2 ML is causing this broadening, and as fewer carriers are confined to these localisations, the broadening effects they produce are reduced. The second fitted peak is attributed to the GaSb barriers and is fitted with a simple Gaussian. This indicates that not all carriers are remaining in the wells at high temperatures.

Temperature varied spectra were measured, and the peak wavelength was converted

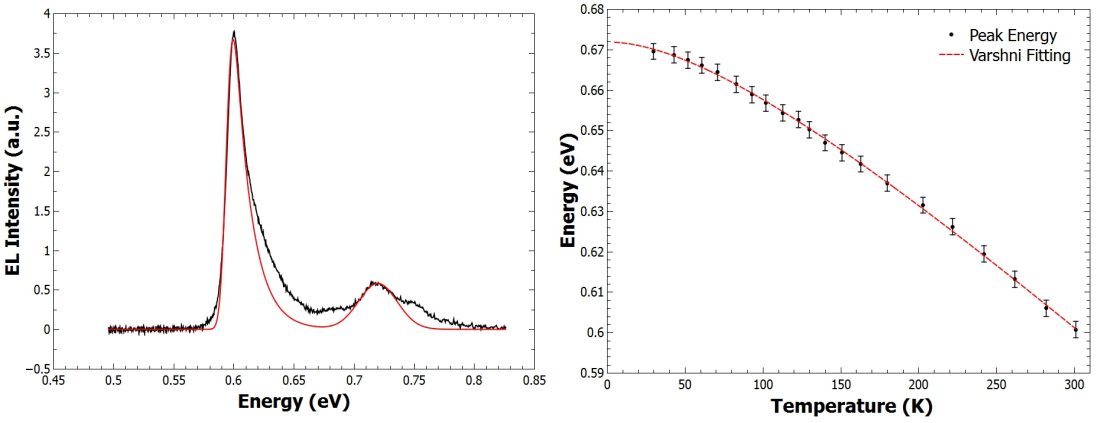

(a) (b)

Figure 5.18: (a) 300 K electroluminescence spectra of QJ403 at 200 mA 50% duty cycle 1kHz (Black line). The main peak is the e_1-hh_1 transition with a fitting using equation 2.15. The Gaussian relates to the GaSb barrier layers, the summation of these two fittings is given as the red line. (b) Varshni fitting of the transition energy of QJ403 as a function of temperature.

to transition energy as shown in Figure 5.18b. A Varshni fitting resulted in fitting values of $E_g(0)$=0.670 eV, α=0.4 meV/K and β=109 K. These values are within 15% of those of GaSb, which forms the majority of the quantum wells. The activation energies of QJ403 are 12 meV and 130 meV. The latter of which is equal to the thermal escape of both carriers, where their recombination would be consistent with the peak seen in Figure 5.18a. The 12 meV process could be the ionization of a Te donor (20 meV) or a Be acceptor (9 meV) both of which are used as dopants in the device.

5.6 Growth and Characterisation of GaAs/InAlSb IMF

As a further development of ternary IMF interfaces, growth was also pursued with which there is no common atom across the interface. To this end a sample was grown with a GaAs/AlInSb interface (QM412). 100 nm of GaAs was grown at a substrate temperature of 575 ℃. The gallium shutter was closed and the substrate subjected to 1 minute of arsenic flux. This was followed by 20 seconds of no flux allowing the surface

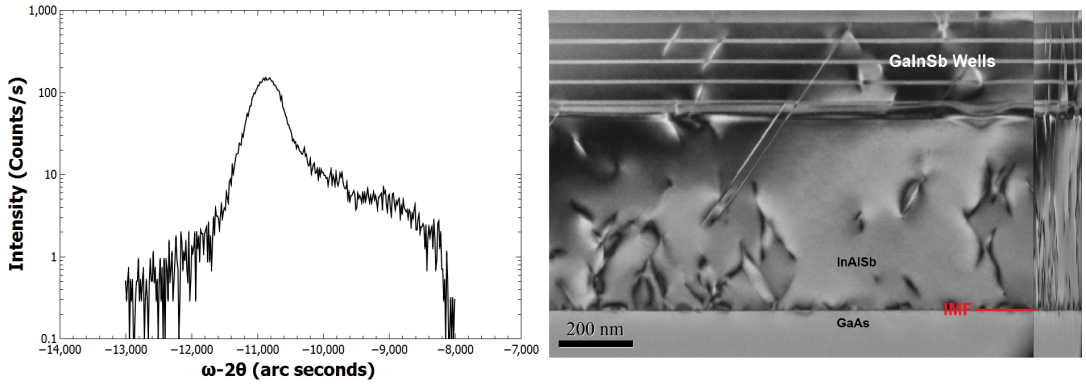

(a) (b)

Figure 5.19: (a) X-ray diffraction pattern of QM412 an AlInSb IMF with GaInSb MQWs there is no evidence of the pendellösung fringes. The wells are under tensile strain. (b)TEM image of the IMF layer and quantum wells. The first two wells are poorly defined and well quality improves in subsequent layers.

to become gallium rich. 2.5 minutes of antimony flux was followed the opening of the aluminium and indium shutters, and a 500 nm buffer of AlInSb was grown. 5× 10 nm $In_{0.15}Ga_{0.85}Sb$ quantum wells were grown with AlInSb barriers. The lattice constant of the AlInSb layer is greater than that of the InGaSb quantum wells meaning the wells are under tensile strain.

X-ray diffraction as shown in Figure 5.19a indicates a barrier composition of $Al_{0.89}In_{0.11}Sb$. There is no evidence of pendellösung fringes which is consistent with the TEM image seen in Figure5.19b. This indicates the wells are between 10 nm and 12 nm but also that the first two wells do not seem to have formed. In several images there is evidence of periodicity in the GaAs/AlInSb interface indicative of IMF. Unfortunately the magnification is insufficient to verify or measure the period against the expected 3.39 nm which would relate to every 12 GaAs sites and 11 AlInSb. Compared to the AlGaSb IMF there is an increased dislocation density of $5\times10^{10}/cm^2$, 20 times greater than that seen in QJ410. Given the improvements seen in PJC570 this could be greater still but TEM images would be required. Of the five quantum wells grown there is clear evidence of

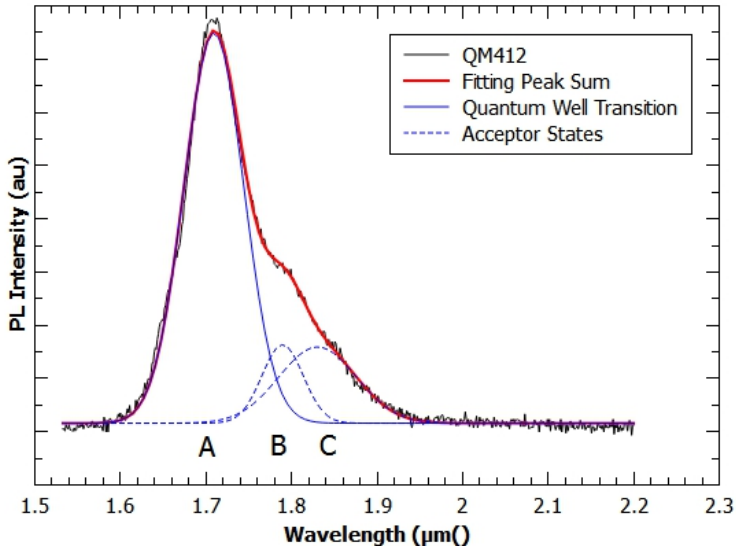

Figure 5.20: 4 K photoluminescence spectrum of QM412 with Gaussian fittings showing the quantum well transition(A) and transitions via the defect states caused by Ge and GaSb native defects(B & C).

the last three. The first two appear intermingled and poorly defined, this is in direct contrast to QJ410, where well quality degraded in subsequent wells.

The 4 K photoluminescence spectra shown in Figure 5.20 reveals a main peak (A) with an energy of 725 meV. This compares well with the nextnano® simulation of 723 meV with a FWHM of 34meV. Peaks B and C have a transition energy 32 meV and 48 meV less than the e_1-hh_1 transition; as e_1 is 72 meV above the conduction band edge, both states are above the valence band, by 8 meV for B and 24 meV for C. This would suggest peak B is the Be acceptor (9 meV) and peak C the native defect in GaSb (30 meV). Using equation 5.2 the well roughness is calculated to be 16 nm. This is greater than the width of the wells, which is not consistent with the TEM images. It is assumed to be a consequence of the distortions in the first two quantum wells.

5.7 Summary

The work in this chapter was undertaken to investigate the suitability of $Ga_{(1-x)}In_xSb$/GaSb (x=0.25–0.35) quantum wells for use in high power LEDs in the 2 μm region. GaInSb quantum wells with GaSb barriers have been grown on GaSb. GaInSb quantum wells have also been grown on GaAs using both GaSb and $Al_{0.5}Ga_{0.5}Sb$ barriers with IMFs. This is the first reported ternary IMF; TEM images reveal a periodic dislocation every 4 nm equal to 13 AlGaSb and 14 GaAs lattice sites with a defect density of $2\times10^9/cm^2$. Only one order of magnitude greater than GaAs/GaSb IMF growth on the same system[128].

The GaInSb/GaSb material system provides an avenue to achieving 2 μm light emission, however, poor carrier confinement in the quantum wells limits the output of devices made from this material. The introduction of AlGaSb barriers, through the use of an AlGaSb IMF, resulted in reduced thermal quenching in photoluminescence samples. This was evident in the superior 300 K signal found in these samples. Quantum well interface abruptness was poor in initial samples, which is believed to have be caused by the mismatch in optimal growth temperatures of GaInSb and AlGaSb.

Growth was improved by the use of a growth interrupt under antimony flux between layers. These growth interrupts resulted in a threefold increase in signal and a 30% reduction in FWHM for the room temperature photoluminescence. This improvement was also seen in the x-ray diffraction pattern where the AlGaSb peak FWHM reduced by 40% and the pendellösung fringes became visible.

The improved photoluminescence properties exhibited by the AlGaSb samples were not replicated in the LEDs made from this material. It was not possible to measure an emission spectra for the sample; it is believed that this is due to the carriers becoming blocked at the GaAs/AlGaSb interface. Interaction with the dangling bonds in the IMF was also detrimental to the function of the device. To develop further AlGaSb devices grown on IMF, it would be recommended to use a device design utilising top-top contacts

so as to bypass the GaAs/AlGaSb interface altogether. For the top contact, a gradated interface between the AlGaSb and GaSb layers and doping the GaSb layer is needed so that the holes can migrate unhindered.

Tentative steps to producing an IMF interface between GaAs and InAlSb were taken. The GaInSb wells grown on the InAlSb exhibited superior interface abruptness when compared to wells grown on AlGaSb. The first two wells were poorly formed which is not seen in the other IMF quantum well samples. There is evidence of a greater number of defects in this sample compared to AlGaSb IMF with a density of $5\times10^{10}/\mathrm{cm}^2$.

Overall, the use of GaInSb quantum wells produced the desired emission wavelength but poor confinement resulted in diminished room temperature operation. Room temperature output power was $0.4\,\mu$W Whilst AlGaSb barriers increased the confinement, the resulting band discontinuity at the GaAs/AlGaSb interface made conventional top-bottom LEDs non-functional. In the next chapter, the GaSb/InGaSb quantum well LED will be compared to other devices to evaluate the benefits inherent in the use of quantum wells verses other quantum structures.

Chapter 6

Comparison of LEDs with Different Degrees of Quantum Confinement Emitting at 2 μm

6.1 Introduction

It is possible to produce LEDs emitting at 2 μm from a variety of quantum structures as well as bulk materials. Whilst the benefits of each system are often discussed with regards to laser diodes, the specific requirements of LEDs are rarely considered, as these are often merely produced as a precursor to lasers. In this chapter, the figures of merit will be determined for a bulk alloy LED as well as those of a quantum well, dash and dot, based active region to determine the most suited to LEDs which will be used as part of an enhanced flight vision system.

6.2 GaInAsSb/AlGaAsSb Double Heterojunction LEDs

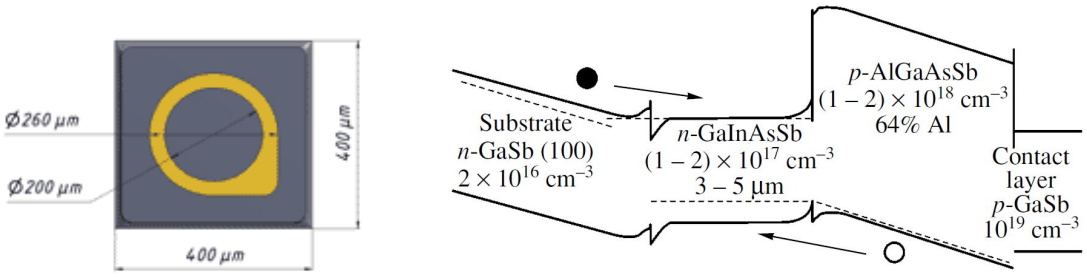

(a) (b)

Figure 6.1: (a) Schematic of the IBSG LED22 mesa and (b) Band diagram of LED22

To be able to compare the devices produced for this section a bulk $Ga_{0.78}In_{0.22}As_{0.15}Sb_{0.85}$/ $Al_{0.4}Ga_{0.6}As_{0.04}Sb_{0.96}$ heterojunction was purchased (LED22) and characterised to act as a benchmark for the devices discussed in this chapter. The device was chosen as it was the highest power bulk heterojunction design commercially available at 2μm. It was produced by IBSG company (Independent Business Scientific Group), St. Petersburg, using liquid phase epitaxy (LPE) growth on a GaSb substrate, to which all layers are lattice matched. Whilst the exact composition of LED22 is not known, IBSG company

Temperature	R_S	R_P	Ideality Factor
77 K	3.7Ω	14 MΩ	1.7
300 K	3.1Ω	165 kΩ	2

Table 6.1: Series resistance (R_S), shunt resistance (R_P) and ideality factor of bulk alloy LED at 77 K and 300 K.

is a spin-off of the Ioffe Institute. It is believed LED22 is a commercialisation of the work presented in the work of Stoyanov *et al.*[49]. A schematic of the chip is shown in Figure 6.1a.

6.2.1 Current – Voltage Characteristics

Measuring the I–V characteristics of the device can show the presence of defects within the device and provide details on leakage currents. A $\log_{10}$I–V plot is shown in Figure 6.2. There is evidence of sub-threshold turn on (a non abrupt turn on), which indicates the presence of defects or surface recombination states.

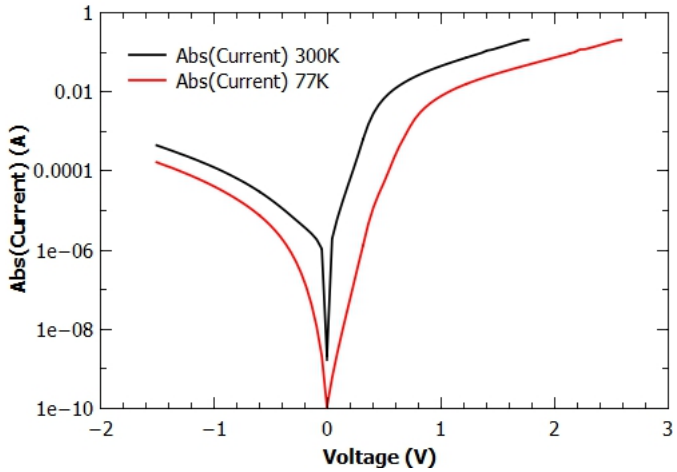

Figure 6.2: $\log_{10}$I-V plots for LED22 at 77 K and 300 K.

The series resistance (R_S) at low current(<10mA) (Table 6.1) is low and indicative of good quality contacts. The reduced shunt resistance (R_P) indicates that there are some defect states that are allowing carriers to bypass the p-n junction. This is supported

by the ideality value of 2 indicating the presence of traps. The relatively large series resistance at operating currents (200 mA) indicates there will be problems with Joule heating.

6.2.2 Electroluminescence

The device was placed in the Oxford Instruments Dry cryostat and cooled to 5 K. Spectra were taken at 20 mA intervals between 20 mA and 200 mA using a 50% duty cycle 1 kHz signal (henceforth referred to as qCW). These drive conditions were chosen as they are recommended by the manufacturer and are commonly used by other commercial manufacturers. Further current–light (I–L) measurements were taken up to 750mA using 1% duty cycle to reduce the effects of Joule heating. These measurements were repeated every 50 K up to 300 K.

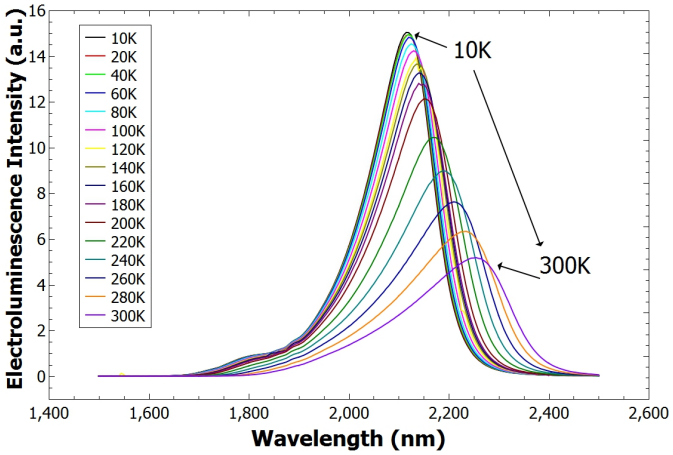

Figure 6.3: Temperature varied electroluminescence from 10 K to 300 K, showing a decrease in intensity of 50%. Peak room temperature emission occurs at 2.25 μm. Device was driven at 200 mA with a 50% duty cycle.

Between 4 K and 300 K the intensity of the light emitted halved (Figure 6.3). This indicates a weak influence of thermally quenching processes. By plotting the integrated intensity of EL emission against $\frac{1}{kT}$, where k is Boltzman constant and T is temperature,

we can determine the activation energy (as shown in Figure 6.4) by using the Arrhenius fitting function;

$$I = \frac{I_0}{1 + A\exp^{-(E_a/k_BT)} + B\exp^{-(E_b/k_BT)}} \tag{6.1}$$

where I is the intensity, I_0 is the intensity at 0 K, A & B are the rates of each process and E_n are the activation energies.

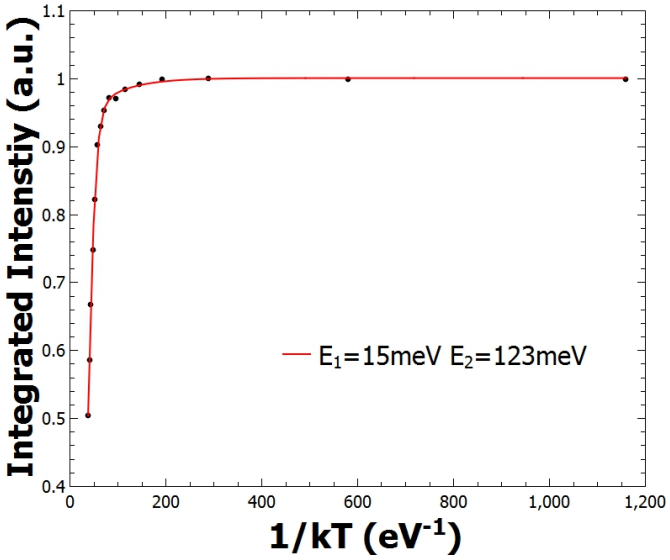

Figure 6.4: Activation energy plot of LED22, a bulk InGaAsSb/AlGaAsSb LED. The fit indicates an Arrhenius function with activation energies of 123 meV and 15 meV associated with the thermal escape of holes and CHSH Auger process respectively.

The activation energies of LED22 were fitted as 123 meV and 15 meV. The former is believed to be the thermal excitation of a carrier into the AlGaAsSb barriers. This can not however be confirmed without exact knowledge of the band structure. The 15 meV activation energy can be attributed to either an excitation of carriers out of an interface band minima or the presence of a Mn trap state (20 meV)[45]. A possible origin for this Mn would be contamination of the LPE boat used to produce the semiconductor. At room temperature, the thermal escape of holes is the key loss process in the device. At temperatures below 200 K the 15 meV process dominates. Without an exact knowledge

of the composition of the device, due to commercial sensitivity it it not possible to determine exactly where the processes occur.

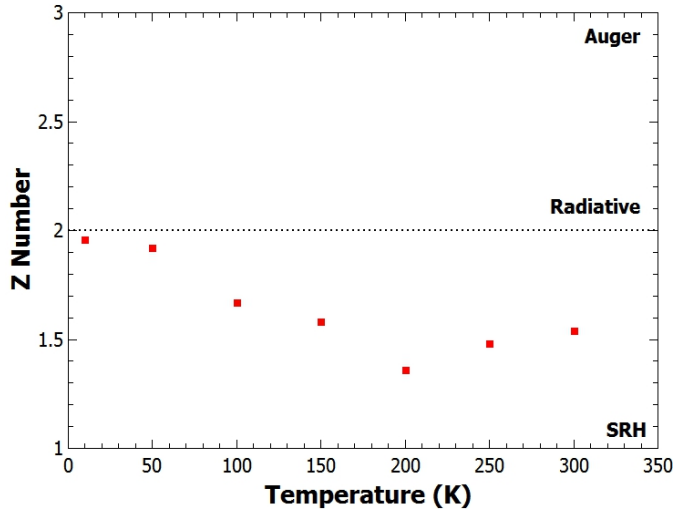

Figure 6.5: The decrease in Z number with temperature due to increased SRH followed by Auger recombination increasing beyond 200 K resulting in the Z number increasing. Taken from power varied measurements with 1% duty cycle to reduce Joule heating.

To further determine the recombination processes, Z analysis was undertaken every 50 K between 10 K and 300 K, taking natural logarithms of light intensity (L) against current (I) such that

$$Z = 2\frac{\ln I}{\ln L} \tag{6.2}$$

where Z is the average number of carriers per recombination. One carrier would indicate Shockley-Read-Hall recombination (SRH), two would be radiatively dominated and three would be indicative of strong Auger recombination. However, as an exception to this, a poor quality sample with weak PL signal could also give a Z value of 2 if it is equally limited by Auger and SRH. Figure 6.5 shows the Z number as a function of temperature. It can be seen that after an initial start at 10 K with a Z value of approximately 2, indicating purely radiative recombination. There are some defect states that activate as the sample warms increasing the SRH rate as indicated by the decrease in Z value.

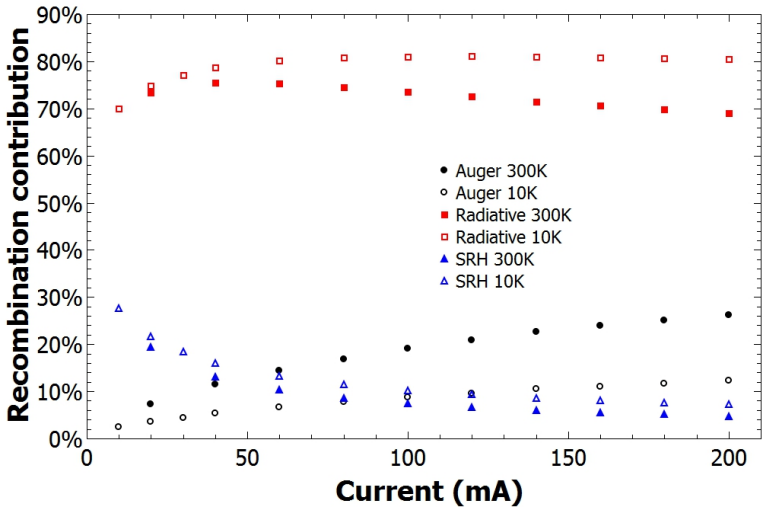

Figure 6.6: Breakdown of the recombination processes present in LED22 at room temperature and 4 K. Calculated from the 1% duty cycle I–L curves.

It is also possible to determine how much each process contributes to the overall carrier recombination, Gadedjisso-Tossou *et al.* showed that the light emitted (R_{spon}) is proportional to Bn^2 where B is the radiative rate and n is the carrier concentration, thus $\sqrt{R_{spon}} \propto n$. Combining this with $I \propto An + Bn^2 + Cn^3$, where A,B and C are the SRH, Radiative and Auger coefficients, it can be shown that[139];

$$\frac{I}{\sqrt{R_{spon}}} \propto A + Bn + Cn^2 \tag{6.3}$$

By plotting $\frac{I}{\sqrt{R_{spon}}}$ vs $\sqrt{R_{spon}}$, a quadratic curve is produced, for which a fitting will extract values for A, B and C. Using $\sqrt{R_{spon}}$ as a proxy for n, then the rates of each process can be calculated and their percentage of the recombination current determined. The result of this is shown in Figure 6.6. Because the current is not directly measured in this technique but inferred from the $\sqrt{R_{spon}}$, the presence of leakage current is not included as it is the proportion of recombination not total current.

As expected, the SRH reduces in effect as carrier densities increase and defect states become saturated. The increase in Auger contribution between 4 K and 300 K is also

consistent with the Z analysis seen in Figure 6.5. By comparing the observed halving of output power with the smaller decrease in radiative rate recombination seen in Figure 6.6 we can infer that the loss of output power is determined by a reduction in the number of carriers not recombining. Possible causes for this could be the thermal excitation of carriers out of the active region. This is supported by the activation energy which indicates carrier leakage to be the key loss mechanism.

6.2.3 Power and Efficiency

The power output was measured by placing the LED in an integrating sphere in front of an 77 K InSb detector connected to a lock in amplifier. Factoring in the gain on the preamp, and the ratio of integrating sphere surface area to output hole, it is possible to determine the current produced by the detector. With the responsivity of the detector known, the output power of the LED can be determined. The output power of the device when operating at 300 K with a drive current of 200 mA qCW was measured as 0.5 mW. This gives an external quantum efficiency of 0.43% and a wall plug efficiency of 0.14%. The difference in these two values can be attributed to loss of energy in each electron hole pair, imparted by joule heating and scattering. The difference between the energy acquired by each electron hole pair from the power source and the mean photon energy is known as the 'feeding efficiency'[140].

6.2.4 Summary

To conclude, a bulk InGaAsSb/AlGaAsSb heterojunction grown by LPE is an easy way to achieve a reasonably high power device (0.5 mW) which results in a power density (brightness) of 1.5 $mWmA^{-1}cm^{-2}$. The broadness (200 nm FWHM) of the emission would reduce any negative effects of absorption in the atmosphere. The main limitation on increased output from the device is thermal loss of carriers to the confining AlGaAsSb barriers. The introduction of a penternary active region could improve the output of

the device by engineering the $\Delta E_{v/c}$ to change the vacuum energy of the active region, improving the carrier confinement. However the effect this will have would be minimal as the carriers are already confined ≈5kT.

6.3 GaInSb/GaSb Quantum Wells

To measure the properties of an LED containing quantum wells, device QJ403 developed in the previous chapter was tested. The structure of which is shown in Figure 6.7a.

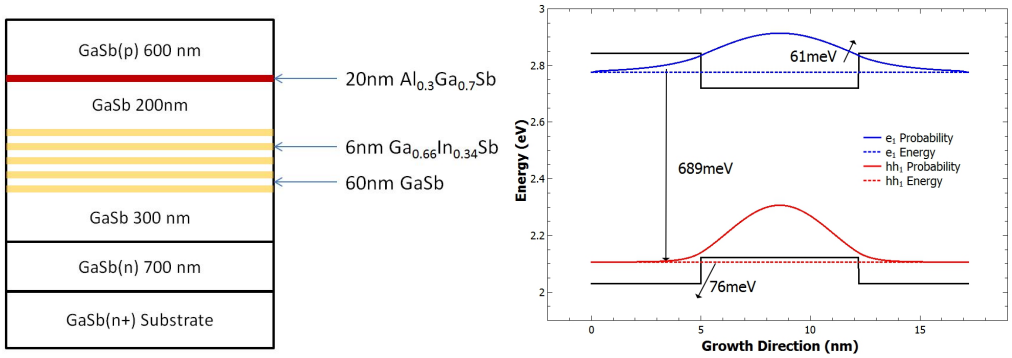

(a) (b)

Figure 6.7: (a) Schematic of QJ403 a GaInSb MQW LED. (b) Band structure of a single quantum well.

6.3.1 Current – Voltage Characteristics

Figure 6.8 shows the current voltage relation of the LED. The series resistance of 1.7 Ω indicates that the contacts are of good quality, however, the very low parallel resistance of 1.8 kΩ indicates that carriers bypassing the active region is a key concern in this device. This is supported by the ideality factor of 5.8. The device failed before 77 K testing could occur.

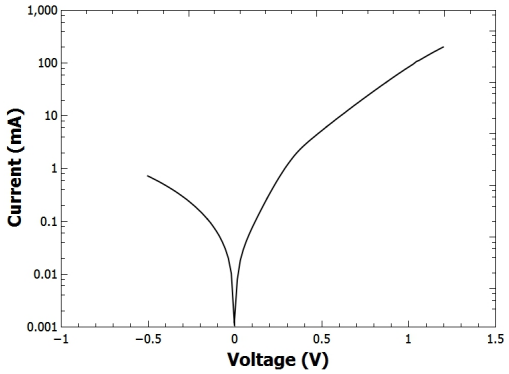

Figure 6.8: $\log_{10}$I-V plot of QJ403 at 300 K with a series resistance of 1.69 Ω and shunt resistance of 1.8 kΩ. The device has an ideality factor of 5.8.

6.3.2 Electroluminescence

A 800 μm diameter surface emitting mesa was produced using the techniques outlined in Section 4.4. Individual mesas were cleaved and mounted on a TO-48 header. The completed device was placed in the Oxford Instruments OptistatDry cryostat with the LED orientated such that the emission from the top of the mesa was directed at the collection optics.

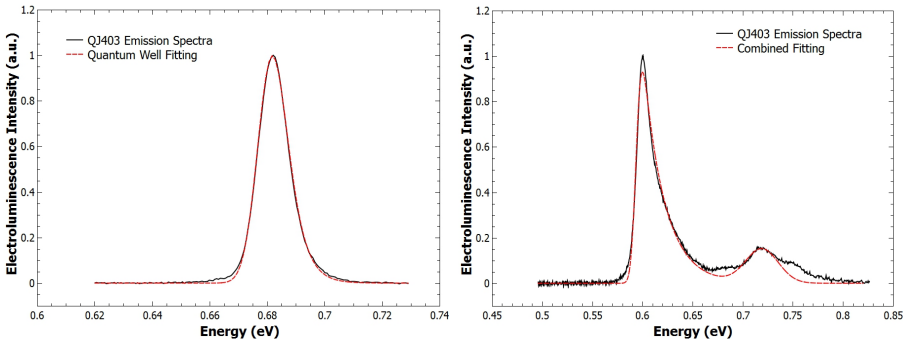

(a) (b)

Figure 6.9: (a) 4 K electroluminescence of QJ403. Fit using equation 2.15(red line). (b) 300 K electroluminescence spectra of QJ403 showing the quantum well peak on the left and a higher energy peak attributed to the GaSb barriers. Black line is the measured spectra; the red line is the summation of a fitting of the quantum well e_1-hh_1 transition and of the GaSb transition. The device was driven at 200 mA with 5% duty cycle.

The 5 K electroluminescence spectra is given in Figure 6.9a. This was fitted using equation 2.15;

$$I_{EL}(h\nu) = A\left[\text{erfc}\left(\frac{E_g - h\nu}{\sigma\sqrt{2}}\right)\exp\left(-\frac{h\nu - E_g}{k_B T}\right)\right]$$

where erfc is the complimentary error function, σ is a fitting parameter to take into account inhomogeneous broadening, E_g is the bandgap, T is the lattice temperature and k_B is Boltzmann's constant. The resulting fitting parameters are: E_g=684 meV, σ=4.5 meV and k_BT=4.2 meV.

Upon heating to 300 K the light intensity decreased by a factor of 100. The activation energy of this thermal quenching was calculated using a fitting of equation 6.1 on a plot of the integrated electroluminescence intensity against 1/kT.

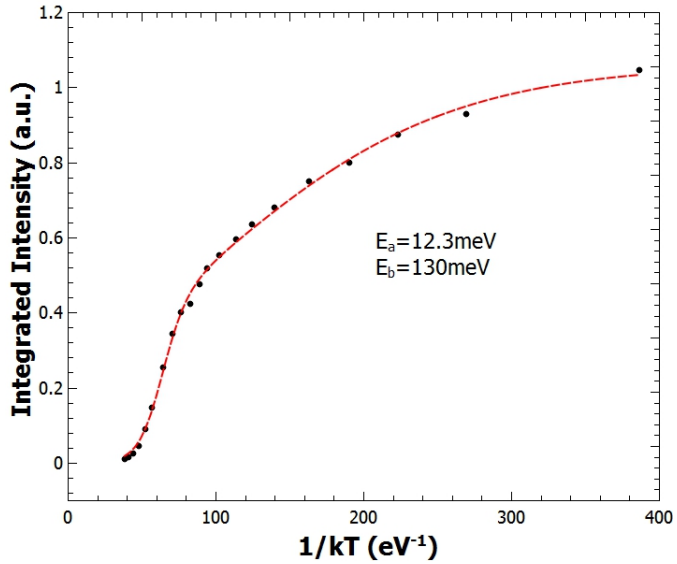

Figure 6.10: Arrhenius fitting of integrated intensity of QJ403. Fitting gives activation energies of 12.3 meV and 130 meV.

The two activation energies were 130 meV and 12.3 meV. The former is approximately equal to the loss of an electron hole pair from the quantum well which modelling suggests has an energy of 128 meV (Figure 6.7b). The 12.3 meV activation energy could be the ionisation of a silicon acceptor as this has an ionisation energy of ∼10 meV, though

as silicon is not used in the system the device was grown in the source of this is unknown. This process dominated up to temperatures of 170 K. It is not one of the Auger recombination processes as CHSH and IVBA are suppressed when $E_g < \Delta_{so}$ as is the case in this sample (Δ_{so}=840). The calculated activation energy of CHCC is 77 meV so this also cannot be the dominant quenching process. The presence of the GaSb peak at temperatures of 200 K and higher supports the view that the quenching is due to the escape of carriers from quantum wells. This is consistent with the findings of the previous chapter. Analysis of the recombination pathways at 300 K was not possible with the device as the signal was too weak to get measurable spectra over a range of currents.

6.3.3 Power and Efficiency

At 300 K under qCW drive conditions, with a current of 170 mA, the output power of the InGaSb MQW LED was 0.4 μW. This gives an external quantum efficiency of 1.6×10^{-3}% and a wall plug efficiency of 2×10^{-4}%. The drive current of 170 mA was chosen instead of 200 mA which was the preferred drive current for the other samples. This was because the output power began to decrease at this point. This was caused by Joule heating of the sample which was confirmed by the attaching of a thermocouple to the sample.

6.3.4 Summary

This sample has shown poor power output and efficiency, and it appears to be limited considerably by poor carrier confinement as was found with other InGaSb quantum well samples examined in the previous chapter. Without the introduction of larger barriers improving confinement this device does not seem suitable when compared to the power outputs available from other devices.

6.4 InAs Quantum Dashes

A sample of InP quantum dashes (QDash) was acquired from III-V Lab, Marcoussis, France where it was developed as part of the PROPHET network[107]. The growth conditions are outlined in the thesis of K. Papatryfonos[103]. The schematic of the sample can be seen in Figure 6.11.

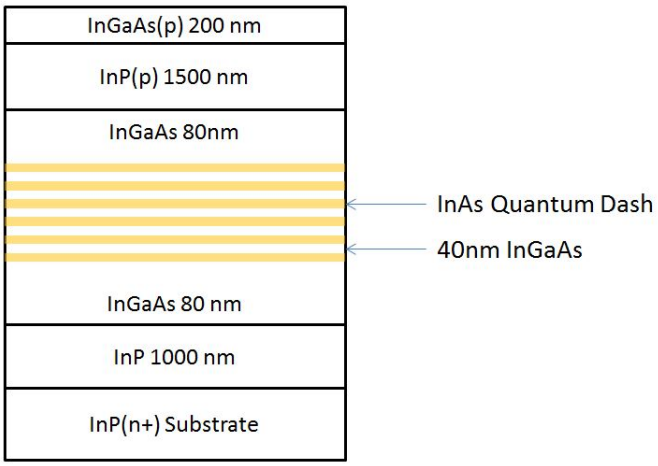

Figure 6.11: Schematic of the Quantum dash LED structure. InGaAs composition is $In_{0.53}Ga_{0.47}As$, lattice matched to InP.

The sample was processed into surface emitting LEDs with assistance from Saurabh Kumar at the Centre for Nanoscience and Technology at the University of Sheffield using the method outlined in Section 4.4.

6.4.1 Current – Voltage Characteristics

The current – voltage curves for the quantum dash LED (Figure 6.12) indicate good quality contacts with a series resistance of 1.7 Ω. The parallel resistance changes greatly between 77 K and 300 K; from 3 MΩ to 750 kΩ, indicating a substantial increase in leakage current. Over the same temperature range the ideality factor changes from 2.8 to 1.6. To ascertain the source of the leakage current I–V measurements where undertaken on mesas of different diameters (d); 800 μm, 400 μm, 200 μm and 100 μm. At 77 K the parallel

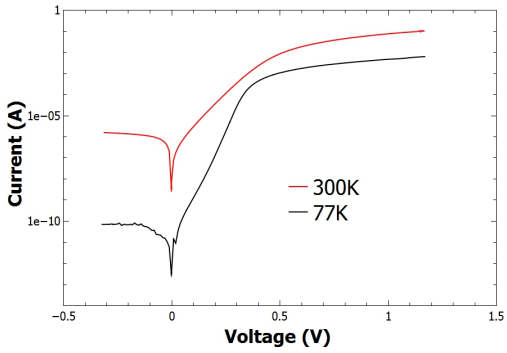

Figure 6.12: Current - voltage relation for quantum dash LED at 77 K and 300 K.

resistance was proportional to $\frac{1}{d}$, indicating that the leakage current was associated with surface recombination. At 300 K the resistance was proportional to $d^{-1.26}$ indicating that whilst surface recombination was still the dominant process, a fraction of the leakage was occurring through defect states in the diode (which has a d^{-2} dependence).

6.4.2 Modelling

Using nextnano®, 2D simulations of the band structure of the quantum dashes were undertaken and fit to the experimental data. It is the height of the dash which defines the confined states within the dash. A dash height of 4 nm gave the best agreement between simulation and experimental results. The resulting 300 K simulation is shown in Figure 6.13a. Several more heavy hole states were possible, but these could not been seen in the spectra, so are excluded from the figure for clarity. Due to strain the light hole band edge of InAs is lower than the valence band of the InGaAs resulting in a type-II transition.

Figure 6.14a shows the fitting of the simulated peaks to the 300 K electroluminescence which are in good agreement. There is a slight offset as the measured peaks are 16 meV above the expected position. This could be due to some gallium migration into the dashes or a small deviation in dash height. The agreement of experimental data and simulation continues down to low temperatures as shown in Figure 6.13b. The peak

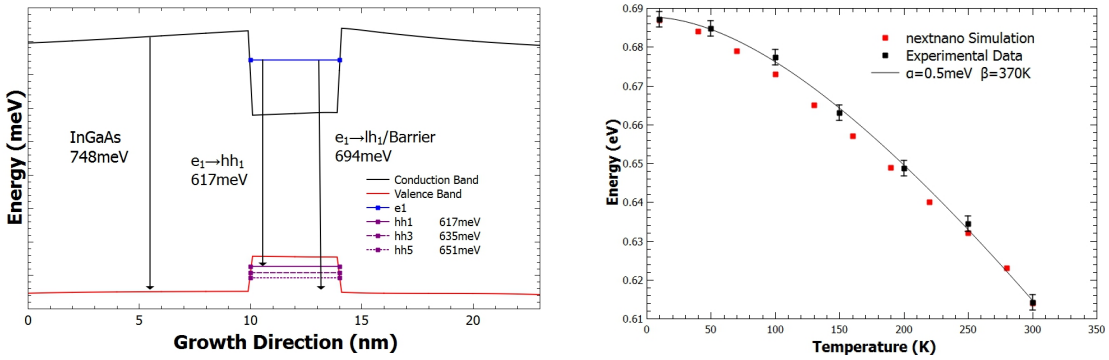

(a) (b)

Figure 6.13: (a) 300 K nextnano® simulation of the band structure of the quantum dash sample. A dash height of 4 nm is used. Shown here is a vertical slice through the 2 dimensional simulation at the center of the dash. Light hole states are not confined due to strain, resulting in a type-II transition. Strain also causes the non-symmetry in the conduction band. (b)Comparison of the experimental transition energy of the quantum dash LED with the nextnano® simulated transition. The Varshni fitting of the LED device is also included (solid line).

emission wavelength of the LED was fitted with the Varshni equation;

$$E_g(T) = E_g(0) - \frac{\alpha T^2}{\beta + T} \tag{6.4}$$

where $E_g(T)$ is the transition energy at temperature T, $E_g(0)$ is the transition energy at 0 K and α & β are fitting parameters. The resulting α & β are 0.5 meV/K and 370 K respectively, far higher than those of InAs (0.27 meV/K and 83 K) but comparable to InP (0.49 meV/K and 327 K).

6.4.3 Electroluminescence

Electroluminescence measurements of the LED were undertaken in the Oxford Instruments OptistatDry cryostat. The LED was orientated such that the emission from the top of the mesa was directed at the collection optics. At low temperature there is evidence of lasing in the sample as manifest by the line narrowing with increased current (inset Figure 6.14b). A high resolution spectrum (0.5 nm step size) is shown in Figure

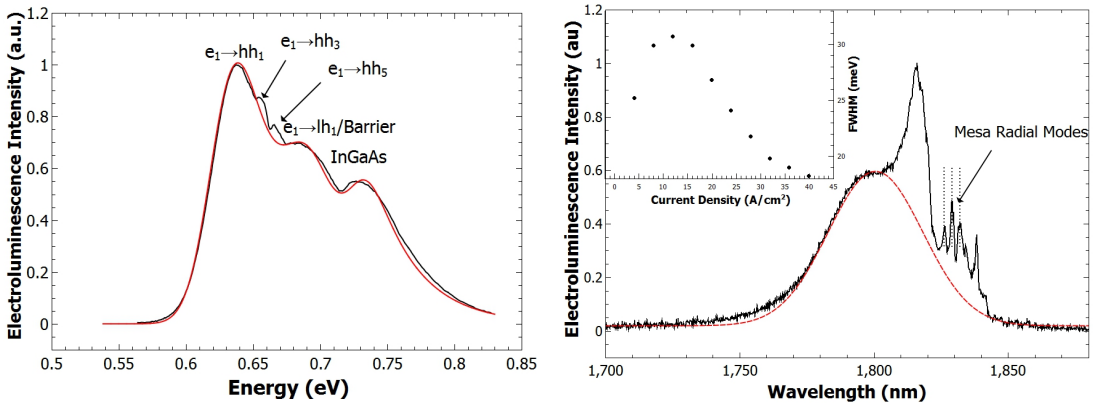

(a) (b)

Figure 6.14: (a) A graph of the electroluminescence spectra of the quantum dash sample at 300 K (Black line), the fitting of the spectra with the transitions for e_1–hh_1, e_1–lh_1/Barrier and bulk transition in the InGaAs barriers. (b) 50K surface electroluminescence of InAs Quantum dashes the main peak being spontaneous emission from the dashes and the longer wavelength peaks result from stimulated emission. Drive conditions were 140 Acm^{-2} with 5% duty cycle and 0.05 mm slits. Inset shows line narrowing with increasing current.

6.14b. The main peak, as detailed by the red dashed line, is attributed to spontaneous emission (e_1–h_1) from the InAs. This is consistent with simulations of 4 nm high dashes. The longer wavelength peaks are attributed to stimulated emission due to their narrow linewidth and lack of strong absorption peaks at this wavelength. The lasing occurs at temperatures up to 150 K. The source of the lasing peaks could not be determined and is beyond the scope of this investigation. Radial and whispering gallery modes have been considered as the origin of the smaller peaks. Using the following equations[141];

$$\Delta\lambda_{WG} = \frac{\lambda^2}{2\pi Rn} \tag{6.5}$$

$$\Delta\lambda_{R} = \frac{\lambda^2}{2Rn} \tag{6.6}$$

where $\Delta\lambda_{WG}$ is the whispering gallery mode spacing, $\Delta\lambda_R$ is the radial mode spacing λ is the wavelength, R is the radius and n is the refractive index. The radius of the mesa

is 400 μm, this would result in a radial mode spacing of 1.1 nm, smaller than the 3-4nm spacing seen in Figure 6.14b. The measured mode spacing would indicate a radius of 150 μm which is approximately the radius of the bond pad. This could indicate a current crowding issue. It is not possible to ascertain the presence of whispering gallery modes as the spacing is below the resolution of the system.

Temperature varied measurements were taken from 4 K to 300 K which resulted in a factor of 7 decrease in sub-threshold output intensity. The spontaneous emission from individual spectra were integrated and plotted against 1/kT (Figure 6.15a). This was fitted using the Arrhenius function (equation 6.1). The resultant activation energies were 109 meV and 33 meV. Given the value of 2.5 in the Z number analysis indicated the dominance of Auger recombination at lower temperatures, the activation energies of the common processes IVBA, CHCC and CHSH were calculated using the equations outlined in Section 2.7.3. The results indicated that the likely process responsible for thermal quenching was CHCC with a calculated activation energy of 31 meV. The 109 meV process was attributed to the thermal excitation of electrons out of the dashes, as simulations indicate the confinement energy to be 94 meV. The Arrhenius fitting suggests that the thermal loss of confinement is the dominant process of the two by a factor of 9.

The L/I turnover point, indicates the point of maximum efficiency. When viewed as a function of temperature it can give an indication of the location of defect states within the band gap[142]. The internal efficiency (η_{int}) of a sample can be given as[13];

$$\eta_{int} = \frac{R_r}{R_r + R_{nr}} \tag{6.7}$$

where the radiative rate $R_r = Bn^2 \propto L$ (the output intensity) and the total recombination rate $R_r + R_{nr} = An + Bn^2 + Cn^3 \propto I$ where A, B and C are the Shockley-Read-Hall, Radiative and Auger coefficients respectively and I is the injected current. The turnover

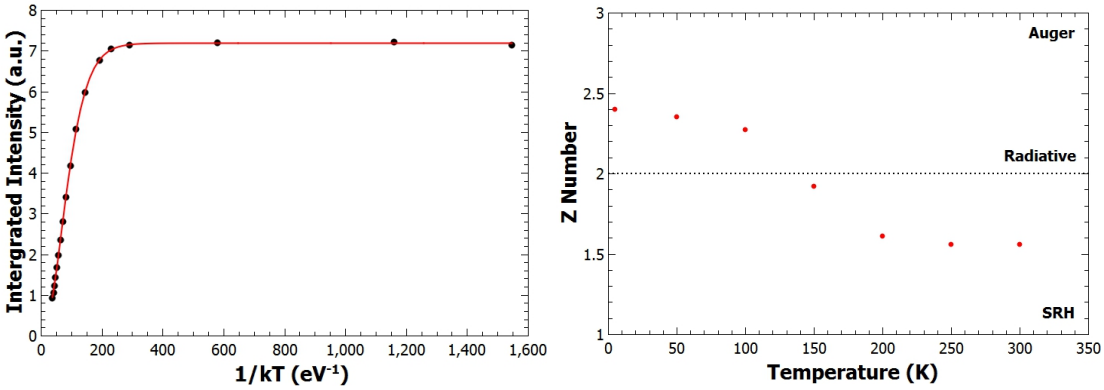

(a) (b)

Figure 6.15: (a) Arrhenius plot of the integrated spontaneous emission of the quantum dash LED. The fitting indicates activation energies of 109 meV and 33 meV. (b) The temperature dependence of Z number indicating an increase single carrier mechanism at increasing temperature.

point occurs when a maxima of equation 6.7 occurs. In this case the differential of the internal efficiency as a function of carrier density should be zero, thus;

$$\frac{d}{dn}\left(\frac{Bn^2}{An+Bn^2+Cn^3}\right) = \frac{B(A-Cn^2)}{[A+n(B+Cn)]} = 0 \tag{6.8}$$

The only physically possible solution to this is when $A = Cn^2$. Therefore at peak efficiency it can be assumed that $\frac{A}{C} \propto n^2 = I$. Both SRH and Auger recombination rates are temperature dependent with[14];

$$A = \frac{1}{2\tau_0\left(1+\cosh\frac{E_{tr}-E_{fi}}{kT}\right)} \tag{6.9}$$

and

$$C \propto exp\left(-\frac{Ea}{kT}\right) \tag{6.10}$$

where $E_{tr} - E_{fi}$ is the difference in energy between the Fermi level and the trap states. Rearranging the solution to equation 6.8 gives $\frac{A}{C} = n^2 \propto I$. Thus the fitting for

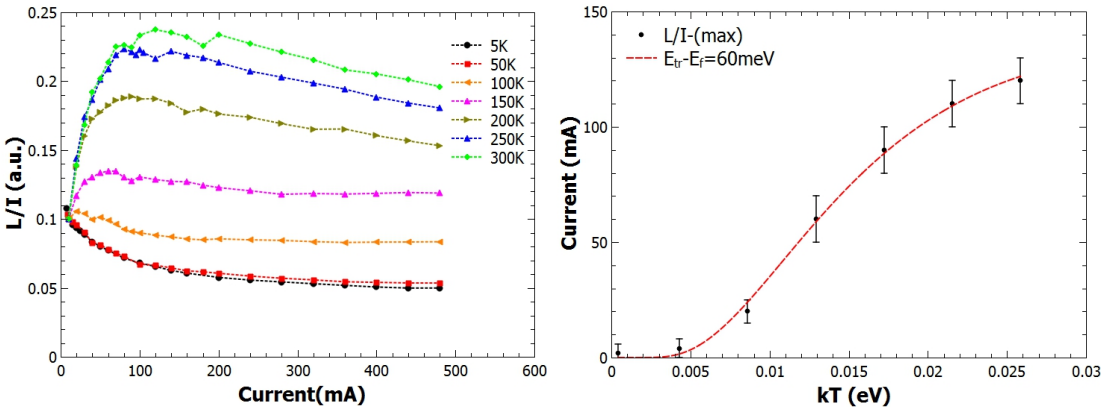

(a) (b)

Figure 6.16: (a) L/I curves for QDash LED at temperatures from 5 K to 300 K. (b) The temperature dependence of current at which internal efficiency is at a maxima from 4 K to 300 K, fit with Equation 6.11.

Figure 6.16b is achieved by combining equations 6.9 and 6.10 to give

$$\frac{A}{C}(T) \propto F_0 \frac{exp\left(\frac{E_a}{kT}\right)}{1+\cosh\frac{E_{tr}-E_{fi}}{kT}} \tag{6.11}$$

where F_0 is a fitting parameter and the value of E_a, the activation energy of the Auger process, is taken from those previously found in the Arrhenius fit as 33 meV. This provides a good fitting for Figure 6.16b with trap levels 60 meV from the intrinsic Fermi energy. This indicates that the trap levels are deep within the band, 120 meV from the band edge. This could be attributed to an As vacancy which has been measured with an energy of 140 meV [143].

6.4.4 Pressure Dependent Electroluminescence

To further ascertain the effect that Auger recombination had on the operating efficiency of the device, a sample was tested at the University of Surrey with Prof. S. Sweeney's group. The sample was placed in a pressure cell as described in [144] and subjected to pressures up to 400 MPa (4 kBar). Both spectra and light–current curves were recorded

at intervals between 400 MPa and atmospheric pressure.

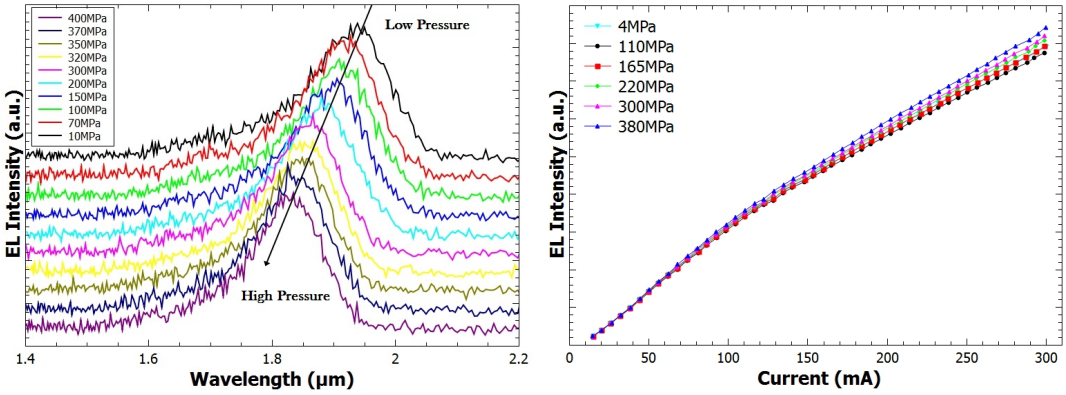

(a) (b)

Figure 6.17: (a) The electroluminescence spectra of a QDash LED when subjected to an increasing pressure and the resultant blue shift (as indicated by the arrow) of 9 meV/kBar. (b) Pressure dependent light current curve for QDash LED at 300 K showing a 9% increase in output. Uncertainty in data less than point size.

The energy shift shown in Figure 6.17a was calculated to be 9 meV/kBar which is consistent with previous high pressure measurements on InAs dashes, albeit with shorter wavelengths[145].

The relatively small increase in light intensity at high pressure validated the presence of the CHCC process. The application of pressure alters the bandgap (E_g). The relative change in $E_g - \Delta_{so}$ is far greater than the change in E_g, meaning the activation energies of IVBA and CHSH processes are more strongly dependant upon the pressure. The application of pressure resulted in a mere 9% increase in light emission which supports the view that the relevant Auger process is a CHCC recombination, but one which is not the dominant quenching process. Figure 6.18 also supports this view. The analysis involved ignores the effect of leaked carriers, the doubling of radiative efficiency does not correspond to the observed 9% increase indicating that carrier leakage has a greater effect on thermal quenching. An additional element that will contribute to the improved output at higher pressure is the improved carrier confinement. The pressure dependence of $In_{0.53}Ga_{0.47}As$ is 10.9 meV/kBar meaning electrons will have a further 7 meV

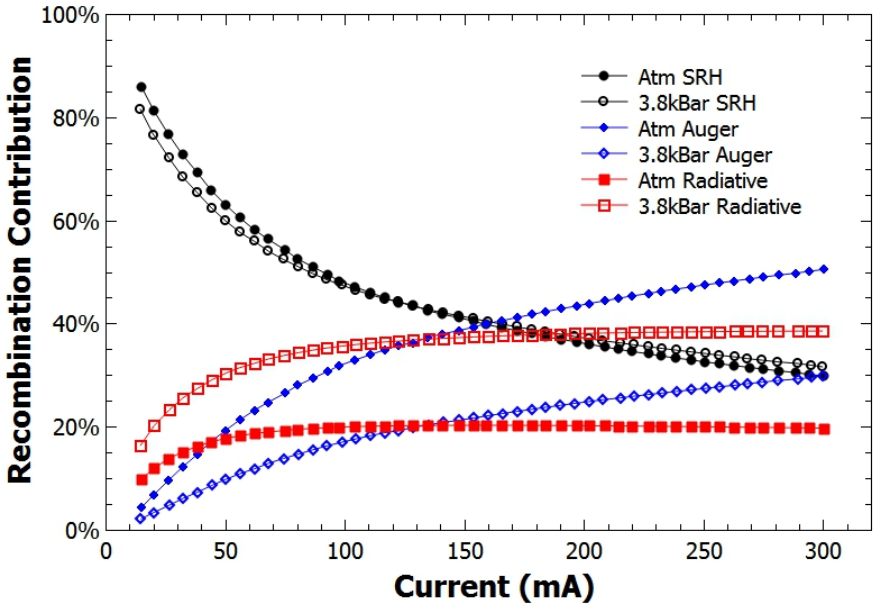

Figure 6.18: 300 K Recombination contribution of SRH, radiative and Auger recombination at atmospheric pressure and 3.8 kBar. Auger recommbination decreases by 40% and radiative increases by 100%.

of confinement at high pressure, compared to the 109 meV at atmospheric pressure.

6.4.5 Power and Efficiency

The output power of the device was measured at 300 K under qCW drive conditions with a current of 200 mA. The output power was 1.2 mW. This gives an external quantum efficiency of 0.94% and a wall plug efficiency of 0.7%.

6.4.6 Summary

With an output power density of 1.2 $mWmA^{-1}cm^{-2}$ the quantum dash LED compares well with the bulk sample, as the device is larger, the absolute power is greater. The wall plug efficiency is 5 times greater. The main limitation on improved output power is the thermal loss of electrons from the dashes; this could prove difficult to overcome as the InGaAs barrier region is selected due to the lattice matching between it and the

InP substrate. Studies of InAs quantum dash growth have also pointed to the necessity of using InGaAs for the growth of InAs dashes instead of quantum dots. Replacing InGaAs with lattice matched AlInAs, which would increase confinement, resulted in the formation of quantum dots. A lattice matched AlGaInAs epilayer has also been used to grown InAs dashes and merits further investigation[146]; not only to contribute to validating the theory that gallium is required in the epilayer to allow dash formation, it could also be used to determine the required quantity whilst also improving confinement. Furthermore, it could increase the confinement in the Quantum dashes improving room temperature operation.

In light of analysis on other samples further improvements to this sample will be discussed in Chapter 7.

6.5 InSb Quantum Dots

LEDs were produced using InSb quantum dots, a structure that has shown promise in achieving emission at 2 μm. Whilst there have been examples of InSb/GaSb quantum dots grown by various means such a LPE[83] and MOVPE[86], studies have been limited to the structural properties through Transmission Electron Microscopy (TEM) and Scanning Electron Microscopy (SEM), with optical studies via photoluminescence. A single example of electroliuminescence spectra, from a p-i-n junction containing InSb dots exists but no details are provided on its operation and is only used to confirm the transition energy seen in the PL. In this section the electroluminescence properties of InSb/GaSb quantum dots are examined. Both surface emitting mesa devices and edge-emitting devices were produced but processing of the mesa devices failed.

6.5.1 Growth

The sample (QH326) was grown on a n-GaAs(100) substrate using MBE. Once the native oxide layer was disorbed, a 100 nm n-GaAs buffer layer was grown, onto which a n-GaSb layer 200 nm thick was deposited using the IMF growth technique. To counteract the inherent dislocations formed by the IMF, a defect filtering structure was grown next. This consisted of four alternating 10 nm $Al_{0.1}Ga_{0.9}Sb$ and 9 nm GaSb layers. Next, a 1.5 μm n-$Al_{0.33}Ga_{0.66}Sb$ cladding layer was grown with a 800 nm GaSb active region containing the QDs and topped with a p-$Al_{0.33}Ga_{0.66}Sb$ cladding layer. The QDs were formed by the deposition of 10 pairs of nominally 0.5 ML InSb and 2.5 ML GaSb layers at 425 ℃. This stack was repeated five times. Between each stack the substrate temperature was raised to 510 ℃ under Sb_2 overpressure and a 30 nm GaSb barrier layer added. Thus the QDs reported here are of the so called 'sub-monolayer' type. The device was capped with a 100 nm p-GaSb for contact bonding.

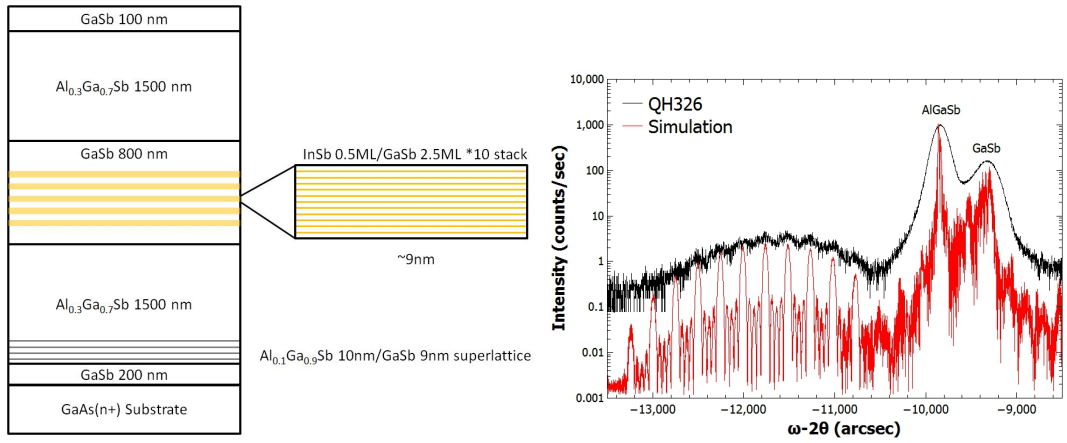

(a) (b)

Figure 6.19: (a) Schematic of (QH326) an InSb/GaSb quantum dot edge-emitting LED (ELED). (b) HRXRD of QH326 a alongside a normalised simulated fitting. The pendellösung fringes are consistent with a series of InGaSb quantum wells, suggesting that the InSb dots have diffused into the barriers.

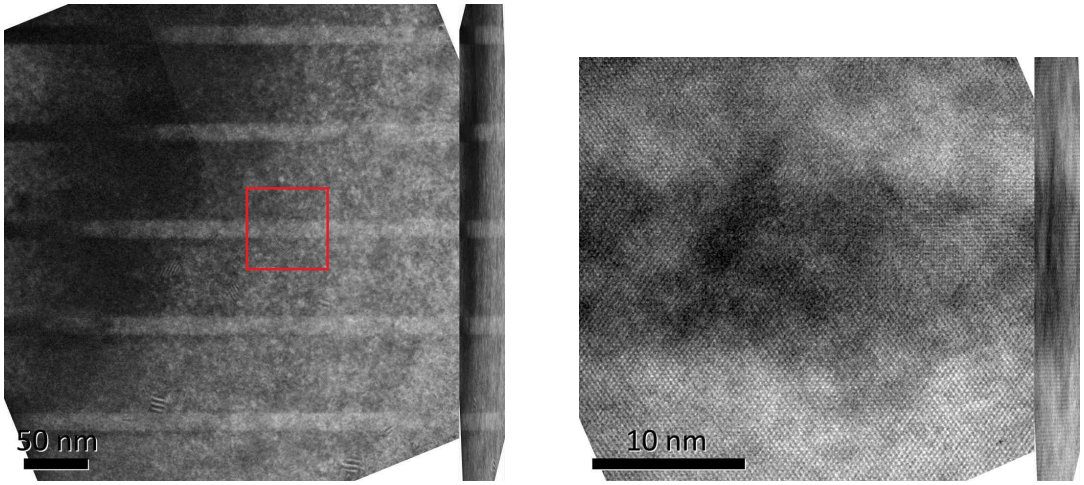

(a) (b)

Figure 6.20: (a) Bright field TEM image with ×50k magnification of the sub-monolayer Quantum dot region, the quantum dots appear to have diffused into the surrounding GaSb producing quantum wells around 15 nm wide. (b) Bright field TEM image with ×600k magnification of a single quantum well (red square in (a)). The indium within the well, as indicated by the darker regions, is not homogeneously distributed.

6.5.2 Structural Analysis

X-ray diffraction of the sample showed poor agreement with the proposed design. The pendellösung fringes were poorly resolved but their presence and position indicated a superlattice of InGaSb/GaSb quantum wells. The composition of the wells was approximately $Ga_{0.84}In_{0.16}Sb$ and 13-16 nm wide. Given the dimensions of the wells it is possible they have relaxed and fittings with unstrained wells provided equally good agreement. The composition is consistent with the ratios of GaSb and InSb deposited, though it is thicker than the 9 nm total thickness of each InSb/GaSb quantum dot stack as designed (Figure 6.19a). TEM images of the sample were taken by Dr Richard Beanland at Warwick University. These were used to determine the structure and ascertain if there are any quantum dots in the sample. The strain filtering AlGaSb/GaSb superlattice reduced the threading dislocation density from 2.5×10^9 to 4×10^8.

Figure 6.20a shows the region in the sample where quantum dots were expected.

The 10 layers of 0.5 ML InSb stack appears to be 15 nm thick instead of the expected 9 nm. There also is no evidence of quantum dots, which appear to have been replaced with quantum wells. At ×600k magnification, as in Figure 6.20b, the bright field TEM indicates regions which are indium rich but overall are best described as disordered quantum wells with indium rich regions rather than quantum dots.

6.5.3 Modelling

Simulations using nextnano® were undertaken and compared to the spontaneous emission peaks of the electroluminescence spectra from 10 K to 300 K. Five scenarios were simulated:

1. InSb quantum dots 1 monolayer (ML) thick.
2. InSb quantum dots 2 MLs thick.
3. 9 nm $Ga_{0.84}In_{0.16}Sb$ quantum wells.
4. 15 nm $Ga_{0.84}In_{0.16}Sb$ quantum wells.
5. 15 nm $Ga_{0.89}In_{0.11}Sb$ quantum wells with indium modulation.

The first two scenarios would be the result from the designed composition. Scenario 3 would be the result of the shuttering for the InSb and GaSb layers for the quantum dots, acting as a digital alloy type growth, whilst maintaining the expected layer thickness. Scenarios 4 and 5 are consistent with the TEM images. Scenario 4 is the resultant composition when a homogeneous alloy has been formed from the InSb and GaSb to the dimensions determined from the TEM images. Scenario 5 most closely approximates the composition seen in the TEM; 15 nm quantum wells with indium rich regions. The composition of the wells and indium rich and deficient regions were varied to find a good fitting of the emission spectra. Without knowledge of the exact composition of the quantum dot/well regions, which could be acquired through techniques such as

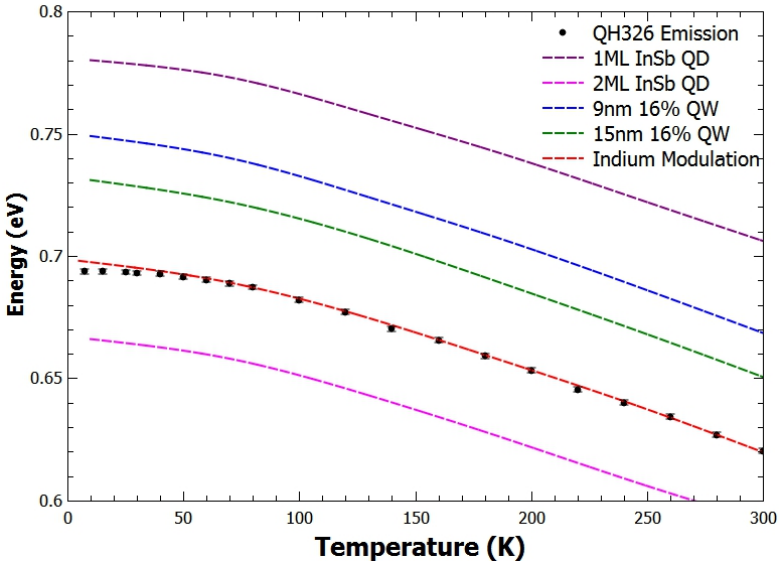

Figure 6.21: The emission energy of QH326 compared with the simulated possible solutions, the strongest agreement is found in the modelling of InGaSb quantum wells with indium rich regions. Varshni parameters of the LED are α=0.37 meV/K and β=130 K.

atom probe microscopy, as such the simulations have been adjusted to the results and cannot be compared to a known structure. A periodic arrangement of quantum dots was chosen for simulation as it best represents the modulation in the TEM images. Other possible solutions included triangular wells to simulate the diffused nature of the indium content and single larger indium rich regions. Whilst varying parameters such as indium content, region dimensions and in the case of triangular wells composition gradient could achieve similar transition energies as those seen. The periodic wells provided confinements consistent with the activation energies measured.

The resultant transition energies from the simulations are compared in Figure 6.21. Scenario 5 is the most consistent with experimental data. In this scenario, the dimensions were taken from the TEM images and the quantum wells were assumed to have indium rich regions. It is believed that formation of disordered GaInSb quantum wells instead of InSb quantum dots is due to a combination of the sub-monolayer growth method acting in a similar fashion to a digital alloy, along with the diffusion of the indium beyond this

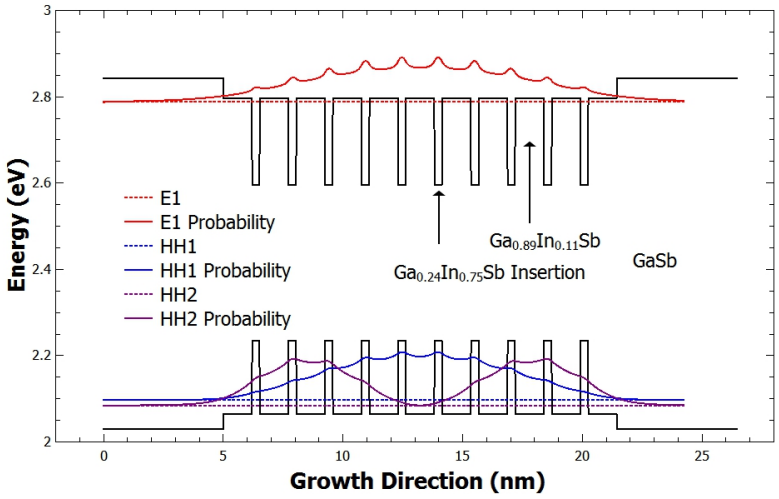

Figure 6.22: Band structure of QH326 at 300 K included are the energy levels and wavefunctions of the ee_1, hh_1 and hh_2 eigenstates.

region. The bright field TEM image indicates that this diffusion is not homogeneous as there is some modulation in the indium composition of the wells. This is a similar effect as to what is seen in the case of InAs/GaAs sub monolayer quantum dot growth [90]. This would explain why the simulation deviates from the experimental measurements at low temperatures. The indium rich regions will have a smaller band gap and at low temperatures, carriers will become localised. The 5 K band diagram can be seen in Figure 6.22; from this it is notable that the electron has very little confinement within the localised indium regions. If this description of the structure is accurate it would indicate that emission from the indium rich rich regions is unlikely at anything but the lowest temperatures. The compositions in this simulation include indium rich regions 1 ML thick with a composition of $In_{0.9}Ga_{0.1}Sb$ separated by 4 ML of $Ga_{0.88}In_{0.12}Sb$, with a total thickness of 16 nm. This would indicate growth rates double those expected.

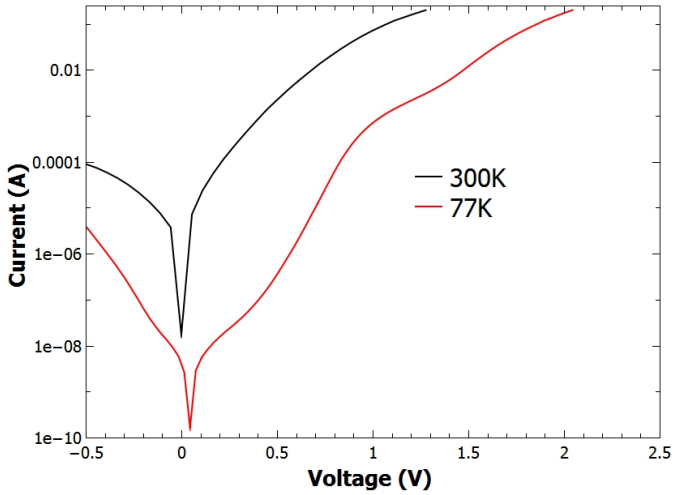

Figure 6.23: Current – voltage relation for QH326 LED at 77 K and 300 K.The ideality factor was 3.3 at 300 K and 4.3 at 77 K.

6.5.4 Current – Voltage Characteristics

Current - voltage measurements of the sample at 300 K indicate a low series resistance of 2.3 Ω, the parallel resistance is also low at 14 kΩ, indicating a lot a defect states or surface recombination. At 77 K the series resistance is 1.6 Ω and parallel resistance is 2 MΩ. Due to the stripe geometry of the sample it is not possible to determine if the leakage current is due to defect states or surface recombination. The ideality factor was 3.3 at 300 K and 4.3 at 77 K.

6.5.5 Electroluminescence

The device was mounted on a TO-46 header and placed in the Oxford Instruments OptistatDry cryostat such that the edge emission parallel to the ridge was aimed at the collection optics.

The sample was cooled to 4 K and driven qCW at currents from 21 mA to 200 mA. The measured spectra are shown in Figure 6.24a, the inset shows the device lases at a current density of 200 A/cm^2. A series of spectra were taken as the sample was warmed

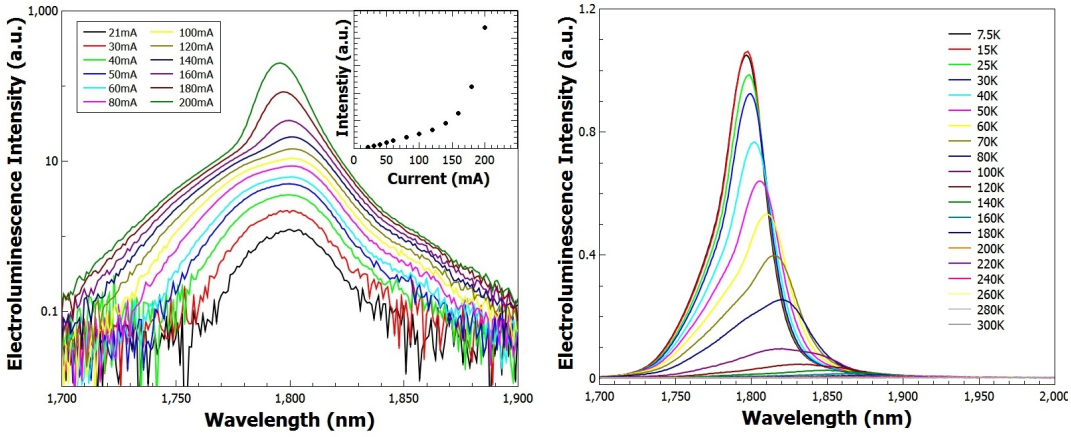

(a) (b)

Figure 6.24: (a) 4 K EL spectra of InSb SML QD ELED with inset intensity graph showing the device begin to lase. (b) Electroluminescence spectra from 7 K to 300 K at a sub-threshold current of 140 A/cm^2.

to 300 K; this was done at a sub-threshold drive current of 140 A/cm^2. The activation energies of the quenching processes indicated values of 49 meV and 9 meV (Figure 6.25a).As it is approximately the localisation energy seen in the Varshni fitting (5 meV), the low energy process is assigned to the electron escaping the indium localisation into the quantum well. However, this is approximately 1000 times weaker than the 49 meV process. The 49 meV process is believed to be the loss of confinement of the electron to the GaSb barrier, as the simulation in Figure 6.22 indicates a confinement of 53 meV. This difference is attributed to the inhomogeneous nature of the indium rich regions meaning the confinements vary region by region. The CHCC process also has an activation energy of 55 meV but this is not considered the main loss mechanism because as outlined in the following section the dominant process is a single carrier process.

The Varshni parameters are α=0.37 meV/K and β=130 K, which assuming a linear relation between GaSb and InSb would be consistent with $Ga_{0.9}In_{0.1}Sb$ (α=0.38 meV/K and β=133 K). The material between the indium rich regions in the simulation.

Lasing in the device occurs at temperatures up to 200 K (Figure 6.25b). Using the

equation[147];

$$J_{th} = J_0 \exp\left(\frac{T}{T_0}\right) \tag{6.12}$$

where J_{th} is the threshold current density, T is temperature and T_0 is the characteristic temperature. In QH326 T_0 is found to be 148 K.

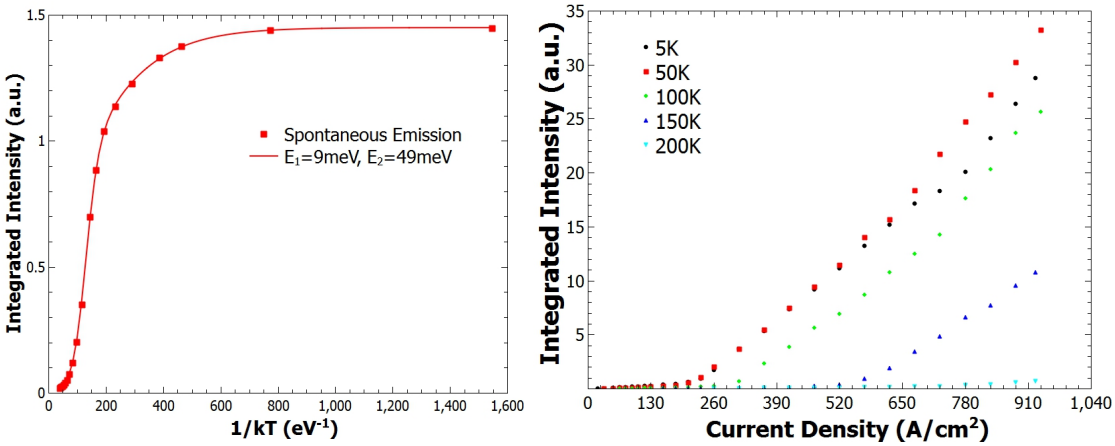

(a) (b)

Figure 6.25: (a) Arrhenius plot of QH326 light emission, giving activation energies of 9 meV and 49 meV.(b) I–L plots of QH326 from 5 K to 200 K. The resultant threshold currents indicate a T_0 of 148 K.

Figure 6.26a shows the analysis of the recombination processes at 300 K. This shows that the dominant recombination process is SRH. The likely cause of this is defects related to the IMF interface, as the defect filters have not entirely removed the threading dislocations as evidenced by the TEM images. This is consistent with the Z number analysis at 5 K which is 1.6, indicating a large defect density. By 150 K, it reaches 1.1 and doesn't increase.

Power varied measurements of the device are shown in Figure 6.26b, in the inset the FWHM is given as a function of injection current. From this it is possible to see that for low injection currents the FWHM is smaller than kT; at 40 mA the FWHM is 17 meV, less than the thermal broadening expected in a quantum well. This gives

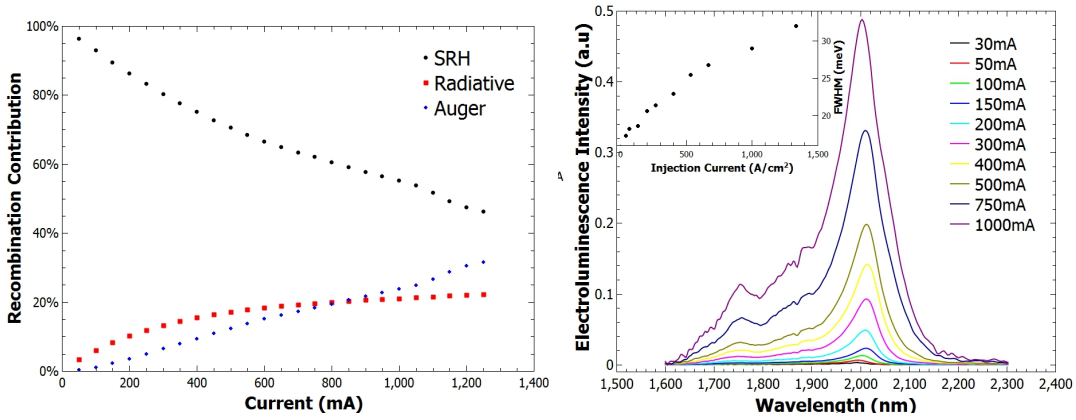

(a) (b)

Figure 6.26: (a) Recombination processes of QH326 LED at 300 K with a 1% duty cycle. (b) 300 K electroluminescence of QH326 ELED the main peak is attributed to the ee_1-hh_1 transition, the FWHM of which is included in the inset. The peak at 1750 nm is attributed to transitions in the GaSb barriers.

credence to the presence of indium rich quantum dots within the active region in which carriers are at least partially confined up to room temperature. The limited presence of the GaSb transition in the spectra is attributed to the threading defects inherent in a sample grown on IMF. Defects within the GaSb barriers reduce recombination in these regions. The localisations caused by the indium rich regions could attract carriers within the quantum well to defect free quantum dots. This process was also seen in the development of InGaN QW LEDs on sapphire substrates[148].

6.5.6 Power and Efficiency

At a qCW current of 200 mA at 300 K the output power of the device was measured to be 1.8 μW. This gives an external quantum efficiency of 1.5×10^{-3}% and a wall plug efficiency 7×10^{-4}%. At these drive conditions there was already evidence of Joule heating, meaning that without some form of heat sink, this would not be a practical operating mode for this device. Edge emitting devices result in a very high output power density (brightness) due to the very small emitting area. In this device the brightness is 18 $mWmA^{-1}cm^{-2}$,

an order of magnitude greater than that seen in the brightest surface emitting device in the study.

6.5.7 Inclusion of AlGaSb Barriers

With the loss of carrier confinement identified as a contributing factor in the thermal quenching of the previous LED, the growth was repeated using AlGaSb barriers as shown in the schematic in Figure 6.27a.

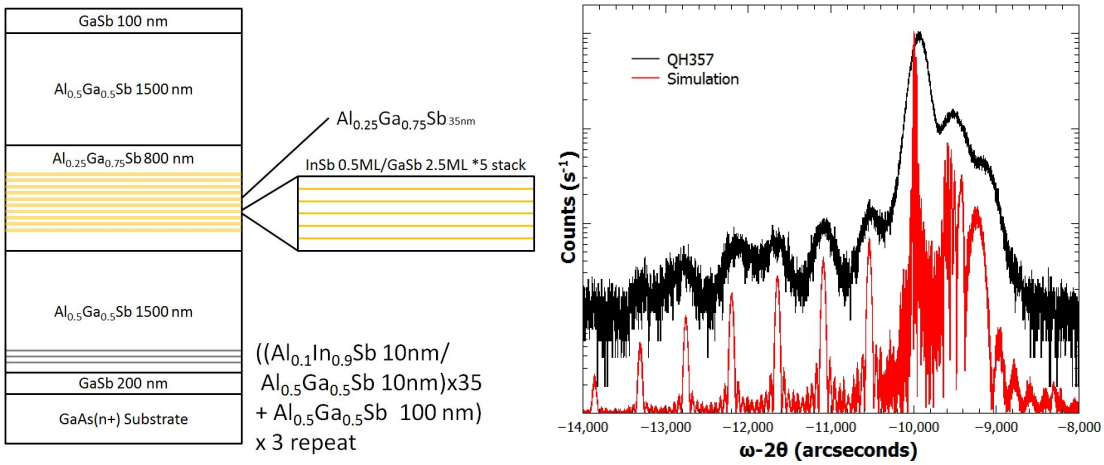

(a) (b)

Figure 6.27: (a) Structure of QH357 including a AlInSb/AlGaSb defect filtering layer. (b) $\omega - 2\theta$ x-ray diffraction of QH357. The pendellösung fringes are poorly defined but consistent with 6 nm $Ga_{0.82}In_{0.18}Sb$ quantum wells separated by 27 nm of $Al_{0.22}Ga_{0.78}Sb$.

Growth

Growth conditions during the InSb sub-monolayer deposition were kept identical to QH326 except each stack only contained five InSb depositions. The reduction in InSb depositions in each stack was reduced as simulations indicated a large number of confined states which could result in poor carrier confinement. Ten repeats of the quantum dot stacks were inter-spaced with 35 nm of $Al_{0.25}Ga_{0.75}Sb$ barriers. These barriers were grown at 500 °C. The ramp in temperature between the growth of quantum dot stacks and

AlGaSb barriers was achieved with a growth interrupt under antimony flux. The defect filter layers in this design consisted of a 35 period superlattice of 10 nm of $Al_{0.1}In_{0.9}Sb$ and $Al_{0.5}Ga_{0.5}Sb$. This superlattice was repeated three times, each one separated by 100 nm of $Al_{0.5}Ga_{0.5}Sb$.

Structural Analysis

X-ray diffraction scan of the wafer is shown in Figure 6.27b. The three main peaks are, from left to right; $Al_{0.5}Ga_{0.5}Sb$, $Al_{0.25}Ga_{0.75}Sb$ and GaSb. The pendellösung fringes are poorly defined but consistent with (6±1)nm $Ga_{0.82}In_{0.18}Sb$ quantum wells separated by 27 nm of $Al_{0.22}Ga_{0.78}Sb$. As in QH326, there is again evidence of intermixing of the InSb and GaSb stacks, though the introduction of AlGaSb barriers appears to have reduced further migration of the indium, as the fitting more closely resembling the intended growth, specifically the well width.

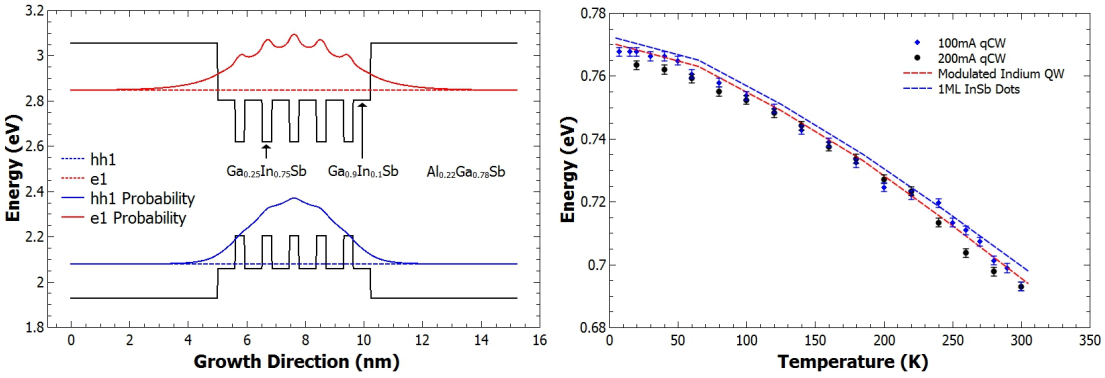

(a) (b)

Figure 6.28: (a) nextnano® simulation of QH357, electrons are confined within a GaInSb quantum well, the holes are confined within the indium rich regions. (b) Comparison of the peak energy of electroluminescence between 10 K and 300 K for QH357 with drive currents of 100 mA and 200 mA. These are compared to the modelled peak energies of an indium modulated quantum well and pure 1 ML InSb quantum dots.

Modelling

A nextnano® simulation of the band alignment and eigenstates of the carriers was undertaken using the x-ray fitting as a template for the structure and iterating until agreement was made with the observed emission from the LED. The resulting band structure is shown in Figure 6.28a. This band structure is the result of 1 ML $Ga_{0.25}In_{0.75}Sb$ dots within 2 ML $Ga_{0.90}In_{0.10}Sb$ barriers. The temperature dependence of the simulated ee_1-hh_1 transition is included in Figure 6.28b. For reference, also included is the transition energies of a pure InSb quantum dot within a GaSb surrounded by AlGaSb barriers. Both simulations are in good agreement with the expected design, though the modulated indium concentration quantum well more closely resembles these data. This would indicate that, though there is still some intermixing within the sample, it is improved upon from QH326. The addition of AlGaSb is not believed to have resulted in the improved InSb dot formation but the growth of the barrier layers at a temperature 10 °C lower has reduced the intermixing of the quantum dots and GaSb. The increased potential due to the AlGaSb barriers and reduced indium content in the wells has resulted in an increased transition energy, which subsequently has lowered the wavelength of the LED.

Current – Voltage Characteristics

At 300 K the series resistance in QH357 is 3.1 Ω which is greater than that of QH326. The shunt resistance is 148 kΩ, an increase of a factor of 10 compared to QH326, indicating a decrease in the number of carriers bypassing the diode The ideality factor at 300 K is 6.5 indicating the continued presence of traps. At 77 K the kink in the curve indicates a strong influence from a shunt resistance which is 45 MΩ, the series resistance is also very high at 6.25 Ω.

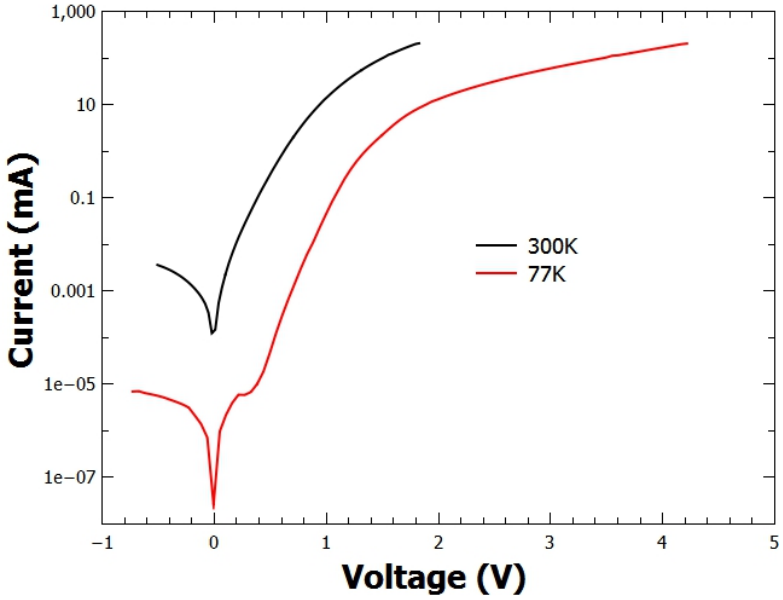

Figure 6.29: Current – voltage relation of QH357 at 77 K and 300 K. The ideality factor is 79 at 77 K and 6.5 at 300 K. In the 77 K there is strong evidence of a parallel resistance at low currents.

Electroluminescence

As with QH326, QH357 was processed into ELEDs with the same profile as QH326. The length of this device was approximately 1500μm. This was mounted on a TO-46 header and placed in the Oxford Instruments OptistatDry cryostat such that the edge emission parallel to the ridge was aimed at the collection optics. The introduction of AlGaSb barriers greatly improved the thermal quenching of the sample. The light intensity of QH326 decreased by a factor of 140 between 5 K and 300 K. Over the same temperature scale QH357 decreased in intensity by a factor of only 14, a tenfold improvement (Figure 6.30a). The Arrhenius plot, of the integrated emission intensity indicates activation energies for the quenching processes to be 71 meV and 15 meV, with the former's contribution twenty times greater (Figure 6.30b). The 71 meV process is attributed to the CHCC process which is calculated to have an activation energy of 69 meV. IVBA and the CHSH processes are suppressed as $\Delta_{SO} > E_g$ (Δ_{SO}=807 meV). The 15 meV process

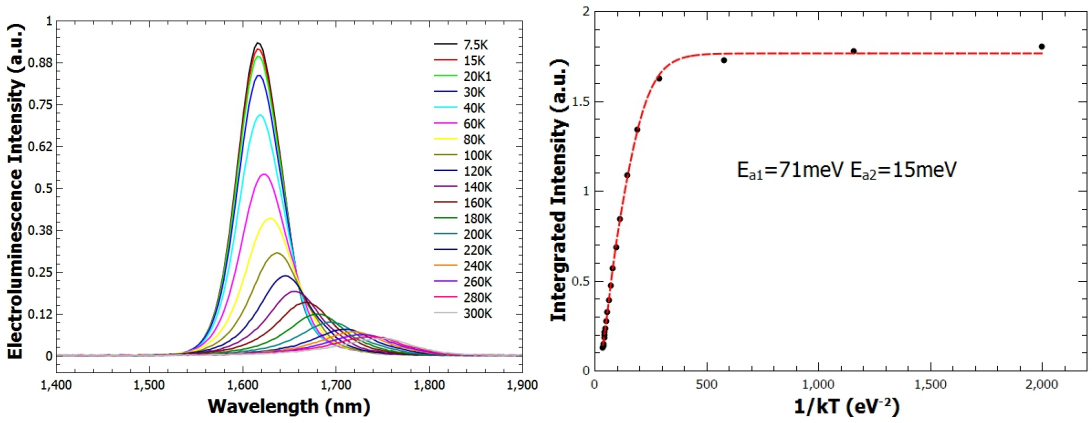

(a) (b)

Figure 6.30: (a) Electroluminescence spectra of QH357 at temperatures of 7.5 K to 300 K supplied with a current density of 130 A/cm^2 and 50% duty cycle. (b) Arrhenius plot of QH357 giving activation energies of 71 meV and 15 meV.

has been identified as the thermal excitation of the heavy hole out of the valence band minima of the InSb rich regions of the quantum wells.

The 300 K electroluminescence spectra is shown in Figure 6.31a. The FWHM as seen in the inset is greater than that seen in QH326 at comparable injection current densities. Close examination of the spectra indicates a second peak on the high energy side of the the main transition.The origin of this peak has not been determined.

Z analysis of the sample at 300 K gave a result of 1.3, indicating a strong dependence on a SRH recombination though an improvement upon that seen in QH326. This is supported by analysis using Equation 6.3, the results of which are shown in Figure 6.31b. This is similar to QH326 where SRH dominates at 300 K; this is likely caused by threading dislocations inherent in the IMF interface.

Power and Efficiency

The power output of the device was measured to be 0.042 mW at a drive current of 200 mA with a 50% duty cycle. This resulted in an external quantum efficiency of 0.03%

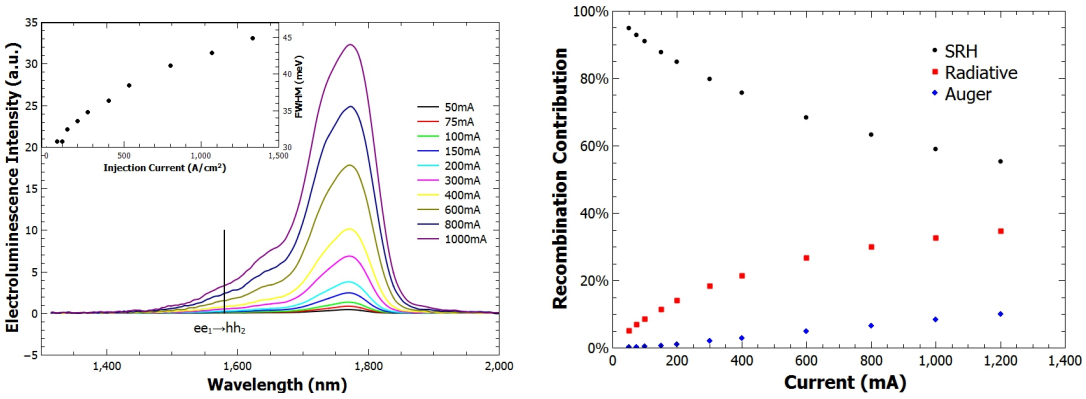

(a) (b)

Figure 6.31: (a) 300 K electroluminescence of QH357 ELED, a 1% duty cycle was used to reduce the effects of Joule heating. The main peak is attributed to the e_1-hh_1 transition and the location of the e_1-hh_2 transition is indicated on the graph. The inset shows the FWHM of the main peak. (b) Relative contribution of recombination processes in QH357 at 300 K.

and a wall plug efficiency of 0.012%, almost double that seen in QH326 where GaSb barriers were used. The corresponding brightness of the device is 420 $mWmA^{-1}cm^{-2}$, over 20 times brighter than the emission seen in the GaSb barrier device.

6.5.8 Growth on GaSb

Analysis of the previous two quantum dot samples has indicated a strong SRH recombination contribution. This is likely a consequence of the use of an IMF interface to allow the growth of the devices on GaAs. In an effort to reduce the effect of this, a sample was grown to the same design as QH357 but produced on a n-type GaSb(100) substrate. Because of this the IMF layer was unnecessary and excluded.

Structural Analysis

The x-ray diffraction spectrum for the resultant wafer (QJ559) is shown in Figure 6.32b. The bulk layers of GaSb, $Al_{0.25}Ga_{0.75}Sb$ and $Al_{0.5}Ga_{0.5}Sb$ are all more clearly defined in this sample. The pendellösung fringes in this case are more consistent with the

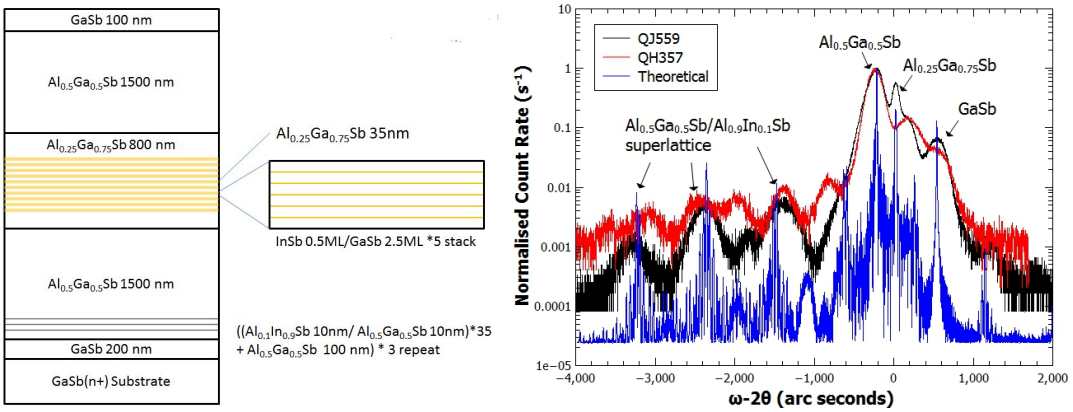

(a) (b)

Figure 6.32: (a) Structure of QJ559 a repeat of QH357 grown on n-type GaSb(100) substrate. (b) $\omega - 2\theta$ x-ray diffraction of QJ559, the pendellösung fringes are consistent with the $Al_{0.9}In_{0.1}Sb/Ga_{0.5}Al_{0.5}Sb$ superlattice. For reference the spectrum of QH357, nominally the same design on GaAs and the simulated pattern are included.

$Al_{0.9}In_{0.1}Sb/Ga_{0.5}Al_{0.5}Sb$ superlattice than the GaInSb quantum wells seen in previous samples. Given their depth within the sample and relative broadness of the peak it is possible that the GaInSb quantum wells are still present.

Current – Voltage Characteristics

The current - voltage plot of the QJ559 LED is shown in Figure 6.33. There is evidence of a large amount of sub-threshold activation indicating the presence of defects or surface states. This is supported by the low shunt resistance (R_P) of the diode at 670 Ω, the lowest amongst the devices studied in this work.

This is most comparable to QJ403, another sample grown on GaSb which also includes InGaSb and AlGaSb layers. Further study is required to determine if this is a product of the processing or is inherent within these materials.

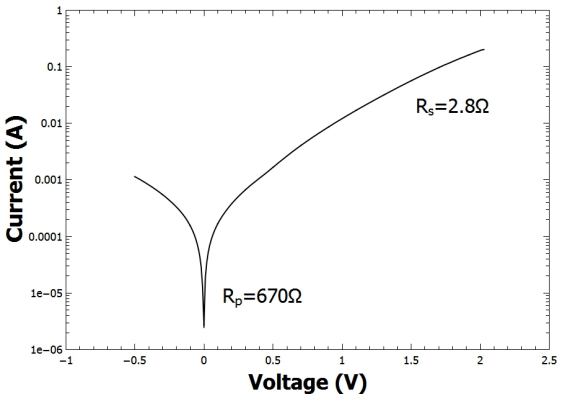

Figure 6.33: 300 K current - voltage plot of a 800 μm diameter LED made from QJ559, the ideality factor is 11

Electroluminecence

A device was placed in the Oxford Instruments OptistatDry cryostat such that the emission from the top of the mesa was directed at the collection optics.

The sample was cooled to 4 K and electroluminescence emission spectra were recorded at varying temperature intervals up to 300 K. As can be seen in Figure 6.34, the resultant spectra had two main peaks. The low energy peak is attributed to transitions between states confined within the quantum dots. This peak consists of two individual transitions, the dominant of which switches between 80 K and 100 K, possibly indicating the loss of confinement in the higher energy state. The shorter wavelength peak is attributed to a transition from the GaSb barrier.

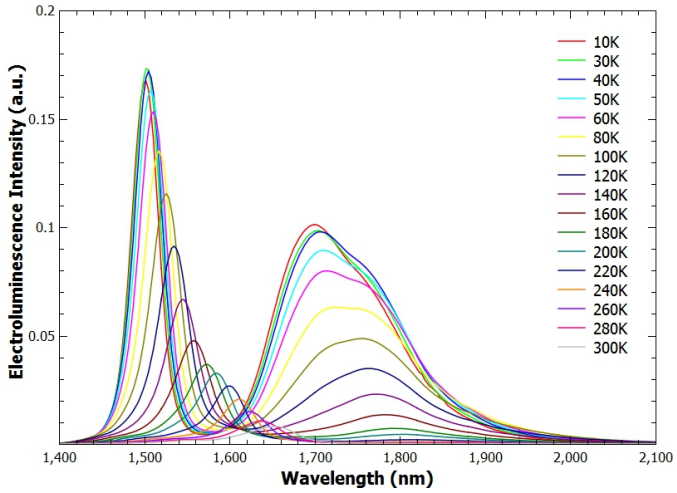

Figure 6.34: Electroluminescence spectra for QJ559 at temperatures from 10 K to 300 K. Emission from the shorter wavelength peak is attributed to a GaSb quantum well caused by the interlayering of AlGaSb and GaSb in the active region. The longer wavelength peak is composed of two peaks the dominant of which switches between 80 K and 100 K.

The presence of this second peak which is not seen in the previous samples despite a nominally identical active region is attributed to the calibration of growth rates on the MBE system. The growth rates used in the formation of SML quantum dots is very low, 0.09 ML/s in the case of QJ559. These rates are far below those that the system is typically calibrated to, the rate is inferred from an extrapolation of the cell temperatures at higher growth rates. Given the exponential relation of cell temperature and growth rate it is possible the growth rates in the two previous samples was incorrect. This would be consistent with the larger than expected dimensions of the stacks seen in the TEM of QH326. As QJ559 was grown some time later, growth times were recalculated to take into account the drift in rates as the material in the cell is depleted. It is possible that this rate was more accurate and deposited a sub monolayer quantity of InSb.

Figure 6.35a shows the simulated 300 K band structure of QJ559. Initial simulations repeating the structure of QH357 were adjusted until agreement was found with the emission spectra seen in Figure 6.34. The structure consisted of 2 ML thick $In_{0.7}Ga_{0.3}Sb$

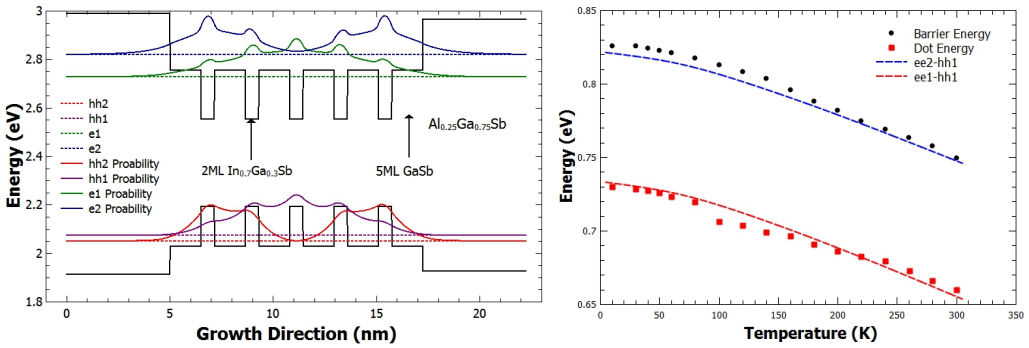

(a) (b)

Figure 6.35: (a) nextnano® simulation of a single quantum dot stack of QJ559 showing the lowest two energy eigenstates in each band. (b) Comparison of the e_1-hh_1 and e_2-hh_2 transitions predicted in the simulation with the measured peaks from the temperature varied electroluminescence.

quantum dots separated by 5 ML of GaSb and $Al_{0.25}Ga_{0.75}$ barriers. The temperature dependence of the transitions in this simulation is shown in Figure 6.35b as the dashed lines. Whilst not adequately simulating the emission from the quantum wells at low temperature, the simulation provides a good approximation and fits well with the quantum dot regions. Without TEM imagery of the quantum dot regions it is not possible to further determine the exact composition of the active region.

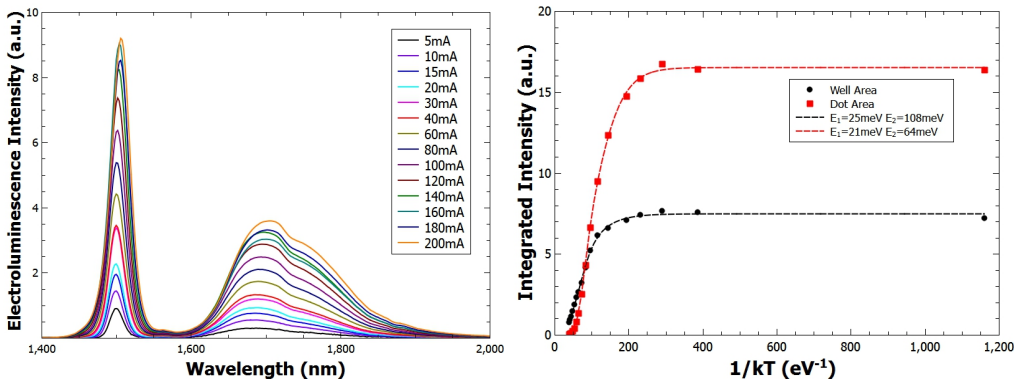

(a) (b)

Figure 6.36: (a) Electroluminescence spectra of QJ559 at 4 K with a 50% duty cycle. (b) Arrhenius fit of QJ559 with the dot emission and barrier emission measured separately.

The thermal quenching in the quantum dots is far greater than that in the wells. At 300 K there is no emission detected from the dots; between 10 K and 280 K it reduces by a factor of 280. The quantum well emission, by comparison, only reduces by a factor of 9 between 10 K and 300 K. Arrhenius plots of the integrated intensity of each peak (Figure 6.36b) reveal activation energies of 21 meV and 64 meV for the quantum well emission and 25 meV and 108 meV for the quantum dot emission. In the quantum dots the quenching is dominated by the 108 meV process. This corresponds to the excitation of the electron between the e_1 and e_2 states, which simulations indicate have a difference in energy of approximately 100 meV. The 25 meV process is the thermal leakage of the holes, as this has a simulated confinement energy of 26 meV. In the quantum well the quenching is attributed to the CHCC process with a calculated activation energy of 70 meV. The 21 meV process is consistent with transitions between hole states. The Varshni parameters of QJ559 are given in Table 6.2, both the InSb dots and GaSb wells are approximately similar to GaSb, given the small size of the dots then structure will be dominated by the GaSb. Z analysis of the power varied light intensity indicates a

	α (meV/K)	β (K)
Well	0.4	170
Dot	0.32	120
InSb	0.61	500
GaSb	0.37	94

Table 6.2: Varshni parameters of the quantum dots and wells in QJ559 compared to GaSb and InSb.

decrease from 2.3 at 5 K, to 1.9 at 300 K for the quantum well. This indicates a greater contribution from SRH as temperature increases but it remains a prominently radiative in recombination. The quantum dot Z number remains around 2 until the emission quenches. Whilst this sample's quenching means it is possible that it is the result of a large SRH and Auger contribution, given that the main quenching process is electron leakage it is more probable that it is a radiative dominated recombination.

Power and Efficiency

The power output of the device was measured to be 0.08 mW at a drive current of 200 mA with a 50% duty cycle. This resulted in an external quantum efficiency of 0.05% and a wall plug efficiency of 0.02%. This is the best output power and efficiency measured amongst the quantum dot samples. The power density was calculated to be 0.08 $mWmA^{-1}cm^{-2}$.

6.5.9 Comparison of Quantum Dot Samples

Whilst it has not been possible to conclusively determine the presence of InSb quantum dots within all samples, the evidence points to the inclusion of some dot like properties within the samples. The bright field TEM images of the first sample (QH326) show some modulation in the indium composition. This modulation, when simulated using nextnano® is consistent with the resulting transition energies. Atomic probe microscopy would resolve this issue. Although available resources didn't allow for it in this study, it would also be fruitful to investigate the formation of quantum dots in the GaSb substrate sample (QJ559) using TEM or atomic probe microscopy. The 10 K electroluminescence spectra in this instance shows the most definite evidence of InSb quantum dots within a quantum well (Figure 6.37a), with two distinct peaks seen. At room temperature the FWHM of emission spectra is below that expected by the thermal broadening of a quantum well peak. Whilst not conclusive proof of the presence of quantum dots, it could indicate the partial dot like confinement of the carriers. This can be seen in the simulated band diagrams by the increased probabilities of carriers being found in the indium rich regions. For this reason, the InSb in QH326 and QH357 should not be considered a quantum dot in the truest sense, a more appropriate name may be nanoscale InSb insertions. In contrast the InSb structures of QJ559 are consistent with quantum dots and as such are the first reported electroluminescence of SML InSb/GaSb quantum dots.

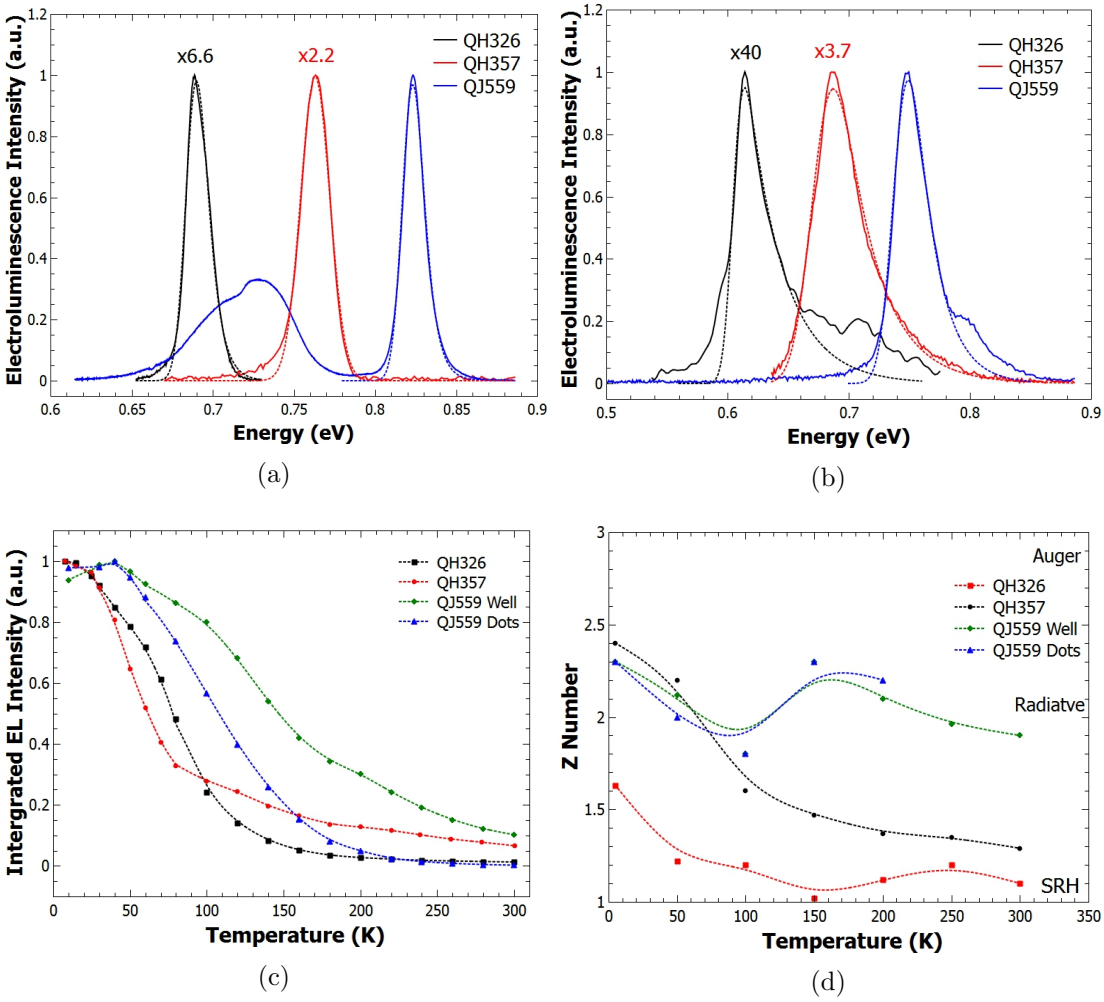

Figure 6.37: (a)10 K Electroluminescence spectra of the InSb quantum dot samples at current densities of 100 A/cm^2, each has been fitted with Equation 2.15. (b) 300 K Electroluminescence spectra of the InSb quantum dot samples at current densities of 200 A/cm^2. (c) The integrated intensities of the peaks seen in the InSb quantum dot samples normalised at 10 K. (d) Z number analysis of the peaks seen in the InSb quantum dot samples with trend lines in the corresponding colour to aid the eye.

QJ559 shows a double peak at 4 K (Figure 6.37a), whereas QH326 and QH357 show only a single peak, this is due to the lack of properly formed quantum dots instead merely InSb rich regions within a disordered quantum well. In QH326 the electrons are negligibly confined and in QH357 they are merely confined to the quantum wells.

Simulations indicate that the more defined dots in QJ559 bring superior confinement within the dot. TEM or atomic probe microscopy imagery of the active region of QJ559 would confirm the structure and validate this reasoning. A further route to improving confinement in the samples would be to increase the thickness of the GaSb deposition between InSb layers. As can be seen in the simulations of the samples (Figures 6.22, 6.28a and 6.35a), the wavefunction fully overlaps between these layers. By increasing the layer thickness such that the dots became isolated, simulations indicate the eigenstates would have a lower energy. Using equation 2.15 on the 4 K spectra of all three samples we see similar values of σ for the GaSb IMF (QH326) and the dot containing GaSb wells in QJ559 (5.6–5.7 meV) where as the AlGaSb/InGaSb containing QH357 is more similar to that seen in QJ410, the AlGaSb/InGaSb MQWs from the previous chapter, further suggesting that QH357 does not contain quantum dots but has in fact a disordered quantum well structure.

Figure 6.37c compares the thermal quenching of the peaks. The two samples on IMF (QH326 and QH357) quench at the lowest temperatures due to strong SRH recombination. The superior carrier confinement in QH357 results in a higher output at room temperature. The quantum dots in QJ559 quench the most relatively, indicative of the low confinement inherent in small quantum dots. The quantum wells in QJ559 by comparison quench by the lowest amount. The activation energies of QH357 and QJ559 quantum wells are very similar (15 meV & 71 meV and 21 meV & 64 meV, respectively). As both samples are nominally the same composition, this further highlights the possibility that QH357 is a quantum well sample. In Figure 6.37d, the difference between the QJ599 and QH357 can be seen. QH357 along with QH326, the two IMF samples, are dominated by SRH recombination which is to be expected from IMF samples. Within the quantum dots of QJ559 the main recombination remains radiative throughout, with quenching coming from the thermal leakage of carriers into the wells. For the wells themselves, the activation energies indicate CHCC recombination to be the contributing

recombination process. When taken in conjunction with the Z analysis, it appears that SRH is also increasing with temperature so counteracts the expected rise in Z number, but the sample is radiatively dominated throughout.

6.6 Summary

In summary, this chapter has analysed several LED material systems to provide the replacement of incandescent bulbs in enhanced flight vision systems.

Device	λ_{peak} (μm)	Output (mW)	Power Density (mW/mAcm^2)	EQE (%)	Wall Plug (%)	Limiting Factor
LED22 (Bulk)	2.25	0.5	1.5	0.43	0.14	Hole Leakage
Q-Dash	1.97	1.2	1.2	0.94	0.7	Electron Confinement
QJ403 (Q Well)	2.07	0.4 μW	4.7×10^{-4}	1.6×10^{-3}	1.6×10^{-4}	Electron Confinement
QH326 (dQW)	2.01	0.0018	18	1.45×10^{-3}	0.0007	SRH
QH357 (dQW)	1.81	0.042	410	0.031	0.012	SRH
QJ559 (SML QD)	1.66	0.08	0.08	0.05	0.02	CHCC(QW) e_1-e_2 (QD)
100W Incandescent Bulb	1	10.5W*	N/A	10.5	10.5	

Table 6.3: Various figures of merit for the samples measured in this chapter. dQW denotes disordered QW. *Output power of region InSb detector is sensitive.

In Table 6.3, the figures of merit for the devices are compared for these. The device with the greatest absolute power output and most efficient device was the InAs quantum dash sample with an output power of 1.2 mW. This sample like all the other homo-epitaxial samples were limited in part by the confinement of the carriers within the active regions. In the IMF samples despite the introduction of defect filtering layers, SRH recombination was still a strong source of limitation in the devices.

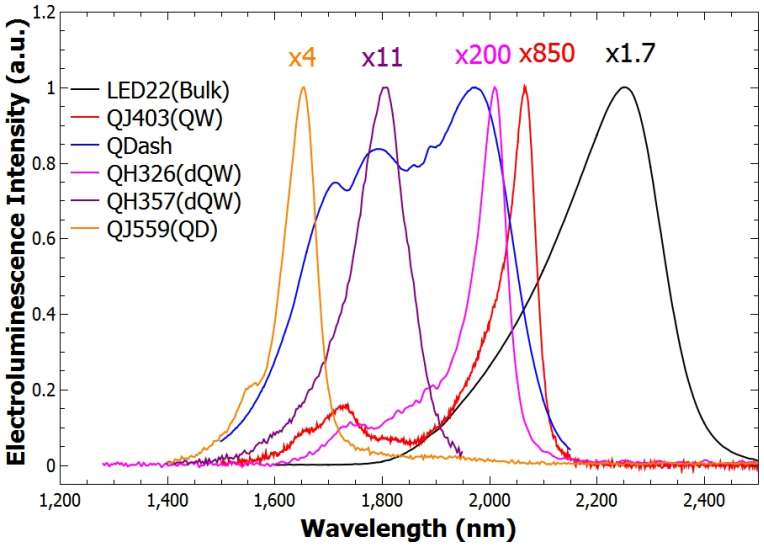

Figure 6.38: 300 K electroluinescence of each sample in this chapter, normalised to the quantum dash sample. Drive conditions in each case are 300 mA/cm^2 at 50% duty cycle.

The use of edge emitting devices would be adaptable to the current generation enhanced flight vision systems, the cross section of the emitting area is small resulting in a high brightness. The small cross section also allows a high density of devices within the lighting unit, up to the limit of waste heat extraction. Such lights are also highly directional which reduces the required power as the light can be more easily focused where it is needed.

The fabrication of another sample with similar composition to QJ559 or the quantum dash sample would be an excellent candidate for this further work. Taking the next logical step with edge emitting LEDs would be the operation of said devices as superluminescent diodes (SLEDs). Recent progress in superluminescent InGaAsSb/AlGaAsSb quantum well SLEDs have achieved output powers up to 40 mW at 2.05 μm [149] and great increase from the 10's of μW achieved from standard GaSb based LEDs[150, 151]. If such increases are possible in InP based InAs quantum dashes this could be a way to achieve the output power requirements to supplement visible LEDs in producing a runway light which is compatible with current generation EFVS.

The quantum dash sample had the greatest output power and again suffered from electron leakage from the dashes. Increasing the height of the dash would improve the confinement with the additional benefit of increasing the wavelength. Assuming additional InAs can be deposited without reverting to a 2D growth regime this would be the preferred method of developing the material as ΔE_c is already large (250 meV) and lowering the confined states within the well should be easily achieved. Simulations of this indicate wavelengths of 2.5 μm are achievable.

This chapter has also reported the first electroluminescence of SML InSb quantum dots grown on GaSb. Grown using the sub-monolayer deposition method, they have proven difficult to prevent from diffusing into the surrounding GaSb once they have been capped. QJ559 appears to of solved this issue, though the emission wavelength is below that desired for EFVS. Options to extend the wavelength are limited by the nature of SML quantum dots, they are inherently small. Moves to extend the wavelength could include increasing the amount of InSb deposited, though this is limited to the point when a well would be formed. The other possible solution is the alteration of the barrier regions. Indium could be deliberately added to the capping material, reducing the potential between dots, at the cost of confinement. Given the limit on QJ559 from carrier leakage this is to be avoided. The preferred method should be to increase the thickness of the capping layers such that the quantum dot electron wavefunctions become non interacting which simulations indicate will lower the transition energy. An adjustment of the active region width, by the removal of a InSb layer within the stack, would be beneficial to the design as it will decrease the well size and increase the e_1-e_2 separation. Another way to achieve this would be to reduce the aluminium content in the barriers such that additional electron states are not confined.

Chapter 7

Conclusions and Suggestions for Further Work

7.1 Summary of Achievements

This work examined the possible solutions to replace the 2 μm portion of an incandescent light source's spectrum. The following outlines the achievements of this work:

- InAs quantum dash containing structures were fabricated into LEDs which achieved an output power of 1.2 mW at 2 μm with a wallplug efficiency of 0.7%. This is greater than the 0.5 mW achieved by commercially available devices achieve at this wavelength.

- InSb quantum dots were grown on GaSb using the sub-monolayer growth technique. LEDs were fabricated with SML QDs in the active region, producing the first reported SML InSb QD electroluminescence. Due to the inherently small size of these quantum dots, carrier confinement was limited in the quantum dots, causing quenching at 250 K. The very low quantities of InSb deposited also made the material very sensitive to growth rate fluctuations.

- The suitability of $Ga_{(1-x)}In_xSb$ ($0.25 < x < 0.35$) quantum wells for 2 μm emission was examined and it was found that the main limitation was electron confinement within the quantum wells. This was improved upon the use of AlGaSb barriers and IMF on GaAs. This led to a twenty fold increase in room temperature photoluminescence intensity.

- A ternary IMF interface was achieved for the first time between GaAs and AlGaSb with a defect density of $<2\times10^{9}$cm^{-2} beyond the interface. A second IMF interface with no common element across the interface was achieved in the GaAs/InAlSb system with a defect density of 5×10^{10}cm^{-2} beyond the interface. This allows for greater freedom in the selection of relaxed lattice constant, useful in the engineering of strain within a structure.

7.2 GaInSb/(Al)GaSb Quantum Wells

GaInSb quantum wells were grown on both GaSb and GaAs. Those grown on GaAs utilised an IMF interface to relax the proceeding (Al)GaSb layer. This included the first reported ternary IMF interface with a period of 4 nm equal to 13 AlGaSb lattice spacings and 14 GaAs. TEM images indicated a defect density of $2\times10^{9}\text{cm}^{-2}$. TEM imagery also showed a large degree of variation in quantum well width within the sample. The use of a growth pause under antimony flux between each interface improved the quality of the InGaSb/AlGaSb samples. Samples that underwent this process exhibited a threefold increase in room temperature photoluminescence signal along with a 30% reduction in FWHM. The x-ray diffraction also showed a 40% reduction in FWHM and the pendellösung fringes became visible, indicating more evenly distributed strain.

Tentative steps to producing a ternary IMF between GaAs and InAlSb were taken. The GaInSb quantum wells in this instance exhibited superior abruptness than those grown on AlGaSb. TEM images showed that the first two quantum wells grown were poorly formed despite identical conditions to the following wells, this was not seen in any other IMF sample. TEM also indicated a dislocation density of $5\times10^{10}\text{cm}^{-2}$.

GaInSb/GaSb quantum wells were produced with compositions $\text{Ga}_{(1-x)}\text{In}_x\text{Sb}$ ($x < 0.4$) with well width varied between 3–12 nm and gave good agreement with the nextnano® simulations. At larger well widths interface abruptness degraded. The key quenching mechanism limiting these materials was poor confinement of carriers. This was improved upon by using AlGaSb barriers. LEDs using an AlGaSb IMF and barriers were not successful as electrons became trapped at the GaAs/AlGaSb interface.

7.2.1 Suggestions for Future Work

From the results above it is clear that the addition of aluminium to the barrier layers improved the high temperature performance of the GaInSb quantum wells. To improve

the quantum wells, the composition could be adjusted to include arsenic. This would reduce the strain and allow the well width to be increased. An increased well width would result in a reduced effect of the quantum confinement of the large potentials of the AlGaSb barriers. Additionally the widening of the quantum wells will improve the confinement of the carriers and allow smaller aluminium barriers to be used. Another possible avenue would be the growth prior to the IMF interface of a AlGaAs layer with the same Al:Ga ratio.

In the context of LEDs, a key improvement would be the bypassing of the IMF interface through the utilisation of top-top contacts. The interface between the GaSb contact layer and upper AlGaSb barrier layer should be graduated to reduce band bending and carrier blocking that occurs at this point. The introduction of strain filtering superlattices such as $Al_{(0.5)}Ga_{0.5}Sb/Al_{0.1}In_{0.9}Sb$ have reduced the defect densities in the InSb quantum dot samples by a factor of 10 and could be utilised in this case.

7.3 InAs Quantum Dashes

LED epilayers were produced at III-V Lab, Marcoussis, France and processed with assistance from the Centre for Nanoscience and Technology at the University of Sheffield. The active region consisted of six layers of InAs quantum dashes grown on InGaAs between InP cladding layers and grown on InP(100).

The resultant surface emitting device achieved the highest output power in this study. At 1.2 mW it is greater than comparable commercially available surface emitting devices. The device was limited by poor confinement of the carriers within the dashes; transitions between the ground state of the dashes and holes in barriers, and band to band transitions within the InGaAs barriers were both present in the 300 K spectra.

SRH recombination was the result of As vacancies within the crystal lattice with defect states 120 meV from the band edge. Activation energies indicated Auger recom-

bination and thermal excitation of electrons from the quantum dashes were the main sources of thermal quenching. Hydrostatic pressure measurements on the device undertaken at the University of Surrey with Prof. S. Sweeney's group identified the thermal excitation of carriers to be the main loss mechanism.

Stimulated emission was recorded in these devices at temperatures up to 150 K. The cause of this emission was attributed to radial modes beneath the contact pad, possibly due to current crowding.

7.3.1 Suggestions for Further Work

As the structure had been designed for edge emission, thick cladding layers on the top may have resulted in an unwanted increase in scattering and re-absorption. Thinning this layer would improve the output. Conversely if the current design is kept, the device could be developed into a superluminescent LED (SLED). This could be achieved by producing an edge emitting LED strip with either a diagonal contact or one which is spoiled at the ends to reduce gain and spoil resonance. If improvements seen between GaInAsSb quantum well LEDs and SLEDs are replicated in InAs quantum dashes it is possible an output in the range of 80 mW could be achieved[149].

As electron confinement was identified as a key loss mechanism within the LED, improvement of the confinement should be achieved by increasing the height of the dashes. The conduction band offset between InAs/GaInAs is 250 meV so lowering the eigenstate lower in the potential well is preferred. This would have the added benefit of extending the wavelength of emission.

As the quantum dashes are a relatively new structure about which the growth mechanisms are not fully understood, further investigation of the morphology of quantum dashes on different matrices merits investigation. The necessity of using InGaAs has been determined but the introduction of aluminium could improve confinement and band alignment. Growth of dashes on AlGaInAs would allow the gallium content to be

varied whilst retaining the lattice matching to InP, thus a study of the morphology of the dashes could be undertaken.

7.4 InSb Sub-Monolayer Quantum Dots

InSb quantum dots were grown on GaSb using the sub-monolayer growth technique and devices containing these structures were fabricated into LEDs. Due to the inherently small nature of sub-monolayer (SML) quantum dots, electron confinement within the dots was small. This resulted in quenching of the emission from the quantum dots at 250 K. This is the first electroluminescence reported from SML quantum dots. At room temperature, emission is the result of recombination within the GaSb quantum wells with a wavelength of 1.65 μm and output power of 80 μW.

Edge emitting LEDs were also produced using sub-monolayer growth, these samples were grown on GaAs utilising an IMF interface. Analysis of these samples indicate that the growth of InSb dots did not occur and the resultant structure was more akin to a disordered GaInSb quantum well. This was attributed to the calibration of growth rates with low cell temperatures. The growth rates during InSb deposition were assumed to be 0.1 ML/s but due to the calibration of the system being focused on higher rates of growth there is an uncertainty of 20% and as such it is possible closer to 1 ML of InSb was deposited.

Like the GaInSb quantum well samples explored in this work, the confinement of carriers was also an issue in the first sample. This was again improved by the introduction of AlGaSb barriers, though the increased potential increased the energy of the electron ground state out of the InSb insertions. As with other samples grown on an IMF there was an increased defect density originating at the GaAs/GaSb interface. The use of dislocation filtering superlattices in these samples provided an order of magnitude reduction in dislocation density. This could be improved further with optimisation.

7.4.1 Suggestions for Future Work

The control of growth rates is a key factor in the formation of SML quantum dots, and more accurate calibration is needed to determine the amount of InSb deposited. Once this is known, it would be beneficial to determine the optimal quantity of InSb to deposit; too little and the dot density will be low, too much and quantum dots will be replaced with disordered quantum wells.

Where quantum dots did form, the loss mechanism was the excitation of electrons from confined states within the quantum dot to the surrounding quantum well. Altering the number of quantum dot layers within each stack, the thickness of the GaSb layers or the aluminium content of the barriers could be adjusted to separate these states. Such adjustments could also be used to control the emission wavelength.

Production of edge emitting devices using the SML quantum dots in the active region would also be a logical improvement as the samples grown on IMF buffers achieved lasing from the quantum wells at temperatures approaching 200 K. Assuming lasing occurred via the quantum dot regions it would provide a chance to determine the gain properties of InSb SML quantum dots on GaSb, a topic as yet unexplored.

7.5 Replacement of Incandescent Light Sources in Runway Lighting

LEDs utilising InAs quantum dashes within the active region produced the highest power output most efficiently at 1.2 mW/mAcm^2. This design would require an active region of approximately 1 cm^2 to achieved the desired 100 mW per device needed to replace the 2.2 μm component with the Approach Light System (ALS). The total footprint would be 20 cm^2, too large to fit within the ALS footprint. For this reason a higher brightness device would be needed, edge emitting devices provide this high brightness. By processing a sample of the quantum dash into a superluminescent LED it should be

possible to achieve the desired output with between 20 and 40 devices, allowing them to be collocated with the visible components. The wavelength will also need to be extended by 50 nm to avoid the edge of an atmospheric absorption band. Modelling suggests this is possible through either increased InAs dash size or antimony incorporation to produce InAsSb quantum dashes.

Bibliography

[1] Thales Enhaced Flight Vision System. https://www.thalesgroup.com/en/enhanced-flight-vision-system-efvs. Accessed: 5-8-16.

[2] Energy Independence. Security Act of 2007. *Public Law*, 110(140):19, 2007.

[3] CIA. The World Factbook. *CIA Factbook https://www.cia.gov/cia/publications/factbook*, 2014.

[4] Oxley Developments Visible Next Generation Landing Light. http://www.oxleygroup.com/product/visible-next-generation-landing-light. Accessed: 10-8-16.

[5] Gulfstream G550 EFVS. http://mygdas.com/products/g550/technology.htm. Accessed: 10-8-16.

[6] inductiveload. A comparison of the band gaps of metals, insulators and semiconductors. https://commons.wikimedia.org/wiki/File:Band_gap_comparison.svg. Accessed: 18-9-16.

[7] J.R. Chelikowsky and M.L. Cohen. Nonlocal pseudopotential calculations for the electronic structure of eleven diamond and zinc-blende semiconductors. *Phys. Rev. B*, 14:556–582, Jul 1976.

[8] Ioffe Institute. Silicon Datasheet. http://www.ioffe.ru/SVA/NSM/Semicond/Si. Accessed: 12-7-16.

[9] C. Kittel. *Introduction to Solid State*. John Wiley & Sons, 1966.

[10] Y.P. Varshni. Temperature dependence of the energy gap in semiconductors. *Physica*, 34(1):149–154, 1967.

[11] J.R. Botha and A.W.R. Leitch. Temperature dependence of the photoluminescence properties and band gap energy of $In_xGa_{1-x}As$/GaAs quantum wells. *Journal of Electronic Materials*, 29(12):1362–1371, 2000.

[12] L. Vina, S. Logothetidis, and M. Cardona. Temperature dependence of the dielectric function of germanium. *Physical Review B*, 30(4):1979, 1984.

[13] S.M. Sze and K.K. Ng. *Physics of Semiconductor Devices*. John Wiley & Sons, 2006.

[14] E.F. Schubert, T. Gessmann, and J.K. Kim. *Light Emitting Diodes*. Wiley Online Library, 2005.

[15] R.F. Kazarinov and M.R. Pinto. Carrier transport in laser heterostructures. *IEEE Journal of Quantum Electronics*, 30(1):49–53, 1994.

[16] R.A. Smith. Semiconductors. 1978.

[17] Dr David Leadley. Density of states for bulk, quantum wells, quantum wires and quantum dots. https://www2.warwick.ac.uk/fac/sci/physics/current/postgraduate/regs/mpags/ex5/bandstructure/. Accessed: 12-7-16.

[18] A. Kazemi, M. Zamiri, J.O. Kim, T. Schuler-Sandy, and S. Krishna. Colloidal and epitaxial quantum dot infrared photodetectors: Growth, performance, and comparison. *Wiley Encyclopedia of Electrical and Electronics Engineering*.

[19] G. Rainò, A. Salhi, V. Tasco, R. Intartaglia, R. Cingolani, Y. Rouillard, E. Tournié, and M. De Giorgi. Subpicosecond timescale carrier dynamics in GaInAsSb/AlGaAsSb double quantum wells emitting at 2.3 μm. *Applied Physics Letters*, 92(10):101931, 2008.

[20] W. Shockley and W.T. Read Jr. Statistics of the recombinations of holes and electrons. *Physical Review*, 87(5):835, 1952.

[21] M. Pope and C.E. Swenberg. Electronic processes in organic solids. *Annual Review of Physical Chemistry*, 35(1):613–655, 1984.

[22] C. Smith, R.A. Abram, and M.G. Burt. Auger recombination in a quantum well heterostructure. *Journal of Physics C: Solid State Physics*, 16(5):L171, 1983.

[23] C.L. Lin, Y.K. Su, T.S. Se, and W.L. Li. Variety transformation of compound at GaSb surface under sulfur passivation. *Japanese Journal of Applied Physics*, 37(12B):L1543, 1998.

[24] P.S. Dutta, A.K. Sreedhar, H.L. Bhat, G.C. Dubey, V. Kumar, E. Dieguez, U. Pal, and J. Piqueras. Passivation of surface and bulk defects in p-GaSb by hydrogenated amorphous silicon treatment. *Journal of Applied Physics*, 79(6):3246–3252, 1996.

[25] W. Shockley. The theory of p-n junctions in semiconductors and p-n junction transistors. *Bell System Technical Journal*, 28(3):435–489, 1949.

[26] C.W. Passchier and R.A.J. Trouw. *Microtectonics*, volume 256. Springer.

[27] F.C. Frank and J.H. Van der Merwe. One-dimensional dislocations. II. misfitting monolayers and oriented overgrowth. In *Proceedings of the Royal Society of London A: Mathematical, Physical and Engineering Sciences*, volume 198, pages 216–225. The Royal Society, 1949.

[28] J.W. Matthews and A.E. Blakeslee. Defects in epitaxial multilayers: I. misfit dislocations. *Journal of Crystal Growth*, 27:118–125, 1974.

[29] R. People and J.C. Bean. Calculation of critical layer thickness versus lattice mismatch for Ge_xSi_{1-x}/Si strained-layer heterostructures. *Applied Physics Letters*, 47(3):322–324, 1985.

[30] E.P. O'Reilly. Valence band engineering in strained-layer structures. *Semiconductor Science and Technology*, 4(3):121, 1989.

[31] M.P.C.M. Krijn. Heterojunction band offsets and effective masses in III-V quaternary alloys. *Semiconductor Science and Technology*, 6(1):27, 1991.

[32] S. Jain, M. Willander, and R. Van Overstraeten. *Compound semiconductors strained layers and devices*, volume 7. Springer Science & Business Media, 2013.

[33] J. Kirch, T. Garrod, S. Kim, J.H. Park, J.C. Shin, L.J. Mawst, T.F. Kuech, X. Song, S.E. Babcock, I. Vurgaftman, et al. $InAs_yP_{1-y}$ metamorphic buffer layers on InP substrates for mid-IR diode lasers. *Journal of Crystal Growth*, 312(8):1165–1169, 2010.

[34] R. Wheatley, M. Kesaria, L.J. Mawst, J.D. Kirch, T.F. Kuech, A. Marshall, Q.D. Zhuang, and A. Krier. Extended wavelength mid-infrared photoluminescence from type-I InAsN and InGaAsN dilute nitride quantum wells grown on InP. *Applied Physics Letters*, 106(23):232105, 2015.

[35] S.H. Huang, G. Balakrishnan, A. Khoshakhlagh, A. Jallipalli, L.R. Dawson, and D.L. Huffaker. Strain relief by periodic misfit arrays for low defect density GaSb on GaAs. *Applied Physics Letters*, 88(13):131911, 2006.

[36] Independent Business Scientific Group. `http://www.ibsg-st-petersburg.com/`. Accessed: 12-7-16.

[37] Mid-IR Diode Optopair Group. http://www.mirdog.spb.ru/products.htm. Accessed: 12-7-16.

[38] Roithner LaserTechnik GmbH. http://www.roithner-laser.com/. Accessed: 12-7-16.

[39] S. Jung, S. Suchalkin, G. Kipshidze, D. Westerfeld, and G.L. Belenky. Light-emitting diodes operating at 2 μm with 10 mW optical power. *IEEE Photonics Technology Letters*, 25(23):2278–2280, 2013.

[40] S. Jung, S. Suchalkin, G. Kipshidze, D. Westerfeld, D. Snyder, M. Johnson, and G. Belenky. GaSb-based type I quantum-well light-emitting diode addressable array operated at wavelengths up to 3.66 μm. *IEEE Photonics Technology Letters*, 21(15):1087–1089, 2009.

[41] S. Jung, S. Suchalkin, D. Westerfeld, G. Kipshidze, E. Golden, D. Snyder, and G. Belenky. High dimensional addressable LED arrays based on type I GaInAsSb quantum wells with quinternary AlGaInAsSb barriers. *Semiconductor Science and Technology*, 26(8):085022, 2011.

[42] J.P. Prineas, J.T. Olesberg, J.R. Yager, C. Cao, C. Coretsopoulos, and M.H.M. Reddy. Cascaded active regions in 2.4 μm GaInAsSb light-emitting diodes for improved current efficiency. *Applied Physics Letters*, 89(21):211108, 2006.

[43] M.K. Haigh, G.R. Nash, S.J. Smith, L. Buckle, M.T. Emeny, and T. Ashley. Mid-infrared $Al_xIn_{1-x}Sb$ light-emitting diodes. *Applied Physics Letters*, 90(23):1116, 2007.

[44] S. Suchalkin, S. Jung, G. Kipshidze, L. Shterengas, T. Hosoda, D. Westerfeld, D. Snyder, and G. Belenky. GaSb based light emitting diodes with strained InGaAsSb type I quantum well active regions. *Applied Physics Letters*, 93(8):81107, 2008.

[45] Ioffe Institute. Ioffe semiconductor material database. `http://www.ioffe.ru/SVA/NSM/Semicond`. Accessed: 12-7-16.

[46] National Physics Laboratory. Principles of photometry. `www.npl.co.uk/principles-of-photometry`,.

[47] A. Krier, M. Yin, V. Smirnov, P. Batty, P.J. Carrington, V. Solovev, and V. Sherstnev. The development of room temperature LEDs and lasers for the mid-infrared spectral range. *Physica Status Solidi (a)*, 205(1):129–143, 2008.

[48] T.N. Danilova, B.E. Zhurtanov, A.N. Imenkov, and Y.P. Yakovlev. Light-emitting diodes based on GaSb alloys for the 1.6–4.4 μm mid-infrared spectral range. *Semiconductors*, 39(11):1235–1266, 2005.

[49] N.D. Stoyanov, B.E. Zhurtanov, A.P. Astakhova, A.N. Imenkov, and Y.P. Yakovlev. High-efficiency LEDs of 1.6–2.4 μm spectral range for medical diagnostics and environment monitoring. *Semiconductors*, 37(8):971–984, 2003.

[50] A. Krier. Physics and technology of mid–infrared light emitting diodes. *Philosophical Transactions of the Royal Society of London A: Mathematical, Physical and Engineering Sciences*, 359(1780):599–619, 2001.

[51] A.A. Popov, V.V. Sherstnev, and Y.P. Yakovlev. Power characteristics of 2.2 μm LEDs for spectroscopic applications. *Technical Physics Letters*, 23(9):701–703, 1997.

[52] E.A. Grebenshchikova, A.N. Imenkov, B.E. Zhurtanov, T.N. Danilova, A.V. Chernyaev, N.V. Vlasenko, and Y.P. Yakovlev. Properties of GaSb-based light-emitting diodes with chemically cut substrates. *Semiconductors*, 37(12):1414–1420, 2003.

[53] N.V. Zotova, N.D. Il'inskaya, S.A. Karandashev, B.A. Matveev, M.A. Remennyi, A.A. Shlenskiĭ, et al. The flip-chip InGaAsSb/GaSb LEDs emitting at a wavelength of 1.94 μm. *Semiconductors*, 40(3):351–356, 2006.

[54] A.A. Popov, V.V. Sherstnev, Y.P. Yakovlev, A.N. Baranov, and C. Alibert. Powerful mid-infrared light emitting diodes for pollution monitoring. *Electronics Letters*, 33(1):86–88, 1997.

[55] M. Piskorski, A. Piotrowska, T.T. Piotrowski, K. Golaszewska, E. Papis, J. Katcki, J. Ratajczak, A. Barcz, and A. Wawro. LPE growth and characterisation of GaInAsSb and GaAlAsSb quaternary layers on (100)GaSb substrates. *Thin Solid Films*, 459(1):2–6, 2004.

[56] J.C. DeWinter, M.A. Pollack, A.K. Srivastava, and J.L. Zyskind. Liquid phase epitaxial $Ga_{1-x}In_xAs_ySb_{1-y}$ lattice-matched to (100)GaSb over the 1.71 to 2.33 μm wavelength range. *Journal of Electronic Materials*, 14(6):729–747, 1985.

[57] B.K. Lee, K.S. Goh, Y.L. Chin, and C.W. Tan. Light emitting diode with gradient index layering, April 6 2004. US Patent 6,717,362.

[58] V.A. Mishurnyi, F. De Anda, A.Y. Gorbatchev, and V.I. Vasil'ev. Some perspectives and peculiarities of the LPE growth of multicomponent Sb-based solid solutions from pentanary liquid phases. *Journal of Electronic Materials*, 28(8):959–962, 1999.

[59] V.M. Smirnov, P.J. Batty, R. Jones, A. Krier, V.I. Vasil'Ev, G.S. Gagis, and V.I. Kuchinskii. GaInAsPSb/GaSb heterostructures for mid-infrared light emitting diodes. *Physica Status Solidi (a)*, 204(4):1047–1050, 2007.

[60] V.M. Smirnov, P.J. Batty, A. Krier, R. Jones, V.I. Vasil'ev, G.S. Gagis, and V.I. Kuchinskii. Pentenary GaInAsPSb for mid-infrared light-emitting diodes and

lasers grown by liquid phase epitaxy. In *Integrated Optoelectronic Devices 2007*, page 647918. International Society for Optics and Photonics, 2007.

[61] A. Krier, V.M. Smirnov, P.J. Batty, V.I. Vasil'Ev, G.S. Gagis, and V.I. Kuchinskii. Room temperature midinfrared electroluminescence from GaInAsSbP light emitting diodes. *Applied Physics Letters*, 90(21):211115, 2007.

[62] N.B. Cook and A. Krier. Midinfrared electroluminescence from pentanary-quaternary heterojunction light-emitting diodes. *Applied Physics Letters*, 95(2):021110, 2009.

[63] A. Krier, V.M. Smirnov, P.J. Batty, M. Yin, K.T. Lai, S. Rybchenko, S.K. Haywood, V.I. Vasil'ev, G.S. Gagis, and V.I. Kuchinskii. Midinfrared photoluminescence and compositional modulation in pentanary GaInAsPSb alloys grown by liquid phase epitaxy. *Applied Physics Letters*, 91(8):082102, 2007.

[64] K.J. Cheetham, A. Krier, I.P. Marko, A. Aldukhayel, and S.J. Sweeney. Direct evidence for suppression of Auger recombination in GaInAsSbP/InAs mid-infrared light-emitting diodes. *Applied Physics Letters*, 99(14):141110, 2011.

[65] E.A. Rezek, R. Chin, N. Holonyak, S.W. Kirchoefer, and R.M. Kolbas. Quantum-well Inp-$In_{(1-x)}Ga_xP_{(1-z)}As_z$ heterostructure lasers grown by liquid phase epitaxy (LPE). *Journal of Electronic Materials*, 9(1):1–27, 1980.

[66] A.N. Baranov, Y. Cuminal, G. Boissier, J.C. Nicolas, J.L. Lazzari, C. Alibert, and A. Joullie. Electroluminescence of GaInSb/GaSb strained single quantum well structures grown by molecular beam epitaxy. *Semiconductor Science and Technology*, 11(8):1185, 1996.

[67] T.A. Nilsen, M. Breivik, E. Selvig, and B.O. Fimland. Critical thickness of MBE-grown $Ga_{(1-x)}In_xSb$ ($x < 0.2$) on GaSb. *Journal of Crystal Growth*, 311(7):1688–1691, 2009.

[68] L. Shterengas, G.L. Belenky, J.G. Kim, and R.U. Martinelli. Design of high-power room-temperature continuous-wave GaSb-based type-I quantum-well lasers with $\lambda > 2.5\mu$m. *Semiconductor Science and Technology*, 19(5):655, 2004.

[69] N. Bertru, A. Baranov, Y. Cuminal, G. Almuneau, F. Genty, A. Joullié, O. Brandt, A. Mazuelas, and K.H. Ploog. Long-wavelength (Ga,In)Sb/GaSb strained quantum well lasers grown by molecular beam epitaxy. *Semiconductor Science and Technology*, 13(8):936, 1998.

[70] C. Mourad, D. Gianardi, K.J. Malloy, and R. Kaspi. 2 μm GaInAsSb/AlGaAsSb midinfrared laser grown digitally on GaSb by modulated-molecular beam epitaxy. *Journal of Applied Physics*, 88(10):5543–5546, 2000.

[71] E. Plis, P. Rotella, S. Raghavan, L.R. Dawson, S. Krishna, D. Le, and C.P. Morath. Growth of room-temperature 'arsenic free' infrared photovoltaic detectors on GaSb substrate using metamorphic InAlSb digital alloy buffer layers. *Applied Physics Letters*, 82(11):1658–1660, 2003.

[72] R. Kaspi and G.P. Donati. Digital alloy growth in mixed As/Sb heterostructures. *Journal of Crystal Growth*, 251(1-4):515–520, 2003.

[73] J.G. Cody, D.L. Mathine, R. Droopad, G.N. Maracas, R. Rajesh, and R.W. Carpenter. Application of the digital alloy composition grading technique to strained InGaAs/GaAs/AlGaAs diode-laser active regions. *Journal of Vacuum Science & Technology B*, 12(2):1075–1077, 1994.

[74] C. Grasse, T. Gruendl, S. Sprengel, P. Wiecha, K. Vizbaras, R. Meyer, and M.C. Amann. GaInAs/GaAsSb-based type-II micro-cavity LED with 2-3 μm light emission grown on InP substrate. *Journal of Crystal Growth*, 370:240–243, 2013.

[75] C. Grasse, P. Wiecha, T. Gruendl, S. Sprengel, R. Meyer, and M.C. Amann. InP-based 2.8–3.5 μm resonant-cavity light emitting diodes based on type-II transitions

in GaInAs/GaAsSb heterostructures. *Applied Physics Letters*, 101(22):221107, 2012.

[76] S. Sprengel, A. Andrejew, K. Vizbaras, T. Gruendl, K. Geiger, G. Boehm, C. Grasse, and M.C. Amann. Type-II InP-based lasers emitting at 2.55μm. *Applied Physics Letters*, 100(4):041109, 2012.

[77] S. Sprengel, C. Grasse, P. Wiecha, A. Andrejew, T. Gruendl, G. Boehm, R. Meyer, and M.C. Amann. InP-based Type-II quantum-well lasers and LEDs. *IEEE Journal of Selected Topics in Quantum Electronics*, 19(4):1900909, 2013.

[78] J.P. Prineas, J.T. Olesberg, J.R. Yager, C. Cao, C. Coretsopoulos, and M.H.M. Reddy. Cascaded active regions in 2.4μm GaInAsSb light-emitting diodes for improved current efficiency. *Applied Physics Letters*, 89(21):3, 2006.

[79] V. Tasco, N. Deguffroy, A.N. Baranov, E. Tournié, B. Satpati, A. Trampert, M.S. Dunaevskii, and A. Titkov. High-density, uniform InSb/GaSb quantum dots emitting in the midinfrared region. *Applied Physics Letters*, 89(26):263118, 2006.

[80] J.J. Bomphrey, M.J. Ashwin, and T.S. Jones. The formation of high number density InSb quantum dots, resulting from direct InSb/GaSb (001) heteroepitaxy. *Journal of Crystal Growth*, 420:1–5, 2015.

[81] N. Bertru, O. Brandt, M. Wassermeier, and K. Ploog. Growth mode, strain relief, and segregation of (Ga,In)Sb on GaSb(001) grown by molecular beam epitaxy. *Applied Physics Letters*, 68(1):31–33, 1996.

[82] N. Deguffroy, V. Tasco, A.N. Baranov, E. Tournié, B. Satpati, A. Trampert, M.S. Dunaevskii, A. Titkov, and M. Ramonda. Molecular-beam epitaxy of InSb/GaSb quantum dots. *Journal of Applied Physics*, 101(12):124309, 2007.

[83] Y.A. Parkhomenko, P.A. Dement'ev, and K.D. Moiseev. Quantum dots grown in the InSb/GaSb system by liquid-phase epitaxy. *Semiconductors*, 50(7):976–979, 2016.

[84] K.D. Moiseev, Y.A. Parkhomenko, E.V. Gushchina, A.V. Ankudinov, V.P. Mikhailova, N.A. Bert, and Y.P. Yakovlev. Specific features of the epitaxial growth of narrow-gap InSb quantum dots on an InAs substrate. *Semiconductors*, 43(8):1102–1109, 2009.

[85] K. Moiseev, P. Dement'ev, V. Romanov, and M. Mikhailova. Quantum dots and quantum dashes in the narrow-gap InSb/InAsSbP system. *Journal of Crystal Growth*, 318(1):379–384, 2011.

[86] E. Alphandery, R.J. Nicholas, N.J. Mason, B. Zhang, P. Möck, and G.R. Booker. Self-assembled InSb quantum dots grown on GaSb: A photoluminescence, magnetoluminescence, and atomic force microscopy study. *Applied Physics Letters*, 74(14):2041–2043, 1999.

[87] T.D. Germann, A. Strittmatter, J. Pohl, U.W. Pohl, D. Bimberg, J. Rautiainen, M. Guina, and O.G. Okhotnikov. High-power semiconductor disk laser based on InAs/GaAs submonolayer quantum dots. *Applied Physics Letters*, 92(10):101123, 2008.

[88] Z. Xu, D. Birkedal, M. Juhl, and J. Hvam. Submonolayer InGaAs/GaAs quantum-dot lasers with high modal gain and zero-linewidth enhancement factor. *Applied Physics Letters*, 85(15):3259–3261, 2004.

[89] S.S. Mikhrin, A.E. Zhukov, A.R. Kovsh, N.A. Maleev, V.M. Ustinov, Y.M. Shernyakov, I.P. Soshnikov, D.A. Livshits, I.S. Tarasov, D.A. Bedarev, et al. 0.94 μm diode lasers based on Stranski-Krastanow and sub-monolayer quantum dots. *Semiconductor Science and Technology*, 15(11):1061, 2000.

[90] S. Harrison, M.P. Young, P.D. Hodgson, R.J. Young, M. Hayne, L. Danos, A. Schliwa, A. Strittmatter, A. Lenz, H. Eisele, et al. Heterodimensional charge-carrier confinement in stacked submonolayer InAs in GaAs. *Physical Review B*, 93(8):085302, 2016.

[91] V.M. Ustinov, N.A. Maleev, A.E. Zhukov, A.R. Kovsh, A.Y. Egorov, A.V. Lunev, B.V. Volovik, I.L. Krestnikov, Y.G. Musikhin, N.A. Bert, et al. InAs/InGaAs quantum dot structures on GaAs substrates emitting at 1.3 μm. *Applied Physics Letters*, 74(19):2815–2817, 1999.

[92] A. Stintz, G.T. Liu, A.L. Gray, R. Spillers, S.M. Delgado, and K.J. Malloy. Characterization of InAs quantum dots in strained $In_xGa_{1-x}As$ quantum wells. *Journal of Vacuum Science & Technology B*, 18(3):1496–1501, 2000.

[93] J. Tatebayashi, M. Nishioka, and Y. Arakawa. Over 1.5 μm light emission from InAs quantum dots embedded in InGaAs strain-reducing layer grown by metalorganic chemical vapor deposition. *Applied Physics Letters*, 78(22):3469–3471, 2001.

[94] G. Balakrishnan, S. Huang, T.J. Rotter, A. Stintz, L.R. Dawson, K.J. Malloy, H. Xu, and D.L. Huffaker. 2.0 μm wavelength InAs quantum dashes grown on a GaAs substrate using a metamorphic buffer layer. *Applied Physics Letters*, 84(12):2058–2060, 2004.

[95] R.H. Wang, A. Stintz, P.M. Varangis, T.C. Newell, H. Li, K.J. Malloy, and L.F. Lester. Room-temperature operation of InAs quantum-dash lasers on InP [001]. *IEEE Photonics Technology Letters*, 13(8):767–769, 2001.

[96] S. Fafard, Z. Wasilewski, J. McCaffrey, S. Raymond, and S. Charbonneau. InAs self-assembled quantum dots on InP by molecular beam epitaxy. *Applied Physics Letters*, 68(7):991–993, 1996.

[97] J. Brault, M. Gendry, G. Grenet, G. Hollinger, Y. Desieres, and T. Benyattou. Role of buffer surface morphology and alloying effects on the properties of InAs nanostructures grown on InP (001). *Applied Physics Letters*, 73(20):2932–2934, 1998.

[98] S. Addamane, A. Mansoori, N. Dawson, C. Hains, R. Dawson, and G. Balakrishnan. Emission wavelength control in InAs(Sb) quantum dashes-in-a-well structures. *Journal of Vacuum Science & Technology B*, 34(2):02L103, 2016.

[99] Q. Gong, R. Nötzel, P.J. Van Veldhoven, T.J. Eijkemans, and J.H. Wolter. Shape transition from InAs quantum dash to quantum dot on InP(311)A. *Journal of Crystal Growth*, 280(3):413–418, 2005.

[100] Y. Zhao, S.J.C. Mauger, N. Bertru, H. Folliot, T. Rohel, and P.M. Koenraad. Volmer–Weber InAs quantum dot formation on InP(113)B substrates under the surfactant effect of Sb. *Applied Physics Letters*, 105(3):033113, 2014.

[101] W. Lu, M. Bozkurt, J.G. Keizer, T. Rohel, H. Folliot, N. Bertru, and P.M. Koenraad. Shape and size control of InAs/InP(113)B quantum dots by Sb deposition during the capping procedure. *Nanotechnology*, 22(5):055703, 2010.

[102] I. Alghoraibi, L. Joulaud, C. Paranthoen, A. Le Corre, O. Dehaese, N. Bertru, H. Folliot, P. Caroff, and S. Loualiche. InAs self-assembled quantum dot and quantum dash lasers on InP for 1.55μm optical telecommunications. In *2006 2nd International Conference on Information & Communication Technologies*, volume 2, pages 2085–2090. IEEE, 2006.

[103] Konstantinos Papatryfonos. *Lasers à bâtonnets quantiques InAs/InP émettant dans la gamme 1.6-2.5 μm pour la détection de gaz.* PhD thesis, L'Universite Pierre Et Marie Curie - Paris 6, 2015.

[104] K. Kawaguchi, M. Ekawa, T. Akiyama, H. Kuwatsuka, and M. Sugawara. Surfactant-related growth of $InAs_{1-x}Sb_x$ quantum structures on InP(001) by metalorganic vapor-phase epitaxy. *Journal of Crystal Growth*, 291(1):154–159, 2006.

[105] F. Doré, C. Cornet, P. Caroff, A. Ballestar, J. Even, N. Bertru, O. Dehaese, I. Alghoraibi, H. Folliot, R. Piron, et al. InAs(Sb)/InP(100) quantum dots for mid-infrared emitters: Observation of 2.35μm photoluminescence. *Physica Status Solidi (c)*, 3(11):3920–3923, 2006.

[106] C. Cornet, F. Doré, A. Ballestar, J. Even, N. Bertru, A. Le Corre, and S. Loualiche. InAsSb/InP quantum dots for midwave infrared emitters: A theoretical study. *Growth*, 5:6, 2005.

[107] Postgraduate Research on Photonics as an Enabling Technology. `http://www.prophet-itn.eu/`. Accessed: 5-8-16.

[108] K. Papatryfonos, G. Rodary, C. David, F. Lelarge, A. Ramdane, and J.-C. Girard. One-Dimensional Nature of InAs/InP Quantum Dashes Revealed by Scanning Tunneling Spectroscopy. *Nano Letters*, 15(7):4488–4497, 2015.

[109] K Papatryfonos, S Joshi, K Merghem, S Bouchoule, S Guilet, L Le Gratiet, A Martinez, and A Ramdane. Quantum dash based lasers for gas sensing. In *26th International Conference on Indium Phosphide and Related Materials (IPRM)*, pages 1–2. IEEE, 2014.

[110] C.J.K. Richardson and M.L. Lee. Metamorphic epitaxial materials. *MRS Bulletin*, 41(03):193–198, 2016.

[111] J.W. Matthews. Defects associated with the accommodation of misfit between crystals. *Journal of Vacuum Science & Technology*, 12(1):126–133, 1975.

[112] C.J.K. Richardson, L. He, and S. Kanakaraju. Metamorphic growth of III-V semiconductor bicrystals. *Journal of Vacuum Science & Technology B*, 29(3):03C126, 2011.

[113] J.M. Kang, M. Nouaoura, L. Lassabatere, and A. Rocher. Accommodation of lattice mismatch and threading of dislocations in GaSb films grown at different temperatures on GaAs (001). *Journal of Crystal Growth*, 143(3-4):115–123, 1994.

[114] A.Y. Babkevich, R.A. Cowley, N.J. Mason, S. Weller, and A. Stunault. X-ray scattering from dislocation arrays in GaSb. *Journal of Physics: Condensed Matter*, 14(49):13505, 2002.

[115] J.M. Kang, S.-K. Min, and A. Rocher. Asymmetric tilt interface induced by 60° misfit dislocation arrays in GaSb/GaAs (001). *Applied Physics Letters*, 65(23):2954–2956, 1994.

[116] D.L. Huffaker, M. Mehta, G. Balakrishnan, S. Huang, A. Khoshakhlagh, P. Patel, M.N. Kutty, and L. Dawson. GaSb QW-based buffer-free vertical LED monolithically embedded within a GaAs cavity using interfacial misfit arrays. In *LEOS 2006-19th Annual Meeting of the IEEE Lasers and Electro-Optics Society*, 2006.

[117] S. Huang, G. Balakrishnan, and D.L. Huffaker. Interfacial misfit array formation for GaSb growth on GaAs. *Journal of Applied Physics*, 105(10):103104, 2009.

[118] J. Tatebayashi, A. Jallipalli, M.N. Kutty, S.H. Huang, G. Balakrishnan, L.R. Dawson, and D.L. Huffaker. Room-temperature lasing at 1.82μm of GaInSb/AlGaSb quantum wells grown on GaAs substrates using an interfacial misfit array. *Applied Physics Letters*, 91(14):141102, 2007.

[119] J. Tatebayashi, A. Jallipalli, M.N. Kutty, S.H. Huang, T.J. Rotter, G. Balakrishnan, L.R. Dawson, and D.L. Huffaker. Device characteristics of GaInSb/AlGaSb

quantum well lasers monolithically grown on GaAs substrates by using an interfacial misfit array. *Journal of Electronic Materials*, 37(12):1758–1763, 2008.

[120] Wafer Technology. GaSb wafer datasheet. `http://www.wafertech.co.uk/products/gallium-antimonide-gasb/`. Accessed: 5-8-16.

[121] C.J.K. Richardson, L. He, P. Apiratikul, N.P. Siwak, and R.P. Leavitt. Improved GaSb-based quantum well laser performance through metamorphic growth on GaAs substrates. *Applied Physics Letters*, 106(10):101108, 2015.

[122] P. Bhattacharya, R. Fornari, and H. Kamimura. *Comprehensive Semiconductor Science and Technology, Six-Volume Set*, volume 1. Newnes, 2011.

[123] Y. Asaoka. Desorption process of GaAs surface native oxide controlled by direct Ga-beam irradiation. *Journal of Crystal Growth*, 251(1):40–45, 2003.

[124] M. Ohring. *Materials science of thin films*. Academic press, 2001.

[125] P.F. Fewster. X-ray analysis of thin films and multilayers. *Reports on Progress in Physics*, 59(11):1339, 1996.

[126] A.R. Clawson. Guide to references on III–V semiconductor chemical etching. *Materials Science and Engineering: R: Reports*, 31(1):1–438, 2001.

[127] G.K. Reeves and H.B. Harrison. Obtaining the specific contact resistance from transmission line model measurements. *IEEE Electron Device Letters*, 3(5):111–113, 1982.

[128] A.P. Craig, P.J. Carrington, H. Liu, and A.R.J. Marshall. Characterization of 6.1 Å III–V materials grown on GaAs and Si: A comparison of GaSb/GaAs epitaxy and GaSb/AlSb/Si epitaxy. *Journal of Crystal Growth*, 435:56–61, 2016.

[129] A.P. Craig, M.D. Thompson, Z.B. Tian, S. Krishna, A. Krier, and A.R.J. Marshall. InAsSb-based nBn photodetectors: lattice mismatched growth on GaAs

and low-frequency noise performance. *Semiconductor Science and Technology*, 30(10):105011, 2015.

[130] A.P. Craig, A.R.J. Marshall, Z.B. Tian, and S. Krishna. Mid-infrared InAsSb-based nBn photodetectors with AlGaAsSb barrier layers–Grown on GaAs, using an interfacial misfit array, and on native GaSb. *Infrared Physics & Technology*, 67:210–213, 2014.

[131] K.C. Nunna, S.L. Tan, C.J. Reyner, A.R.J. Marshall, B. Liang, A. Jallipalli, J.P.R. David, and D.L. Huffaker. Short-wave infrared GaInAsSb photodiodes grown on GaAs substrate by interfacial misfit array technique. *IEEE Photonics Technology Letters*, 24(3):218–220, 2012.

[132] I. Vurgaftman, J.R. Meyer, and L.R. Ram-Mohan. Band parameters for III–V compound semiconductors and their alloys. *Journal of Applied Physics*, 89(11):5815–5875, 2001.

[133] H. Okamoto. Semiconductor quantum-well structures for optoelectronics–recent advances and future prospects–. *Japanese Journal of Applied Physics*, 26(3R):315, 1987.

[134] M. Motyka, R. Kudrawiec, J. Misiewicz, M. Hümmer, K. Rößner, T. Lehnhardt, M. Müller, and A. Forchel. Photoreflectance and photoluminescence study of $Ga_{0.76}In_{0.24}Sb$/GaSb single quantum wells: Band structure and thermal quenching of photoluminescence. *Journal of Applied Physics*, 103(11):113514, 2008.

[135] R.H. Miles, D.H. Chow, T.C. Hasenberg, A.R. Kost, and Y.H. Zhang. 3–4 μm laser diodes based on GaInSb/InAs superlattices. In *Narrow Gap Semiconductors 1995: Proceedings of the Seventh International Conference on Narrow Gap Semiconductors, Santa Fe, New Mexico, 8-12 January 1995*, volume 144, page 31. CRC Press, 1995.

[136] J. Meyer, I. Vurgaftman, and R.Q. Yang. Interband quantum well cascade laser, with a blocking quantum well for improved quantum efficiency, August 25 1998. US Patent 5,799,026.

[137] P. Podemski, R. Kudrawiec, J. Misiewicz, A. Somers, R. Schwertberger, J.P. Reithmaier, and A. Forchel. Thermal quenching of photoluminescence from InAs/$In_{0.53}Ga_{0.23}Al_{0.24}As$/InP quantum dashes with different sizes. *Applied Physics Letters*, 89(15):151902, 2006.

[138] M. Mehta, G. Balakrishnan, S. Huang, A. Khoshakhlagh, A. Jallipalli, P. Patel, M.N. Kutty, L.R. Dawson, and D.L. Huffaker. GaSb quantum-well-based"buffer-free"vertical light emitting diode monolithically embedded within a GaAs cavity incorporating interfacial misfit arrays. *Applied Physics Letters*, 89(21):1110, 2006.

[139] K.S. Gadedjisso-Tossou, S. Belahsene, M.A. Mohou, E. Tournié, and Y. Rouillard. Recombination channels in 2.4–3.2 μm GaInAsSb quantum-well lasers. *Semiconductor Science and Technology*, 28(1):015015, 2012.

[140] V. Khanna. Fundamentals of solid-state lighting, 2014.

[141] G. Norris, A. Krier, V.V. Sherstnev, A. Monakhov, and A. Baranov. Mode behavior in InAs midinfrared whispering gallery lasers. *Applied Physics Letters*, 90(1):011105, 2007.

[142] Michael D. Thompson. *GaInSb Quantum Wells grown on Metamorphic Buffer Layers for Mid-Infrared Lasers.* PhD thesis, Lancaster University, 2014.

[143] J. Dobbert, V.P. Kunets, T.A. Morgan, D. Guzun, Y.I. Mazur, W.T. Masselink, and G.J. Salamo. Investigation of deep levels in InGaAs channels comprising thin layers of InAs. *Journal of Materials Science: Materials in Electronics*, 19(8-9):797–800, 2008.

[144] A. Aldukhayel, S.R. Jin, I.P. Marko, S.Y. Zhang, D.G. Revin, J.W. Cockburn, and S.J. Sweeney. Investigations of carrier scattering into L-valley in λ=3.5 μm InGaAs/AlAs(Sb) quantum cascade lasers using high hydrostatic pressure. *Physica Status Solidi (b)*, 250(4):693–697, 2013.

[145] I.P. Marko, S.J. Sweeney, A.R. Adams, S.R. Jin, B.N. Murdin, R. Schwertberger, A. Somers, J.P. Reithmaier, and A. Forchel. Recombination mechanisms in InAs/InP quantum dash lasers studied using high hydrostatic pressure. *Physica Status Solidi (b)*, 241(14):3427–3431, 2004.

[146] R. Schwertberger, D. Gold, J.P. Reithmaier, and A. Forchel. Long-wavelength InP-based quantum-dash lasers. *IEEE Photonics Technology Letters*, 14(6):735–737, 2002.

[147] T. Higashi, T. Yamamoto, S. Ogita, and M. Kobayashi. Experimental analysis of characteristic temperature in quantum-well semiconductor lasers. *IEEE Journal of Selected Topics in Quantum Electronics*, 3(2):513–521, 1997.

[148] Y. Narukawa, Y. Kawakami, M. Funato, S. Fujita, S. Fujita, and S. Nakamura. Role of self-formed InGaN quantum dots for exciton localization in the purple laser diode emitting at 420 nm. *Applied Physics Letters*, 70(8):981–983, 1997.

[149] K. Vizbaras, E. Dvinelis, I. Šimonytė, A. Trinkūnas, M. Greibus, R. Songaila, T. Žukauskas, M. Kaušylas, and A. Vizbaras. High power continuous-wave GaSb-based superluminescent diodes as gain chips for widely tunable laser spectroscopy in the 1.95–2.45 μm wavelength range. *Applied Physics Letters*, 107(1):011103, 2015.

[150] C. Grasse, T. Gruendl, S. Sprengel, P. Wiecha, K. Vizbaras, R. Meyer, and M.C. Amann. GaInAs/GaAsSb-based type-II micro-cavity LED with 2–3μm light emission grown on InP substrate. *Journal of Crystal Growth*, 370:240–243, 2013.

[151] M.B. Wootten, J. Tan, Y.J. Chien, J.T. Olesberg, and J.P. Prineas. Broadband 2.4 μm superluminescent GaInAsSb/AlGaAsSb quantum well diodes for optical sensing of biomolecules. *Semiconductor Science and Technology*, 29(11):115014, 2014.